5-2017

Numerical Investigation of a Phase-Change Material Based Photovoltaic Panel Temperature Regulation System

Rohit Gulati

NUMERICAL INVESTIGATION OF A PHASE-CHANGE MATERIAL BASED PHOTOVOLTAIC PANEL TEMPERATURE REGULATION SYSTEM

by

Rohit Gulati

A Thesis Submitted to the College of Engineering Department of Mechanical Engineering in Partial Fulfillment of the Requirements for the Degree of Master of Science in Mechanical Engineering

Embry-Riddle Aeronautical University
Daytona Beach, Florida
May 2017

NUMERICAL INVESTIGATION OF A PHASE-CHANGE MATERIAL BASED PHOTOVOLTAIC PANEL TEMPERATURE REGULATION SYSTEM

by

Rohit Gulati

This thesis was prepared under the direction of the candidate's Thesis Committee Chair, Dr. Sandra K.S. Boetcher, Associate Professor, Daytona Beach Campus, and Thesis Committee Members Dr. Marc D. Compere, Associate Professor, Daytona Beach Campus, and Dr. Yan Tang, Associate Professor, Daytona Beach Campus, and has been approved by the Thesis Committee. It was submitted to the Department of Mechanical Engineering in partial fulfillment of the requirements for the degree of Master of Science in Mechanical Engineering

Thesis Review Committee:

Sandra K.S. Boetcher, Ph.D.
Committee Chair

Marc D. Compere, Ph.D.
Committee Member

Yan Tang, Ph.D.
Committee Member

Jean-Michel Dhainaut, Ph.D.
Graduate Program Chair,
Mechanical Engineering

Charles F. Reinholtz, Ph.D.
Department Chair,
Mechanical Engineering

Maj Mirmirani, Ph.D.
Dean, College of Engineering

Christopher Grant, Ph.D.
Associate Vice President of Academics

5/2/17
Date

Acknowledgements

This thesis has been made possible by important contributions made by the thesis committee members to my life as a graduate student.

Dr. Boetcher has taken me through two heat transfer courses, advised me for my senior design project, and now guided me through the research for my thesis. I would like to thank her for all the knowledge she has shared, the criticism she gave when I did shabby work, and the answers to my many questions she provided even in late night meetings.

I would like to thank Dr. Compere for sharing his teaching and research methods with me. He has always been interested in the work I did, provided valuable feedback on it, and appreciated whenever I made progress.

Finally, I would like to thank Dr. Tang for introducing me to this project in clean energy, and giving good advice for the direction the project should take.

Abstract

Researcher: Rohit Gulati

Title: Numerical Investigation of a Phase-Change Material Based Photovoltaic Panel Temperature Regulation System

Institution: Embry-Riddle Aeronautical University

Degree: Master of Science in Mechanical Engineering

Year: 2017

As the production of clean electricity has gained importance, photovoltaic (PV) panels have become a widely used technology. But, during operation, PV panels heat up due to the solar insolation and suffer a drop in electrical output. The goal of this investigation is to use phase-change materials (PCM) to passively cool PV panels. The PCM is inside an aluminum container attached to the back surface of the PV panel. Four configurations of the container are investigated. The first configuration is a container with bulk PCM occupying its entire interior volume. The depth of this container is varied. The second configuration adds straight aluminum fins to a container of fixed depth. The length, width and spacing of the fins are parametrically varied. The third configuration uses an aluminum honeycomb core acting as a fin inside the container. Two cell sizes of the honeycomb are modelled. The fourth configuration utilizes PCM encapsulated in pellets, which are suspended in a water bed inside the container. Numerical simulations are conducted using ANSYS Mechanical APDL for finite element heat conduction. The solid-to-liquid phase change is modeled using the enthalpy method. A constant heat flux to simulate the highest value of local irradiance averaged over a day is applied to the PCM container modules. For all cases, temperatures as a function of time at different locations of the container are reported. Results show that a deeper container regulates PV temperature for a longer time. In the finned configuration, as the length of the fins is increased and the spacing is decreased, the PV surface is maintained at lower temperatures for longer; fin width only has minimal effect. The honeycomb configuration matches these criteria and has the lowest PV temperature at PCM saturation time. The encapsulated configuration performs much worse due to the substantially reduced PCM volume. A cost function developed to compare the results from different configurations shows that a honeycomb fin with cell size of 0.5” is most effective at maintaining low PV temperature for an extended duration.

Table of Contents

List of Figures

List of Tables

Chapter I

Introduction and Literature Review

An ample supply of electricity is essential to the modern world. Lighting, air conditioning, refrigeration, medical equipment, water supply, computing, and transportation are a few major areas which have developed along with, and thus, reliant on electric supply. Today, an additional strain on the power grid is being added in the form of personal transportation – electric cars. Traditionally, electricity has been produced by power stations that burn fossil fuels such as coal, oil, and natural gas. According to the United States Energy Information Administration, about 67% of the electricity generated in the US in 2015 was from fossil fuels [1].

Recently, there has been a shift towards using alternate sources of energy for the production of electricity due to four reasons. First, there is a growing concern over climate change, which is accelerated by the greenhouse gas emissions from burning fossil fuels. Second, burning fossil fuels also generates particulate emissions, which have a negative impact on air quality. Third, fossil fuels are a non-renewable resource, which means they are not a viable electricity generation source for long term energy security. And fourth, to meet the growing demand of electricity more generating capacity is being added to the power grid and new resources are being exploited. 2016 saw the US power grid generating capacity increase by 15 GW, which is the largest net change in 5 years [2].

One of the primary alternate technologies for electricity generation is the use of photovoltaic panels to capture solar energy. PV panels make us of the photovoltaic effect exhibited by some semiconducting materials to generate an electric potential from sunlight. This method of generating electricity creates no greenhouse gas or particulate emissions. Also, solar irradiance is a free and renewable energy resource, which makes it an appealing option.

While PV panels are widely used to generate clean electricity, they are only approximately 10-16% efficient in converting incident solar irradiance into electricity. This is because the photovoltaic cells, which are linked together to form a solar panel, produce electricity from a specific range of light frequencies. All remaining frequencies in solar irradiance are unused. This remaining incident energy turns to heat and raises the temperature of the PV panels. As the temperature increases, the electrical output of the panels drops, thereby decreasing the efficiency. Different researchers have shown that a crystalline silicon PV panel operating above 25°C shows a temperature-dependent power decrease with a coefficient between 0.4%/K and 0.65%/K [3-5]. Thus, lowering the operating temperature of a PV panel can lead to a significantly improved electrical output, as shown in Figure 1.1.

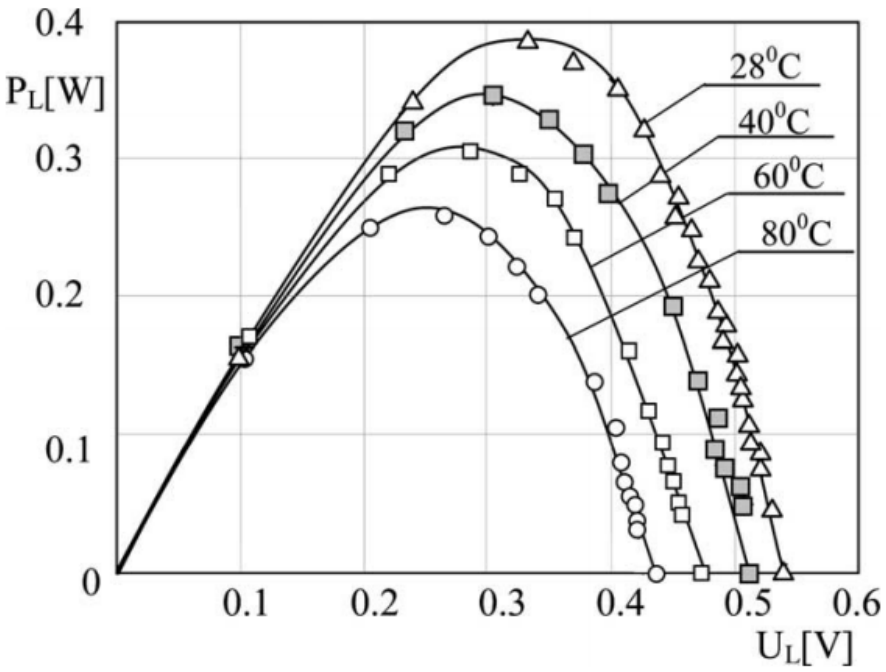

Figure 1.1: Output power versus voltage of a single crystalline silicon solar cell at various temperatures [5].

Several methods of thermal regulation have been developed in order to prevent the drop in electrical output of PV panels caused by an increase in operating temperature. PV panels may be passively or actively cooled. Passive cooling usually relies on natural convection heat transfer due to the circulation of air in the open space behind the PV panel. While this cooling method has some benefits ground mounted and roof mounted PV panels, building integrated photovoltaics (BIPVs) are not inherently able to take advantage of this type of cooling due to the restricted space behind the panels. According to Krauter et al., in the absence of this passive cooling mechanism BIPVs yield a 9.3% lower electrical output when compared to non-integrated PV panels [6]. Active cooling can be used for all kinds of PV panel installations, but consumes energy to pump a fluid (usually water) over the front or back surface of the PV panel.

When the temperature regulation system stores the waste heat, which is then used for thermal work, the system is called a photovoltaic/thermal (PVT) hybrid collector. Liquid- and air-cooled PVT and BIPVT hybrid collectors have been studied extensively [7, 8]. However, using phase-change material (PCM) as the heat sink in PVT or BIPVT systems is an emerging technology that has recently gained attention, as detailed in the review conducted by Ma et al. [9].

Phase change material is engineered to absorb large amounts of latent heat over a very narrow temperature band. Thus, if there is good thermal contact between the PCM and the PV panel, a PCM-based temperature regulation system should be able to maintain the PV panel at near-constant temperature while the PCM absorbs the waste heat from the panel and changes phase. The heat energy stored in the PCM can then either be removed through a heat exchanger, or utilized for other applications.

One of the earliest studies of PCM affixed to a PV panel was conducted by Häusler and Rogaß in 1998 [10]. Häusler and Rogaß used a glass tank filled with water, inside which there was PCM placed in polyethylene spheres. Poor heat transport from the PV panel to the PCM was seen due to the small contact area and poor thermal contact caused by the bad thermal conductivity of the spheres. A second design was also tested, with the PCM now encased in flat copper tanks, again placed in the water filled glass tank. This time, good heat transport was seen, but tanks were destroyed due to the corrosive nature of the PCM and the volume changes caused with a change in phase. The system was improved later with a new design which featured an aluminum absorber [11]. The photovoltaic cells are laminated directly onto one side of the absorber, while the other side has a tank filled with PCM.

In 2004 Huang et al. were able to develop one of the first numerical models of a system that uses PCM to moderate the temperature of a PV panel [12]. This model was then validated with results from experiments conducted using similarly sized geometries. The effect of adding metal fins to the system was also studied. This showed a significant improvement in the thermal performance of the regulation system. In 2006, Huang et al. presented further experimental evaluation of PV-PCM systems that utilized internal fins [13]. For three different systems, the numbers, dimensions, and forms of fins for two PCMs were investigated. All of the PCM assisted finned systems showed improvement over a finned PV panel cooled by natural ventilation. The same researchers also published a study that compared results from a three-dimensional (3D) model of a PV-PCM system to the two-dimensional (2D) model presented in their earlier work. A good agreement was found between the two numerical modelling approaches [14].

One of the first BIPV systems using PCM as a heat sink was built and tested at Oak Ridge National Laboratory by Kosny et al. in 2009 [15, 16]. Amorphous silicon PV laminates and PCM heat sinks were integrated into metal panels to be placed on the roof. During the winter, the roof acted as a passive solar collector where the PCM stored solar heat in the day, which was released in the night to reduce building heating loads. During the summer, the PCM in the roof acted as a heat sink, reducing the heat gained by the interior of the house. The investigators focused on thermal characteristics of the PCM during solar heating rather than the efficiency of the PV panels. They found that the PV-PCM roof generated cooling loads that were approximately 55% lower than a standard shingle roof; and during the winter, the PV-PCM roof generated heating loads that were about 30% less than a standard shingle roof.

In 2010, Hasan et al. [17] performed a comparative study of the effect of various PV-PCM systems on the PV panel temperature. Five PCMs were used in the study, which were enclosed in four different kinds of containers attached to the photovoltaic cell to form the PV-PCM system. The containers varied in materials and thicknesses. The performance of each design was evaluated at three solar insolation intensities. It was found that a maximum temperature reduction of 18°C was achieved for 30 minutes.

In 2011, Huang et al. tried to overcome the limited effectiveness of PCM heat sink due to their low thermal conductivities and crystallization segregation during solidification [18]. They experimentally investigated the effect of natural convection in finned PCM heat sinks.

Biwole et al. [19] developed a finite-element model of an impure PCM coupled with a PV panel, and compared isotherms from numerical experiments to an experimental setup. In this study, published in 2013, the researchers found that with the addition of the PCM, the operating temperature of the PV panel remained under 40°C for 80 minutes. Without the use of PCM, the PV panel reached this temperature after only 5 minutes. In 2014, Lo Brano et al. [20] developed a finite-difference thermal model of PCM, which solved two sets of recursive equations for two spatial domains in the PV-PCM system: a boundary domain and an internal domain. The model was validated experimentally under varied weather conditions.

Also, around the same time, Park et al. [21] evaluated the power performance of a BIPV-PCM panel system. The experimental setup consisted of a PV panel with attached PCM heat sink, which was mounted on a rooftop. Along with being exposed to varied

ambient temperatures, insolation, and wind speeds throughout the experiment, different orientations of the PV panel were also introduced. The researchers found that the electrical power output of the PV increased by 3% when the amount of vertical solar radiation was high and when the outdoor air temperature was moderate. An electro-thermal simulation of the combined system, exposed to the same weather conditions as the experiment, was also set up in TRNSYS. Reasonable agreement between the experimental and predicted values of PV temperature and electric power output was seen.

Aelenei et al. [22, 23] developed a one-dimensional heat transfer model coupled with experimental verification to study a prototype BIPV-PCM system. This system was installed on the main façade of a building. While the PV panel forms the outer layer exposed to sunlight, the PCM is embedded into a gypsum insulating board behind the panel. However, the panel and PCM are not in direct thermal contact since there is an air gap of variable width between the two. Their results show an overall combined electrical and thermal efficiency of around 20%.

Maiti et al. [24] proposed a V-trough PV-PCM system and determined the effectiveness of using a paraffin wax-based PCM with a melt temperature between 56-58°C. Metal turnings were embedded into the low-thermal conductivity PCM to promote heat flow through it. Their experiments determined that indoors, the PV temperature was reduced by approximately 25°C for 3 hours, and outdoors, the temperature was reduced by 16°C. The outdoor temperature reduction could be sustained for the entire operating day.

In 2015, Hasan et al. [25] compared the effect of utilizing PCM on the back of PV panels in two different climates: Dublin and Vehari. Two separate PCMs were used in the study – a salt hydrate and a eutectic mixture of two fatty acids. They concluded that the PCM was more effective in regulating the temperature of PV panels in the hotter climate of Vehari, which also gets stable radiation throughout the year. The gains from using the PCM were smaller when in the overcast and cooler climate of Dublin. Also, at both testing sites, the salt hydrate PCM achieved a greater drop of PV panel temperature.

Recently, Sharma et al. experimentally determined the performance of a building-integrated concentrating photovoltaic system thermally regulated with PCM [26]. The system was validated at four different irradiance levels, ranging from 500W/m^2 to 1200 W/m^2. Their highly controlled indoor experiments found that, for all irradiance levels, incorporating PCM resulted in an increase in electrical efficiency and a decrease in the panel temperature. The maximum improvement was seen with a 1000 W/m^2 irradiance, where the use of PCM increased the electrical efficiency by 7.7% and lowered the module center temperature on average by 3.8°C when compared to a standard system.

Almost all the studies on PCM assisted thermal regulation systems have used bulk PCM solidified in a container. Utilizing a slightly different approach to PCM packaging, Ho et al. [27-31] implemented microencapsulated phase change material (MEPCM) as a means of improving the efficiency of BIPVs. In [27], Ho et al. modeled the MEPCM embedded in a fluid as a buoyancy-driven natural convection problem in a porous media. They determined that the MEPCM layer increased the efficiency by as much as 0.42 %. Follow-on numerical studies by the same authors [28-31] model different MEPCM layer

configurations and show the promise of using MEPCM in a fluid bed for BIPV thermal regulation and energy storage.

The literature reviewed shows that experimental design, testing, numerical model development, and performance evaluation of PV-PCM systems have constituted many recent efforts. This thesis presents the work done to achieve the same goal of limiting the increase of PV panel temperature in order to prevent a drop in electrical output by using a PCM based temperature regulation system. Geometries of the different configurations of an organic based PCM are modelled. The PCM melt characteristics are modelled based on the enthalpy method. The same boundary conditions are then applied to each design and then solved numerically using a finite element solver with the same boundary conditions to investigate the effectiveness of the PCM heat sink. Temperatures of various locations in the solution domain are monitored to gain an understanding of the melt process of the PCM. PCM saturation time and PV panel temperature for the different designs are compared. To evaluate the performance of different regulation system configurations, a cost function is developed. The most effective configuration would be the one closest to ideal, and thus, have minimal cost.

Chapter II

Numerical Setup

Through review of past literature, it is seen that a PCM heat sink can be used as a passive temperature regulation system for PV panels. But, there are various ways to implement this idea. To supplement the experimental studies being performed in the laboratory by other researchers, numerical simulations of four different configurations of the PCM are set up. The PCM is inside a container attached directly to the back surface of the PV panel, as shown in Figure 2.1. By comparing the PV panel temperature over time, the effectiveness of different PCM configurations can be gauged.

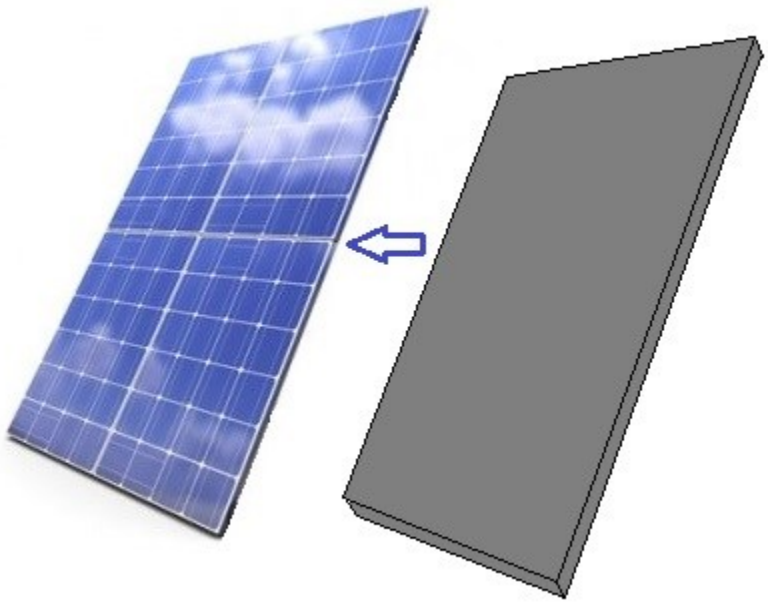

Figure 2.1: Schematic of the PCM container as it attaches to the back of the PV panel.

2.1 Physical Modelling

Before a cooling system is designed for a full-size PV panel, initial studies are focused on regulating the temperature of a small, 15 W PV panel with an area of 929 cm^2. Upon inspection of the 15 W PV panel, it is determined that the cooling area on the back of the panel would have a footprint of 10” by 10” (25.4 cm by 25.4 cm).

The PV panel is not modelled in the simulations because the exact thermal properties of it are not known. Instead, the back surface of the panel is assumed to be in perfect thermal contact with a 1/8” (3.175 mm) thick plate of aluminum. Behind this plate is the PCM container with inner dimensions of 10” by 10”. The container is made of 1/8” thick plates of aluminum as well. This material was chosen for its lightness and good thermal conductivity which would allow heat to travel away from the PV panel with little resistance. Through experiments in the laboratory, and past use in a cold plate for the energy storage system of an EcoCAR2 vehicle [32], it is determined that despite its corrosive nature, the organic based PCM used in this study is compatible with the aluminum container. Figure 2.2 shows the arrangement of the container and the lid attached to the PV panel, as used in simulations.

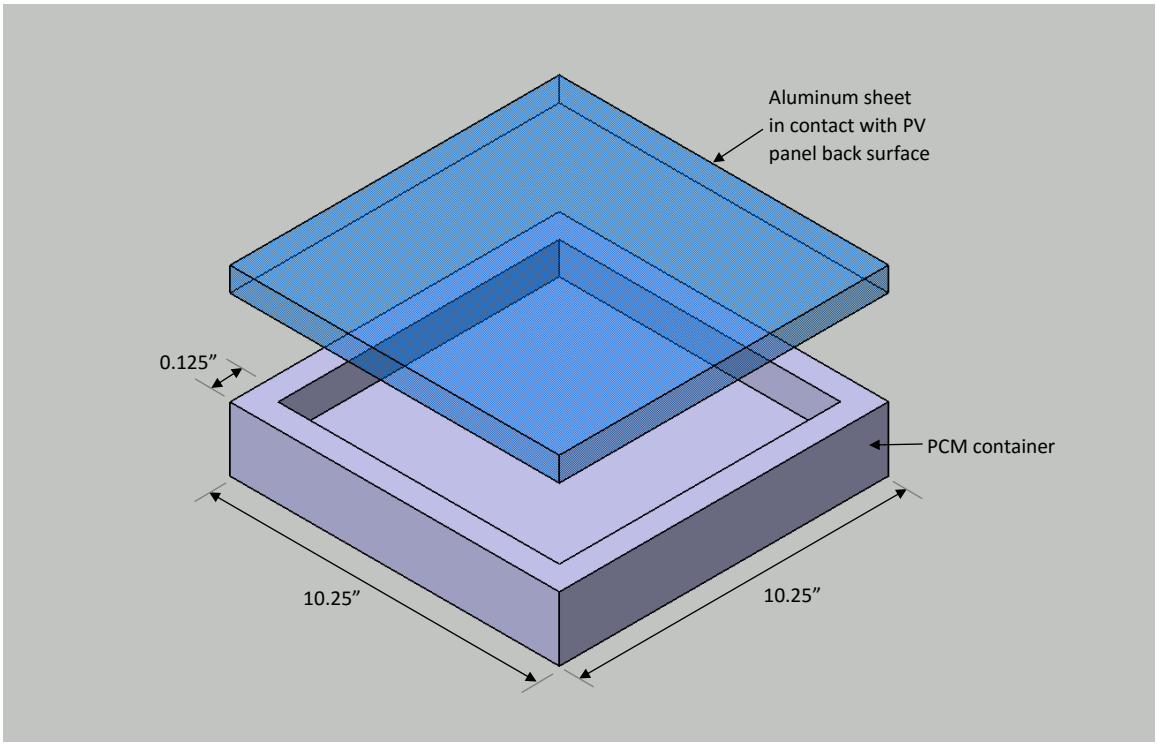

Figure 2.2: Schematic diagram of the PCM container and the lid used in simulations. The PV panel rests on top of the lid, and perfect thermal contact is assumed between them.

With the chosen model of the PV panel and PCM container design, there are four main configurations of the PCM and its container that are numerically solved.

2.1.1 Bulk PCM

The first design consists of just the aluminum container filled with PCM and its lid attached to the back of the PV panel, as shown in Figure 2.3.

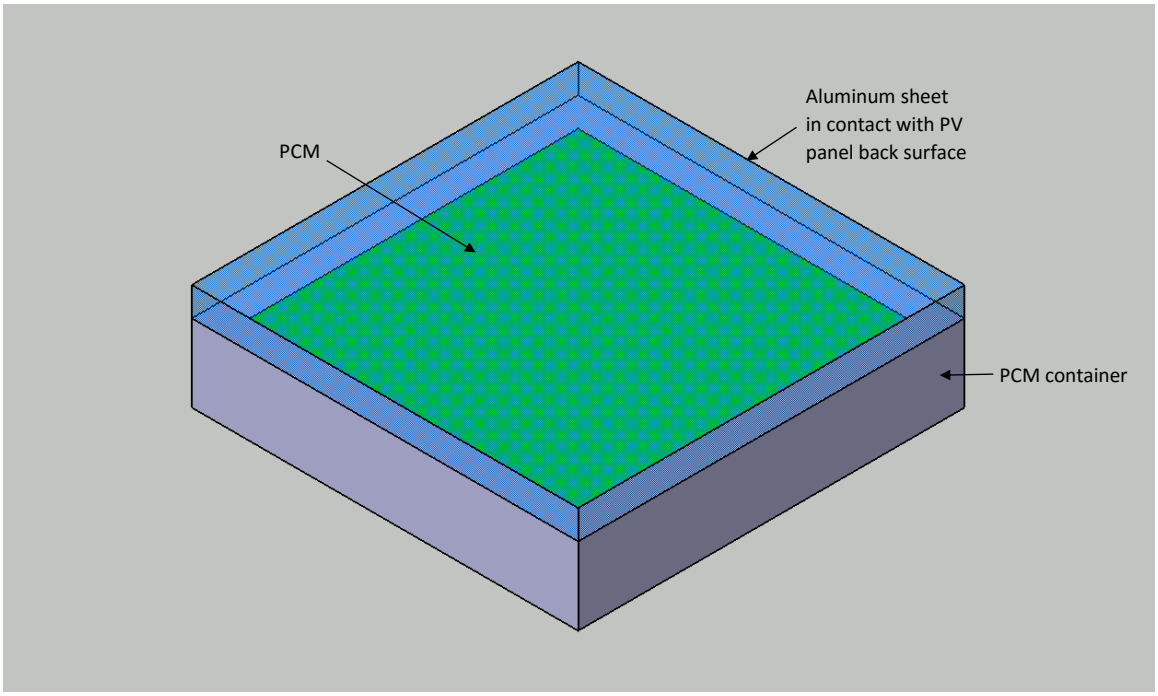

Figure 2.3: Schematic of bulk PCM in the container.

In this configuration, the PCM is also in direct thermal contact with the aluminum sheet that lines the back surface of the PV panel. This configuration was simulated as two- and three-dimensional models.

2.1.1.1 Two-Dimensional Model

The 2D model of the bulk PCM configuration assumes an infinitely large container, and takes advantage of thermal symmetry to reduce the solution domain to a cross section of the actual design. Figure 2.4 shows the geometry used in these 2D simulations.

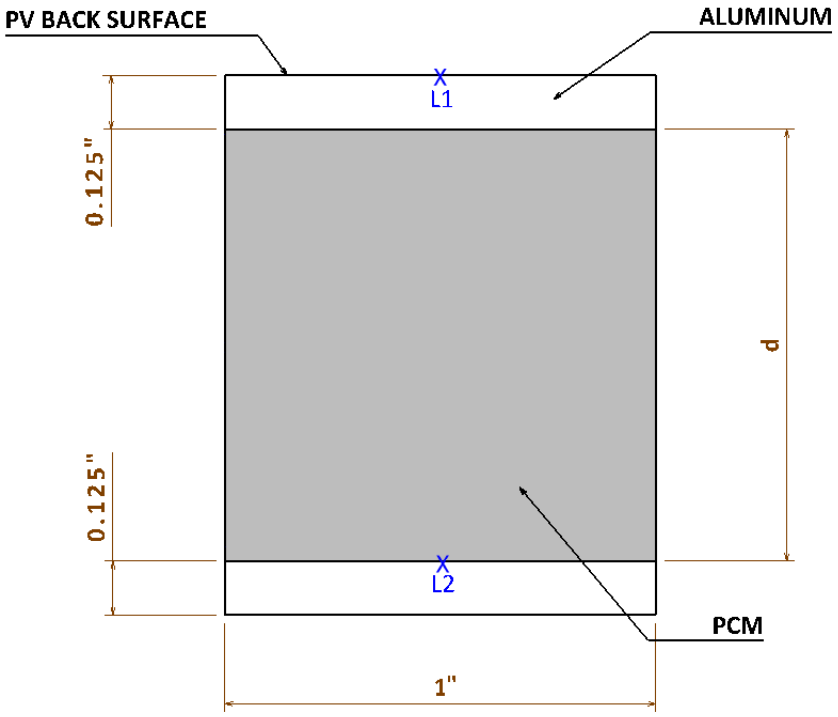

Figure 2.4: Two-dimensional cross section of the bulk PCM configuration as used in the simulations. $L1$ and $L2$ are the temperature monitor locations.

The width of the cross section is held constant at 1” (25.4 mm), while the internal depth of the container, d, is varied. Three depths are modelled – 1/3” (8.467 mm), 1/2” (12.7 mm), and 1” (25.4mm). The container’s internal depth is restricted to a maximum of 1” so that the design can be scaled up and implemented on the back of any full sized PV panel without interfering with the rack mounting system. Temperature was monitored at two locations in this 2D model, as marked in Figure 2.4. $L1$ is the temperature of the back surface of the PV panel, and $L2$ is the temperature of the inside bottom surface of the container.

2.1.1.2 Three-Dimensional Model

Only a PCM depth of 1” is modelled for the 3D simulations of the bulk PCM configuration. This model utilizes physical symmetry of the design to reduce the solution domain. A one-eighth section of the container, lid, and PCM is modelled, shown as a yellow wedge in Figure 2.5. The two sides perpendicular to each other are of length 5.125” (130.175 mm). With the internal depth of the PCM container set to 1”, the total height of the wedge is 1.25” (31.75 mm).

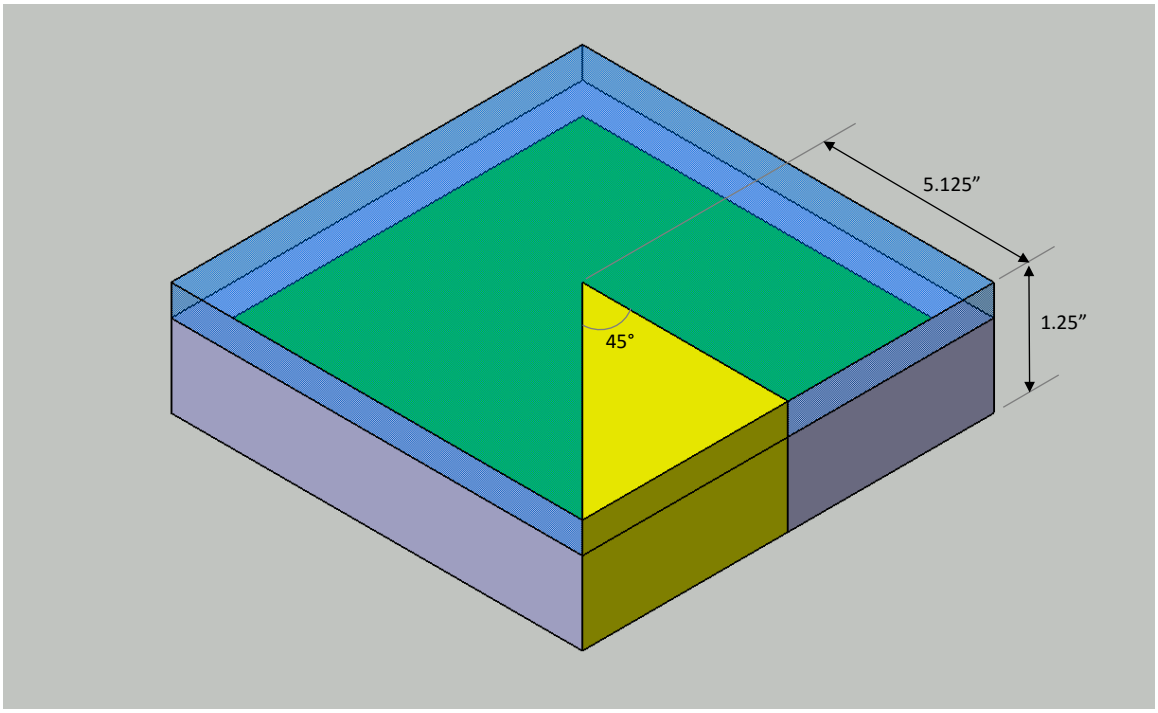

Figure 2.5: Yellow wedge shows a schematic of the geometry used in 3D simulations of the bulk PCM configuration.

Figure 2.6 shows the three sites in this 3D model that are chosen for temperature data collection. At each of these three sites, temperatures are monitored at two locations along the height of the geometry – the back surface of the PV panel and the inside bottom

surface of the container. These locations are analogous to $L1$ and $L2$ from the two-dimensional model, respectively.

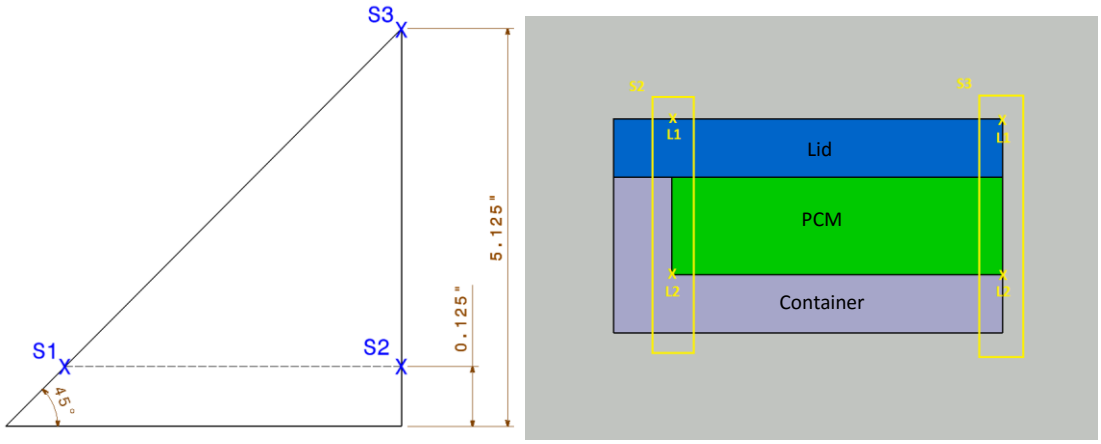

Figure 2.6: (left) A top view of the 3D geometry simulated, showing the three sites of interest. (right) The same wedge as seen from the right, showing sites $S2$ and $S3$, along with the temperature monitor locations at these sites.

2.1.2 Container with Straight Fins

The second configuration investigated utilizes PCM inside the aluminum container with an internal depth of 1". In addition, to enhance heat flow from the PV panel surface into the PCM, straight aluminum fins are placed in the container. Figure 2.6 shows a schematic of this design.

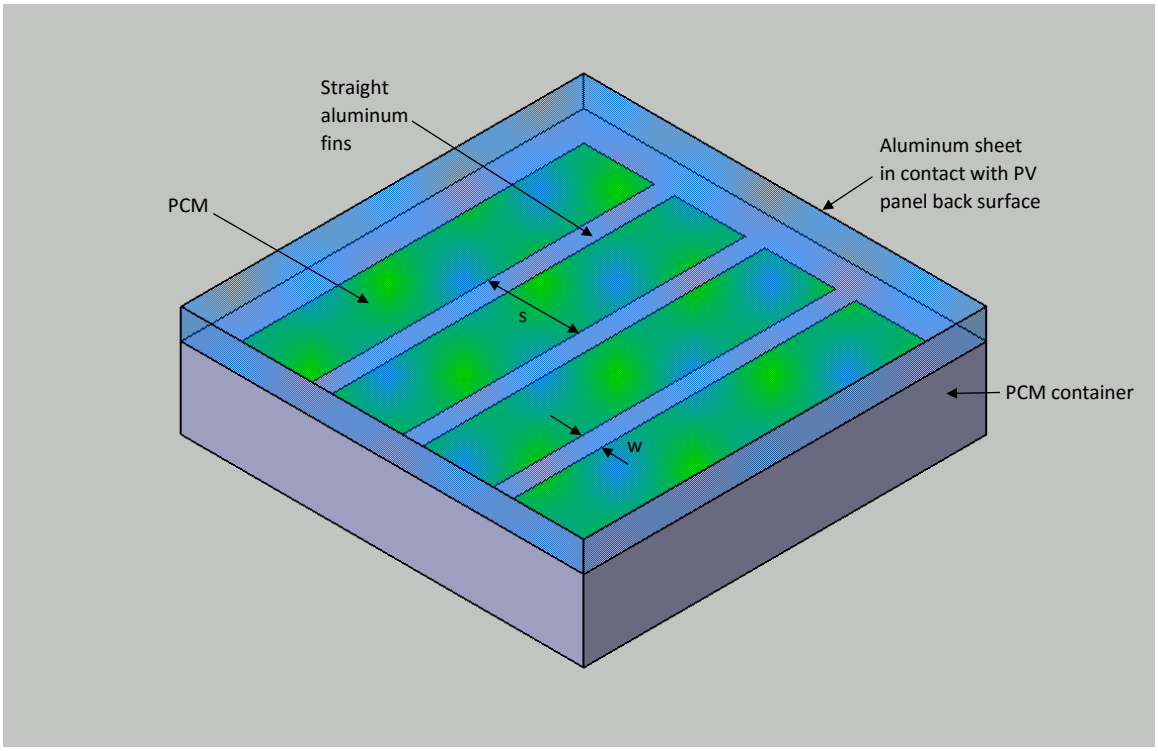

Figure 2.7: Schematic diagram of the PCM container with straight fins. Dimensions s and w represent fin spacing and fin width, respectively.

The aluminum fins in this configuration are attached to the aluminum sheet that lines the back surface of the PV panel, and span the entire length of the container. Different fin lengths, l, fin widths, w, and fin spacings, s, are investigated. The PCM is in contact with the container lid, and also the straight aluminum fins. This configuration was also simulated as two- and three-dimensional models.

2.1.2.1 Two-Dimensional Model

The 2D model of the finned PCM container configuration assumes an infinitely large container, and takes advantage of thermal and geometric symmetry to reduce the solution domain to a cross section of the actual design. Figure 2.8 shows the geometry used in these 2D simulations.

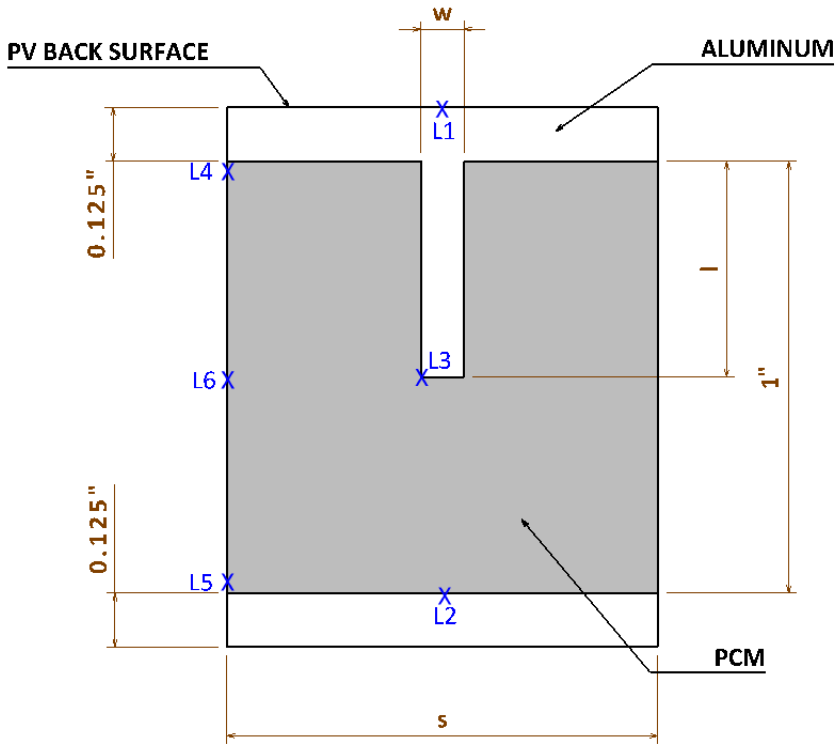

Figure 2.8: Two-dimensional cross section of the finned container configuration as used in the simulations. $L1$ through $L6$ are the temperature monitor locations. Dimensions l, s, and w represent fin length, fin spacing and fin width, respectively.

The internal depth of the container, d, is held constant at 1" (25.4 mm), while three other parameters – l, fin length, w, fin width, and s, fin spacing – are parametrically varied to study the effect on PV panel temperature. Table 2.1 lists the variations in these dimensions in the three cases simulated.

Table 2.1: Different cases of the finned container are modelled by varying fin dimensions in the 2D geometry. Values of for each case are shown below.

Dimension	**Case I**	**Case II**	**Case III**
Fin length, l [mm]	0 – 25.4	13	25.4
Fin width, w [mm]	1	1, 1.5, 2, 3.175	1, 1.5, 2, 3.175
Fin spacing, s [in]	1	0.5, 1, 1.5, 2	0.5, 1, 1.5, 2

In Case I, the fin spacing is held constant at 1", and the length of a 1 mm wide aluminum fin attached to the top plate is varied until it reaches the bottom plate. In Case II, the fin length is held constant at 13mm, while combinations of different fin widths and fin spacing are simulated. Case III is similar to Case II with varied fin width and spacing, but the length of the fin is 25.4 mm so that it connects the top and bottom aluminum plates of the PCM container. Figure 2.8 also shows the locations where temperature was monitored in the 2D model of the finned container. Table 2.2 describes them in more detail.

Table 2.2: Temperature monitor locations in the 2D model of finned container configuration.

Location	Description
L1	Back surface of the PV panel/outer surface of the container lid
L2	Inside bottom surface of the container
L3	Fin tip
L4	PCM (top) – adjacent to the top plate, and halfway between two fins
L5	PCM (bottom) – adjacent to the bottom plate, and halfway between two fins
L6	PCM (middle) – halfway (0.5”) along the depth of the container, and halfway between two adjacent fins

2.1.2.2 Three-Dimensional Model

This model utilizes physical symmetry of the design to reduce the solution domain. A one-fourth section of the finned container, lid, and PCM is modelled, shown as a yellow block in Figure 2.9. The length and width of this square section are both 5.125” (130.175 mm) long. With the internal depth of the PCM container set to 1”, the total height of the block is 1.25” (31.75 mm).

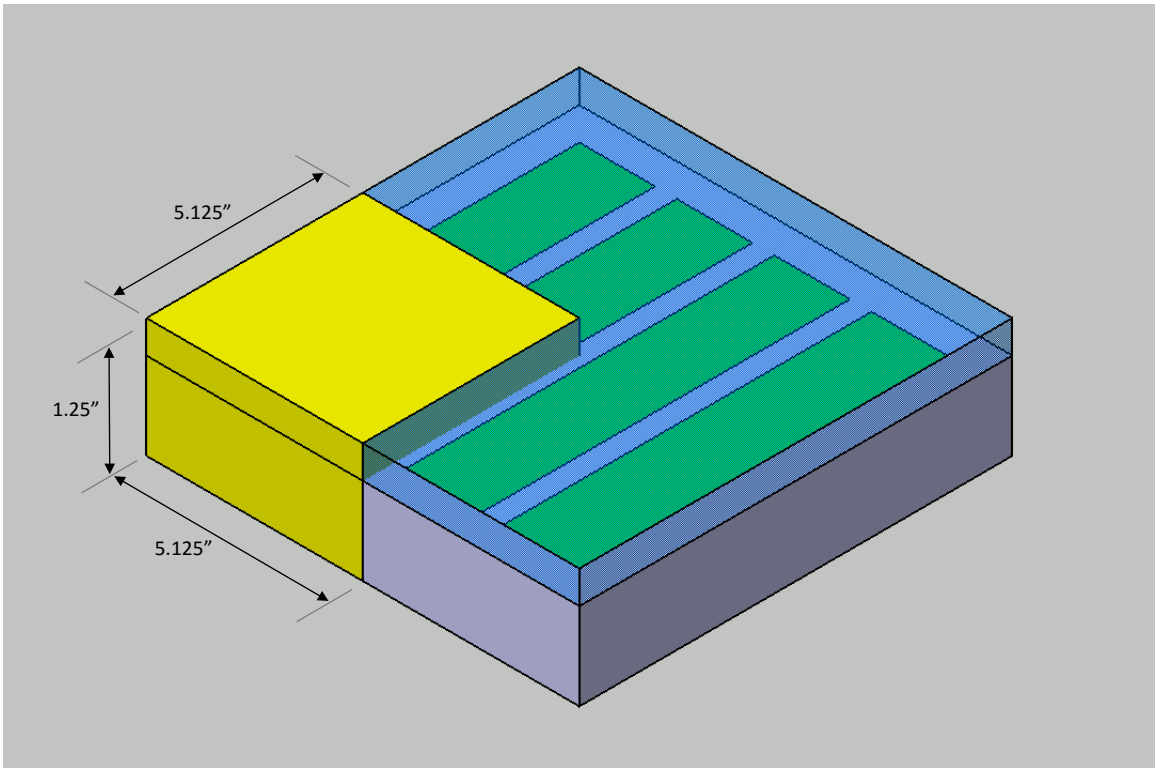

Figure 2.9: Yellow block shows a schematic of the geometry used in 3D simulations of the finned PCM container configuration.

Only two particular cases are modelled as 3D geometries. This is mainly done to compare with results from the 2D simulations and check if the walls of the container, which were not modelled in the 2D geometry, have a significant impact on heat flow. Both cases have fins of length 1”, so that they connect the top and bottom plated of the PCM container. In Case I, the fins have a width, w, of 1mm, and are arranged with a spacing, s, of 0.5”. Thus, the entire container is able to fit 19 fins in it, while the quarter model used for simulations has 10 of these fins. In Case II, the fins have a width, w, of 3.175 mm (1/8”), and are evenly spaced 1” apart. Thus, the entire container is able to fit 9 fins in it, while the quarter model has 5 of these fins.

Six sites of interest are chosen in the quarter model. Since cases I & II have fins which connect the top and bottom plates and span the length of the box, the PCM is effectively divided into separate blocks. Sites $S1$, $S2$, and $S3$ are located such that the PCM block adjacent to the container wall, and the fin adjacent to it, fall within them. Sites $S4$, $S5$, and $S6$ include the central fin of the PCM container, and the PCM block adjacent to it. Figure 2.10 shows a top view of the geometry used in Case II, with the temperature collection sites highlighted. Three slicing planes passing through the sites are also shown.

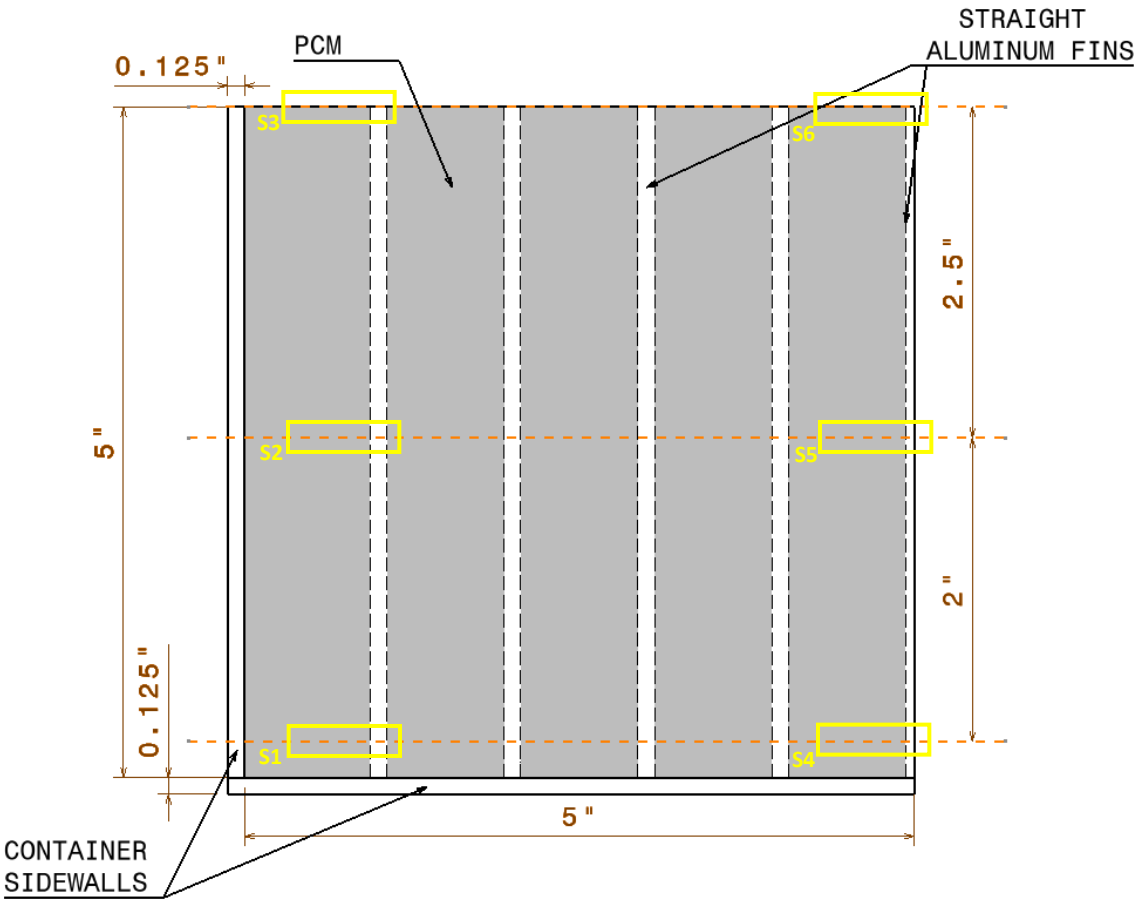

Figure 2.10: Top view of the quarter model of finned container, Case II. All dimensions are drawn to scale. Three slicing planes (dashed orange lines) pass through the PCM blocks to give six sites of interest. Sites $S1$ through $S6$ are highlighted in yellow.

At each of the sites $S1$ through $S6$, a plane parallel to the bottom edge of the container is used to slice the 3D geometry and reveal cross sections similar to the 2D model of Figure 2.8. Temperatures are monitored at locations $L1$ through $L6$, analogous to the 2D model locations. Figure 2.11 shows a back view of the quarter model of Case II, with sites $S3$ and $S6$ visible. Temperature collection locations for site $S6$ are marked $L1$ through $L6$.

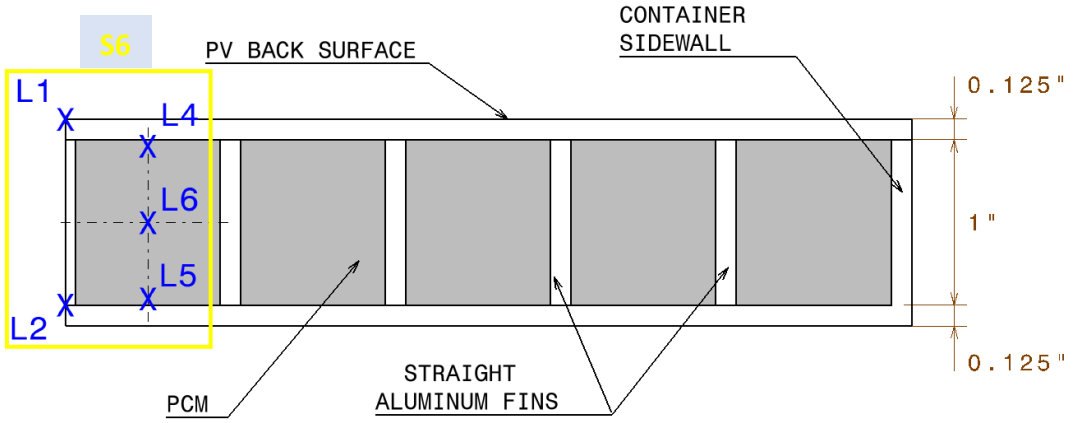

Figure 2.11: Back view of the geometry of the finned container Case II. All dimensions are drawn to scale. Site $S6$ from Figure 2.10 is visible, with the temperature monitor locations $L1$ through $L6$ marked.

2.1.3 Container with Honeycomb Core Fin

For the third configuration investigated a PCM container with an internal depth of 1” is used. A honeycomb core made of aluminum is inserted into the container and acts as a fin to improve heat transfer from the PV surface to the PCM. The honeycomb also has a depth of 1”, connecting the top and bottom plates of the PCM container, dividing the PCM in to separate cells. Figure 2.12 shows a schematic of this design.

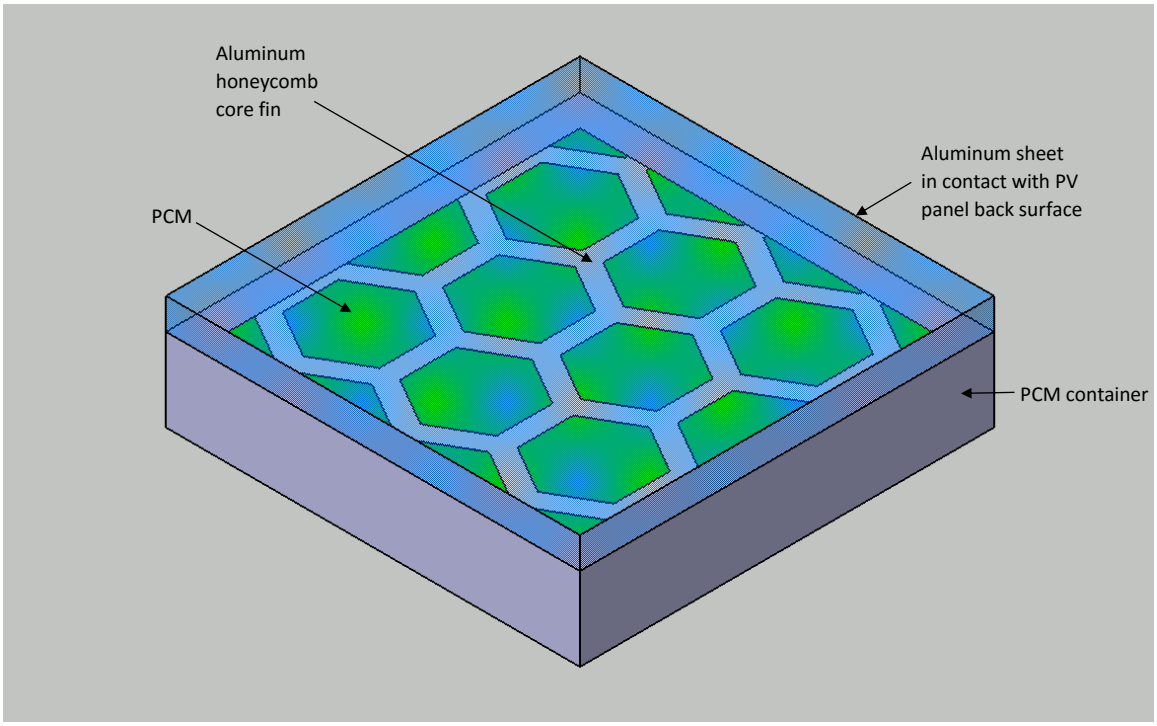

Figure 2.12: Schematic diagram of the PCM container with a honeycomb core fin. The depth of the honeycomb core is 1".

Two cases are investigated with different sizes of the honeycomb core. Case I is modelled on the commercially available honeycomb core from McMaster-Carr (Part# 9365K511). A manufacturer provided cell size of 1" (25.4 mm) and a measured foil thickness of 0.2 mm are used to create the geometry of the fin. Figure 2.13 shows a close-up of the honeycomb. 10 honeycomb cells fit horizontally inside the PCM container. Figure 2.14 shows how symmetry is used to reduce the solution domain to one fourth of the container, similar to the finned design. The quarter model contains 5 honeycomb cells horizontally.

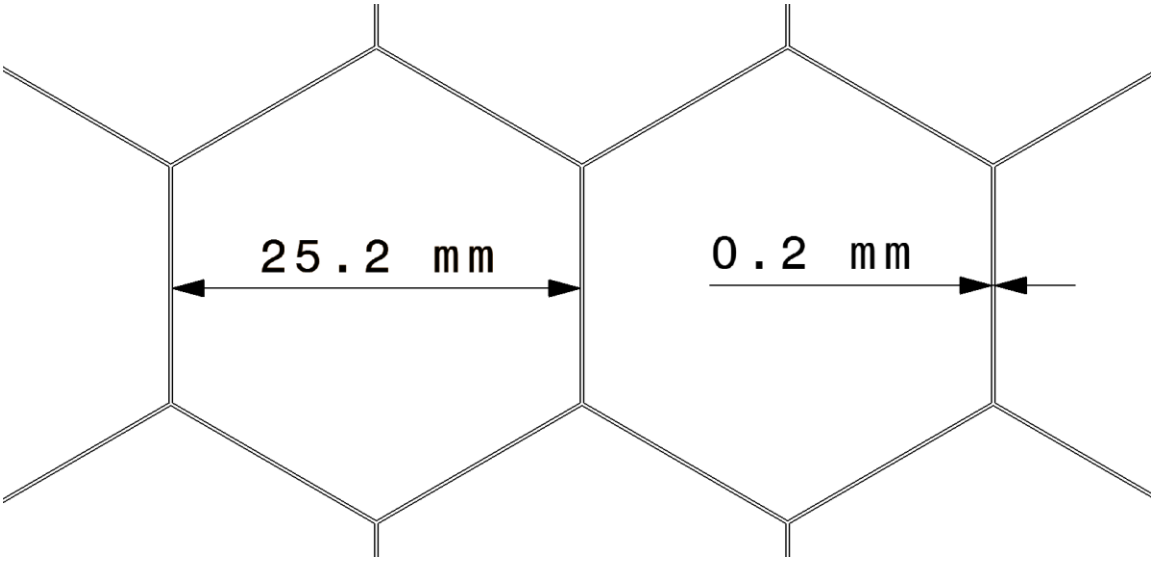

Figure 2.13: Dimensions of the honeycomb core used in Case I. The depth of the honeycomb is 1” (25.4 mm).

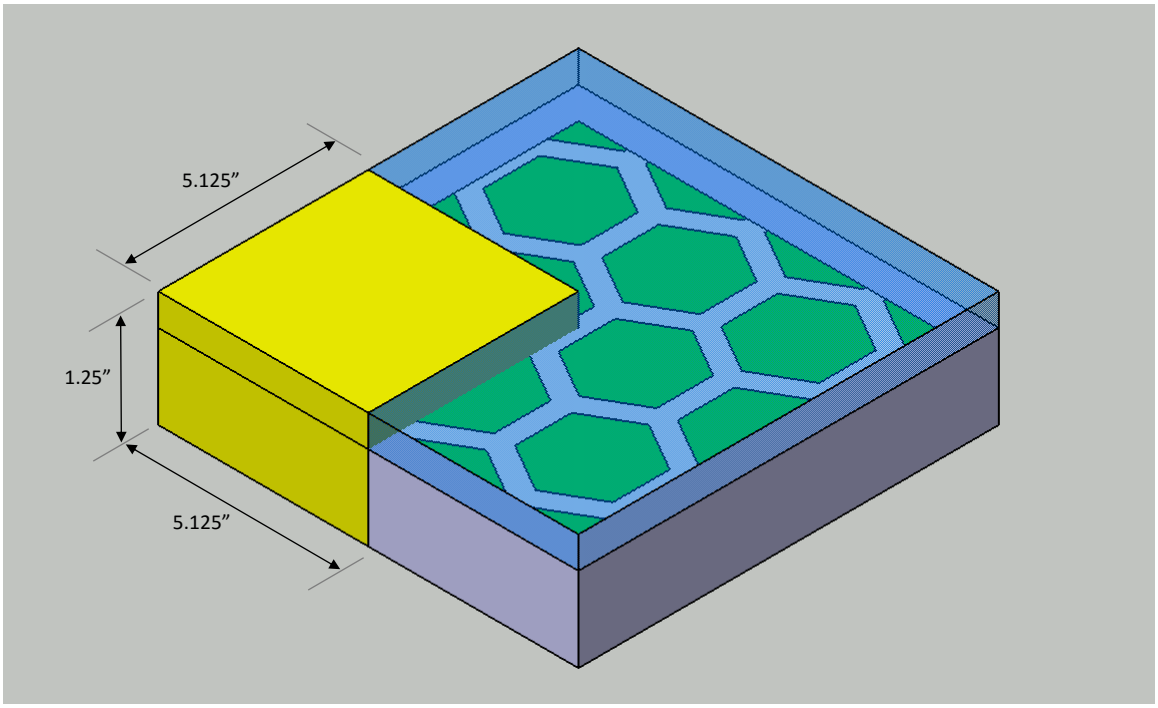

Figure 2.14: Yellow block shows a schematic of the geometry used in 3D simulations of the configuration with a honeycomb core fin inside the PCM container.

Case II of the honeycomb fin design is a modification of Case I. The cell size of the honeycomb is reduced to 0.5” (12.7 mm) to check if distributing the PCM into smaller cells has an effect on the temperature regulation of the PV panel. A close-up of the honeycomb used in Case II is shown in Figure 2.15. With a cell size of 0.5”, 20 honeycomb cells fit horizontally inside the PCM container. Again, symmetry is used to reduce the solution domain to a quarter model containing 10 honeycomb cells horizontally.

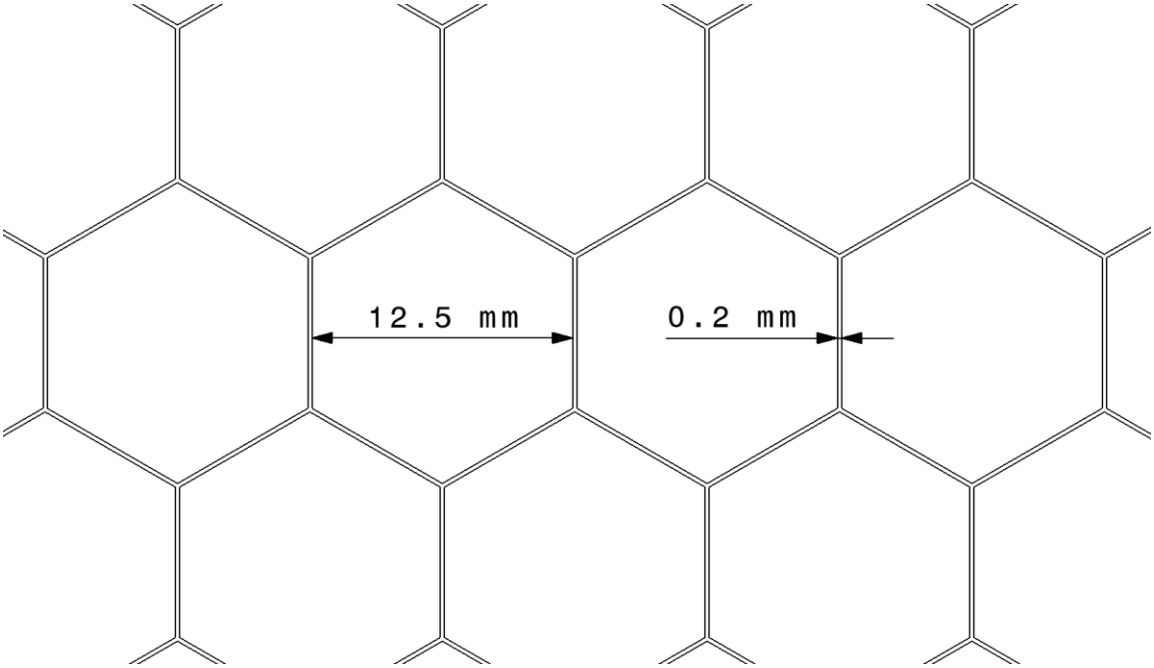

Figure 2.15: Dimensions of the honeycomb core used in Case II. The depth of the honeycomb is 1” (25.4 mm).

Temperatures of four PCM cells in the quarter model are monitored. These cells are labeled BL (bottom left), BR (bottom right), TL (top left), and TR (top right) based on their locations in the quarter model. Figure 2.16 shows the geometry used for Case I with the cells of interest marked.

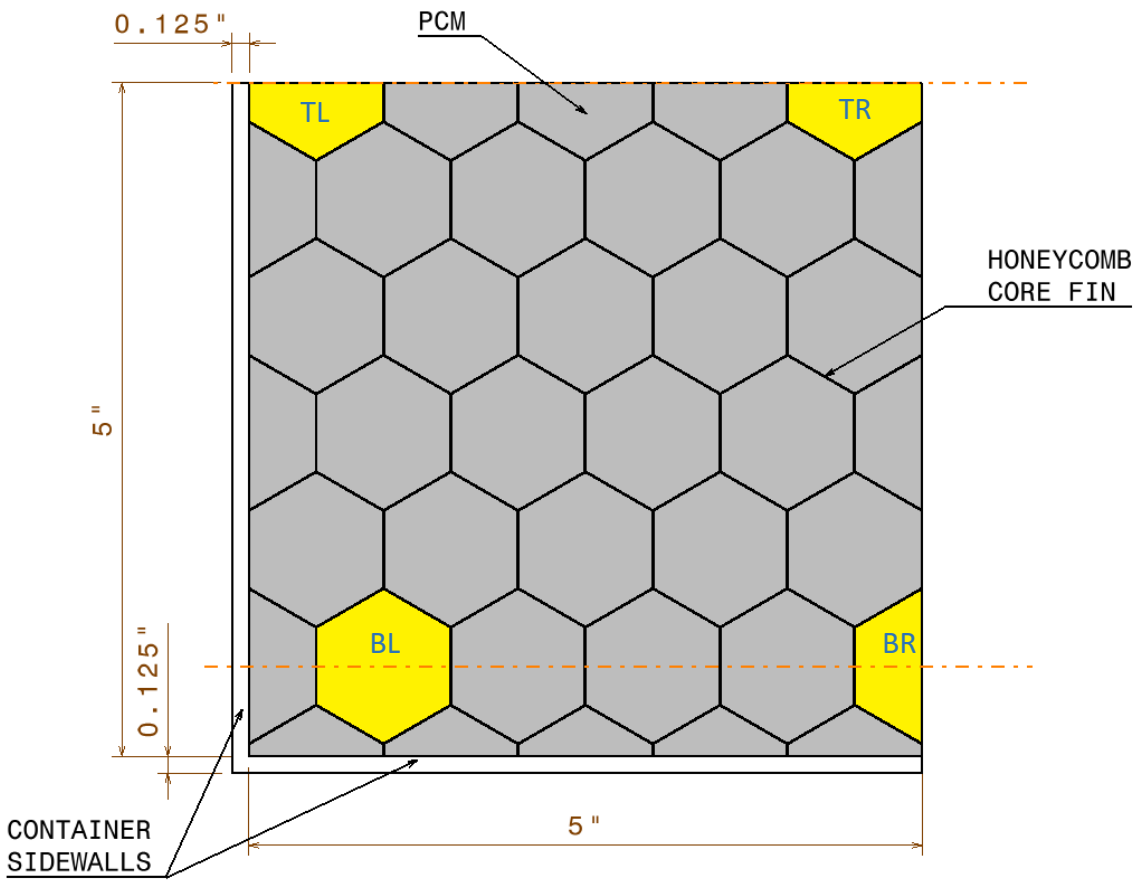

Figure 2.16: Top view of the quarter model of container with honeycomb fin, Case I. All dimensions are drawn to scale. Two slicing planes (dashed orange lines) pass through the centroids of PCM cells highlighted in yellow to give four cells of interest. Cell BL was chosen slightly away from bottom left position so that its centroid doesn't fall on the sidewall.

Slicing planes parallel to the bottom edge of the PCM container are passed through the centroids of the four cells to reveal cross sections. These cross sections are treated like the one shown in Figure 2.8. For each cell, temperatures of six locations $L1$ through $L6$ are monitored.

2.1.4 Encapsulated PCM

While all configurations modelled until now have had the PCM poured directly into the aluminum container, this design uses PCM in encapsulated form. The PCM is encapsulated inside pellets made of a blend of plastics that are resistant to its corrosive properties. Each pellet has a diameter of 18 mm (0.71”) with a 3 mm (0.12”) halo, as shown in Figure 2.17. The halo is due to the sealing in the manufacturing process. The thickness of the wall is measured as 0.45 mm (0.012”).

Figure 2.17: Encapsulated PCM pellets [33].

169 pellets are uniformly arranged in a container with 1” internal depth to form a single layer. The container is filled with water to occupy the remaining volume and provide a medium for heat to travel from the container walls into the pellets. To make the modelling process easier, the dimples and the halo found on the pellets are not modelled. The pellets are thus modelled as thin walled spheres with PCM occupying their entire

interior volume. The encapsulating material is assigned properties of high-density polyethylene (HDPE). Figure 2.18 shows a schematic of this design.

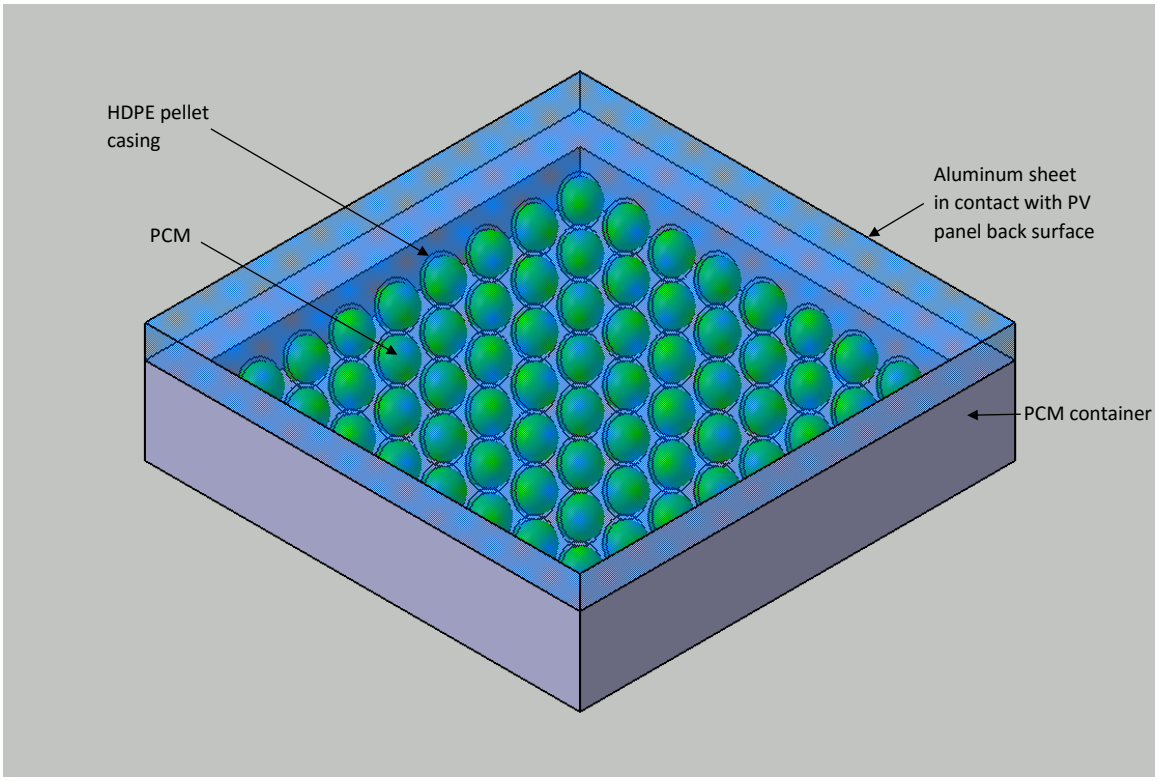

Figure 2.18: Schematic diagram of the PCM container with encapsulated PCM pellets.

Symmetry is used to reduce the solution domain and model only one quarter of the encapsulated PCM configuration, as shown in figure 2.19. There are 49 pellets in the reduced geometry. Only one site at the top right corner of the quarter model (or, the center of the entire PCM container) is chosen for collection of temperature data. At this site, temperatures of the PV panel and the inner surface of the bottom plate are monitored. PCM temperature at the center of the pellet that is at this site is also recorded.

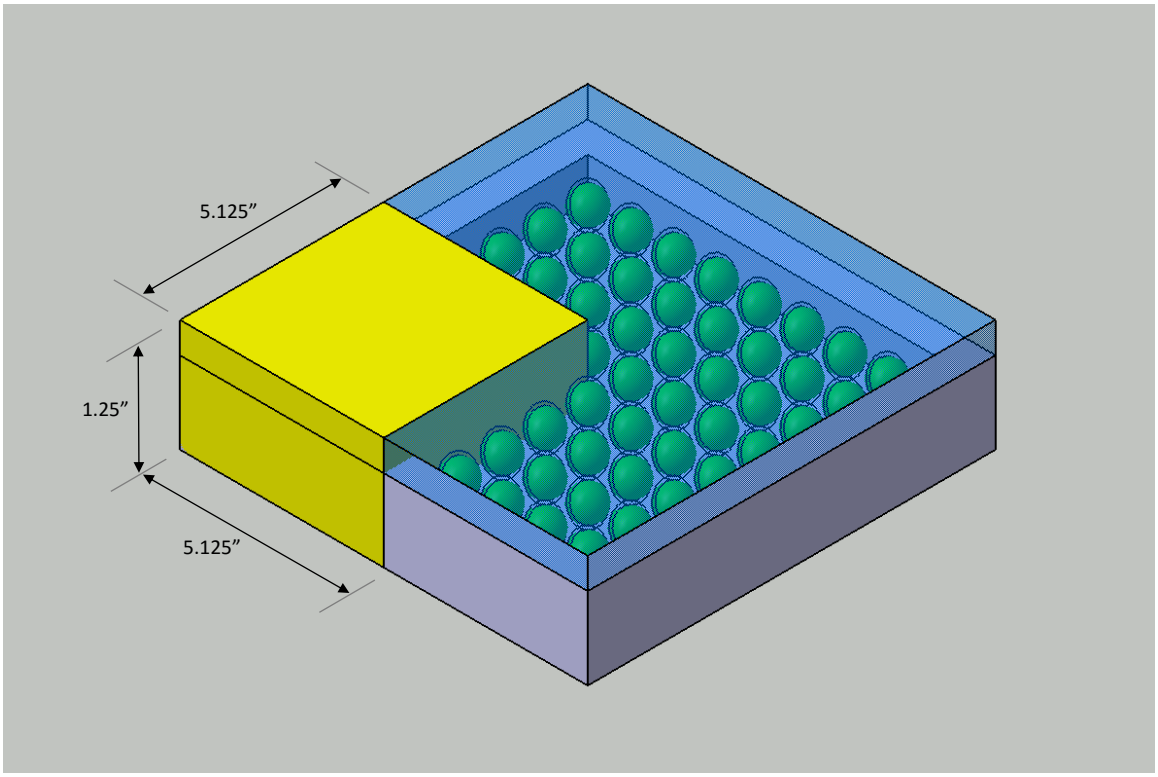

Figure 2.19: Yellow block shows a schematic of the geometry used in 3D simulations of the encapsulated PCM configuration.

2.2 Governing Equations and Boundary Conditions

The PCM used in numerical experiments is a proprietary blend of organic based fatty acids, called PureTemp 29. It is sold commercially by Entropy Solutions, LLC. The melting temperature range of this PCM is 27.6°C to 29.6°C. This saturation temperature was chosen to be higher than the average outdoor temperature of Daytona Beach, and lower than the peak operating temperature of PV panels. Because of this, the PCM's latent heat would not be used up in just reaching thermal equilibrium with the ambient air. Instead, the latent heat would be drawn from the hot PV panel, effectively regulating the panel's temperature. Material properties of PureTemp 29 obtained from the manufacturer are shown in Table 2.3.

Table 2.3: Material properties of PureTemp 29.

Property	**Value**	
	solid phase	liquid phase
Density, ρ $[kg/m^3]$	940	850
Specific Heat Capacity, c_p $[J/kg \cdot K]$	1770	1940
Thermal Conductivity, k $[W/m \cdot K]$	0.25	0.15
Melting Temperature Range $[°C]$	27.6 – 29.6	
Latent Heat of Fusion, h $[J/kg]$	202,000	

For all four configurations of the PCM, the solid-to-liquid phase change is modeled using the enthalpy method developed by Shamsundar and Sparrow [34]. This is a lumped method that does not take into account the interface between the solid phase and the liquid phase, nor the natural convection present in the melt. However, this model has proven to be reasonably accurate at predicting temperature during the phase change. Also, in the encapsulated PCM container, natural convection of the water caused by temperature gradients while the container and its contents heat up is neglected. This is done because the small gaps between the pellets, and between the pellets and the container walls would not let steady convection currents form. In addition, there would not be a very large temperature gradient along the depth of the PCM container.

Using the enthalpy method, the conservation of energy equation in the completely solid solution domain is solved numerically.

$$\frac{\partial h}{\partial t} = k\left[\frac{\partial^2 T}{\partial x^2} + \frac{\partial^2 T}{\partial y^2} + \frac{\partial^2 T}{\partial z^2}\right] \tag{2.1}$$

In Eq. 2.1, h is enthalpy, t is the time, k is thermal conductivity, T is the temperature, and x, y, and z are Cartesian coordinates.

An arbitrary datum for the enthalpy of the PCM is specified at 0°C, and the enthalpies per unit volume for other temperatures are calculated and entered as inputs to the numerical solver. These enthalpy values are listed in Table 2.4.

Table 2.4: Enthalpy values of PureTemp 29 used in simulations.

Temperature $[°C]$	**Enthalpy,** $\boldsymbol{h}$ $[J/m^3]$
0	0
27.6	45,920,880
29.6	230,031,330
50	263,670,930

Material properties of the other materials used in the different configurations are listed in Table 2.5. While the properties of HDPE were aggregated from Matbase, the properties of aluminum and water were obtained from [35].

Table 2.5: Material properties used in simulations.

Property	**Aluminum**	**HDPE**	**Water**
Density, ρ $[kg/m^3]$	2700	974	997
Specific Heat Capacity, c_p $[J/kg \cdot K]$	903	2250	4180
Thermal Conductivity, k $[W/m \cdot K]$	237	0.49	0.618

In order to model the worst case scenario for the temperature regulation system, all external boundaries except the surface in contact with the PV panel are modelled as adiabatic. This way, all the incoming heat will be stored in the container and the PCM within.

A constant heat flux of 525 W/m^2 is applied to the upper surface of the top aluminum plate. The 30-year average of monthly solar radiation database maintained by the National Renewable Energy Laboratory was consulted to obtain this value [36]. The highest average daily irradiation value for flat plate collectors facing south at a fixed tilt equal to the latitude for Daytona Beach was chosen, and then converted to an average heat flux by assuming 12 hours of irradiation per day. It is assumed that all of this insolation is converted to heat and reaches the PCM container.

A uniform initial temperature of 25°C was assumed for the PV panel as well as all components of the temperature regulation system.

2.3 Numerical Solution

The numerical simulations for the transient two- and three- dimensional solution domains were conducted using ANSYS Mechanical APDL R17.0, which is a commercially available finite-element solver. A mesh independence study was conducted for the finned PCM container configuration. The 2D geometry of Case I of this configuration, with a fin length of 1mm, was meshed using two different element size schemes. A mesh with 4037 nodes was compared to a mesh with 9240 nodes. The temperatures at locations $L1$, $L2$, and $L3$ at chosen times differed by less than 0.005%. Automatic time-stepping was used in the simulations, with the solution time-step values

bounded between 0.1 seconds and 10 seconds. The total simulation time was set to 5 hours.

2.4 Cost Function

PCM saturation times and PV temperatures at these times extracted from the different PCM configurations used in simulations help to gauge their effectiveness at regulating PV temperature. However, a more meaningful metric that allows direct comparison of different configurations is required. This metric would measure the ability of the temperature regulation system to maintain low PV temperatures over the duration of the simulation. The cost function, J, is defined as follows:

$$J = \int_{t_i}^{t_f} \Delta T(t) dt \tag{2.2}$$

where t is time in seconds, t_i is the time at the start of the simulation, t_f is the time at the end of the simulation, and $\Delta T(t)$ is the difference between the PV temperature at time t and the initial condition of 25°C.

An ideal temperature regulation system would maintain a constant PV temperature equal to the initial condition of 25°C. This system would have zero total cost over the simulation time interval. The best PCM container configuration would be the one with minimal deviation from ideal, and thus, minimal cost.

The PV temperature data obtained from the numerical simulations is in discrete, unequal time-steps. The cost function is therefore modified to perform a numerical integration of the available data using the trapezoidal rule.

$$J = \frac{1}{2}\sum_{k=1}^{N}(\Delta T_{k+1} + \Delta T_k)(t_{k+1} - t_k) \tag{2.3}$$

In Equation 2.3, J is the total cost for $N + 1$ data points, k is the index number, t is time, and ΔT is the PV temperature minus 25°C.

Chapter III

Results

From the transient simulations set up in ANSYS, temperature data is collected at the marked locations and sites explained in the previous chapter. By plotting this data versus time, the effectiveness of different PCM configurations at regulating PV temperature can be seen. Also, by collecting temperatures of different locations within the PCM container, the melt patterns of the PCM can be understood and used to improve the design of the container for better temperature regulation.

3.1 Bulk PCM

This design consists of the aluminum container filled with PCM and the lid attached to the back surface of the PV panel.

3.1.1 Two-Dimensional Model

Three different depths of the PCM container are modelled as 2D geometries. Temperature contour plots of this model show that there is one-dimensional heat flow from the PV surface down to the bottom plate of the PCM container. Figure 3.1 shows this plot for a container of depth 1". The last part of the PCM block to melt is thus found to be at location $L2$, shown in Figure 2.4. Table 3.1 summarizes the results for the three cases.

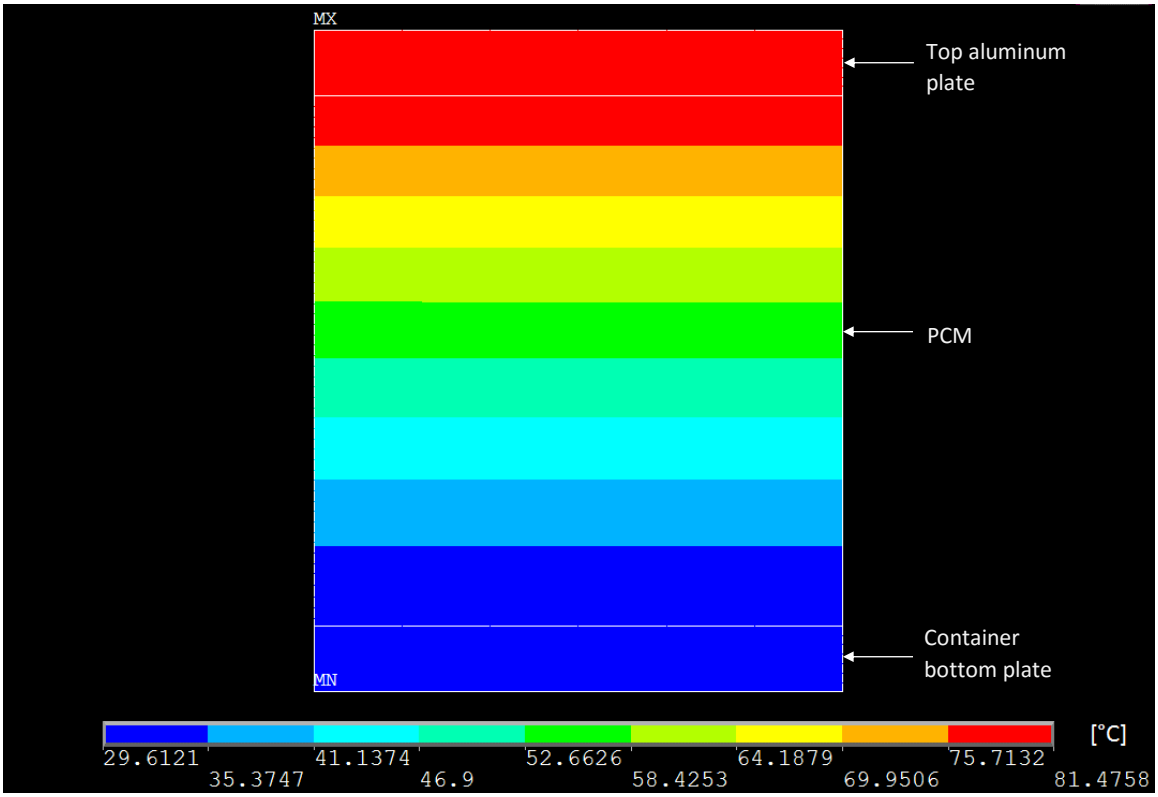

Figure 3.1: Temperature contour plot at PCM saturation of a 2D geometry of the bulk PCM configuration. MX and MN indicate the maximum and minimum temperatures at that time, respectively.

Table 3.1: Results from different depths of container modelled as 2D geometries for bulk PCM configuration.

Depth, d $[in]$	**L1 temperature @ 5 hours** $[°C]$	**L2 PCM saturated** $[hh:mm]$	**L1 temperature @ L2 saturation** $[°C]$
1/3 (8.467 mm)	298.9	01h:02m	47.2
1/2 (12.7 mm)	229.6	01h:34m	56.1
1 (25.4 mm)	128.3	03h:20m	81.5

Table 3.1 shows that as the depth of the container is increased, at the end of simulation at 5 hours the PV temperature is kept much lower because the amount of PCM available to absorb incoming heat increases. It takes longer for deeper containers to achieve full PCM saturation, which is a desirable trait for the passive temperature regulation system. But, at the time of saturation, the PV temperature is higher. This is

because the low thermal conductivity of PCM causes heat to accumulate close to the PV surface and raise the local temperature. Still, at all times during the simulation, the container with depth 1” maintains the lowest PV temperature, as seen in Figure 3.2.

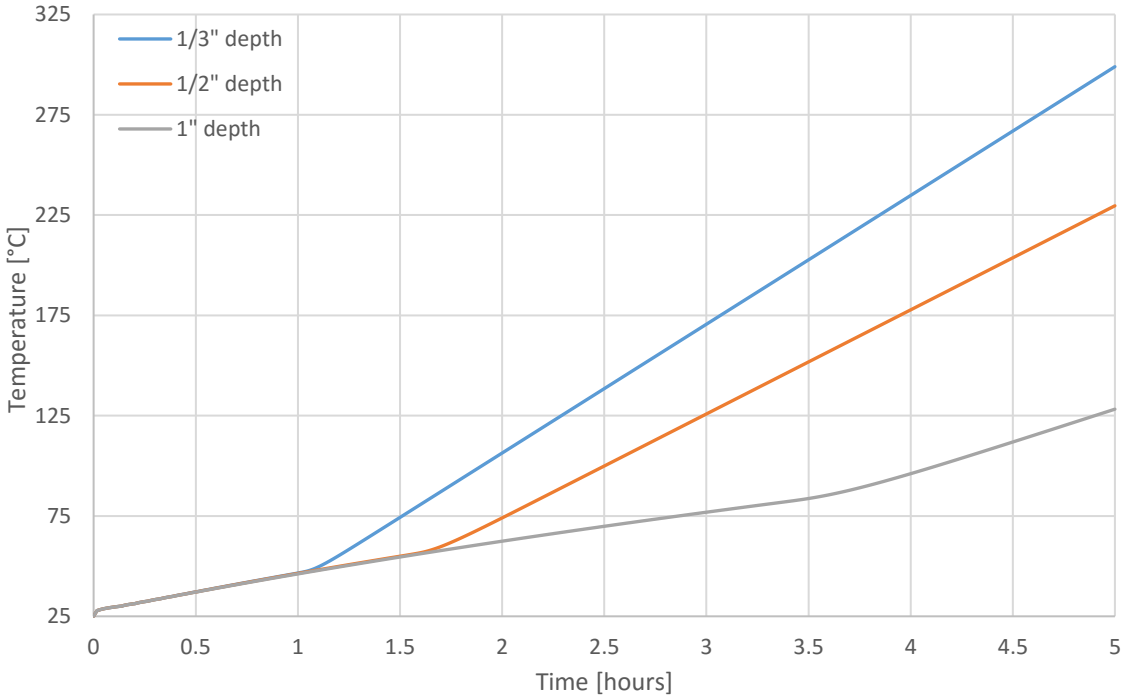

Figure 3.2: Plots of PV temperature versus time for different depths of the PCM container.

While deeper designs would be preferable since they take a longer time to saturate and keep the PV cooler, a way to further lower the PV temperature while the PCM melts is needed.

3.1.2 Three-Dimensional Model

The 2D model of the bulk PCM container assumed that end effects from the container sidewalls would not play a major part in the absorption of heat by the PCM.

Thus, that modelling approach assumes one-dimensional heat flow. In order to determine how accurate this assumption is, a 3D model of the container with 1” internal depth is simulated with the same initial and boundary conditions. Temperatures are collected at three different sites (see Figure 2.6) at varying distances from the container sidewalls, and then compared to the results from the 2D model.

When temperature histories of locations $L1$ and $L2$ from different sites in the 3D model are compared to the 2D results, very large differences, up to 31°C, are seen. The differences are very slightly smaller at site $S3$, which is the geometric center of the container. Figure 3.3 shows plots of the PV temperature (location $L1$) from the three sites of the 3D model, and the 2D model.

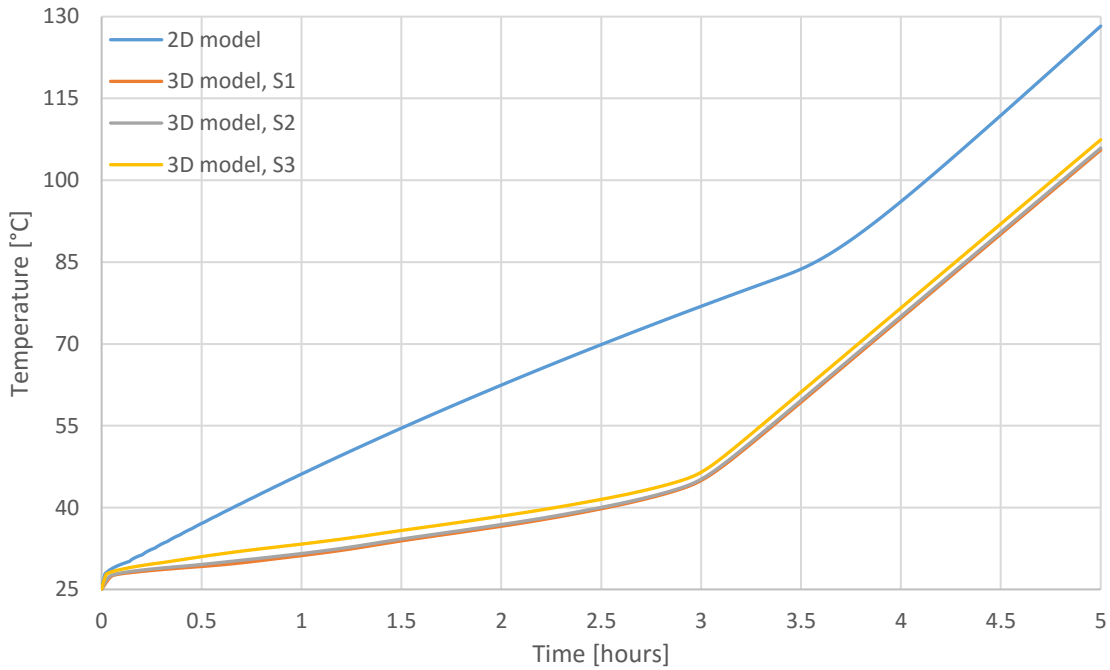

Figure 3.3: Plots of PV temperature versus time for the 2D model and 3 sites of the 3D model of bulk PCM configuration. A container of depth 1” was used to obtain this data.

In Figure 3.3, the PV temperature rises with a much higher slope during PCM melt in the 2D case because the incoming heat is accumulated within the top layers of PCM. The same was expected of the 3D model, but a lower initial slope is seen. This is because of the way the models are set up. While the 2D setup assumes an infinitely large box, with the only contact between top and bottom through the PCM filling, the 3D setup has the top and bottom walls of the container connected at the outer boundaries with the aluminum sidewall. Due to aluminum's high thermal conductivity, the sidewall effectively provides a low resistance path for the heat to travel down from the incoming flux at the top surface to the bottom surface.

This affects the way heat is distributed into the PCM, resulting in different shapes of the temperature contours at full PCM melt time. The 2D case isotherms (see Figure 3.1) suggest that the bottom layer of PCM, next to location $L2$ will be the last to melt. But, due to the sidewall connection between the top and bottom plates in the 3D case, the PCM close to the halfway depth in the container is the last part to melt. This can be seen in Figure 3.4.

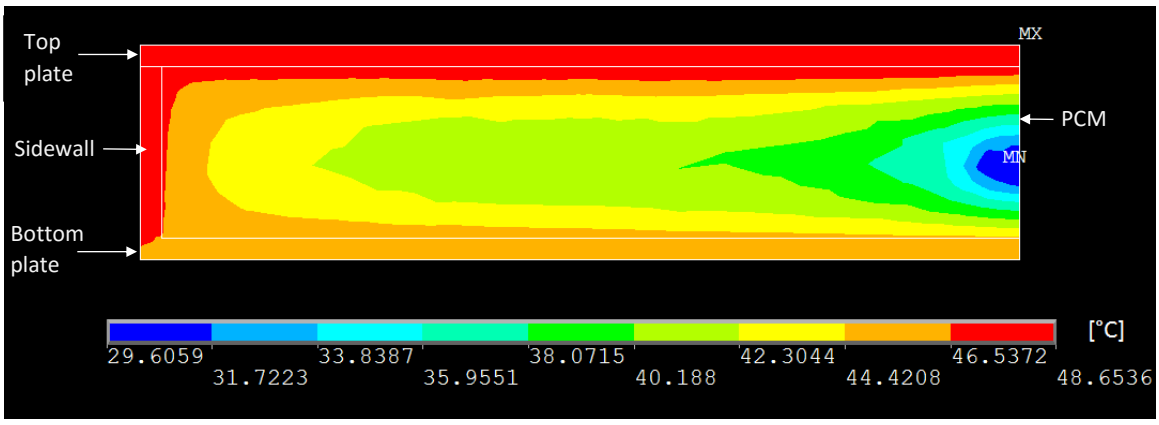

Figure 3.4: Temperature contours of the 3D model of the bulk PCM container at PCM saturation time. The difference in shape from the 2D model contours in Figure 3.1 point to a different melt pattern.

A better agreement between the 2D and 3D models would be seen if the container were made of a material with low thermal conductivity, such as HDPE. For the current design of an aluminum container, the results of the 3D simulation are more reliable. The 3D simulation shows that with a container of internal depth of 1”, full PCM saturation occurs after 3 hours and 6 minutes; the PV temperature at this time is 49°C.

The conclusion made from the 2D simulations about greater container depth regulating PV temperature for longer still holds. Thus, for all the following configurations investigated, the internal depth of the PCM container is fixed at 1”. Also, as shown by the comparison between 2D and 3D geometries, connecting the top and bottom plates of the container with a high thermal conductivity material is beneficial to the temperature regulation system. Hence, straight aluminum fins in the container will be explored next.

3.2 Container with Straight Fins

In order to distribute heat evenly into the PCM volume to lower PV temperature during the melt phase of PCM, straight aluminum fins are added to the container. These fins are attached to the top plate that is in contact with the PV panel.

3.2.1 Two-Dimensional Model

Three different cases of the finned container are modelled as 2D geometries. In these cases, the length, width and spacing between fins are varied to study the effect on PV temperature. In the reduced domain 2D geometry that utilizes symmetry, only one fin is modelled at the center of the PCM block.

3.2.1.1 Case I

The length of the aluminum fins is varied between 0 mm (no fin; geometry is identical to bulk PCM configuration) and 25.4 mm (fins connect top and bottom plates of the container). Plots of PV temperature (location $L1$) for selected fin lengths are shown in Figure 3.5.

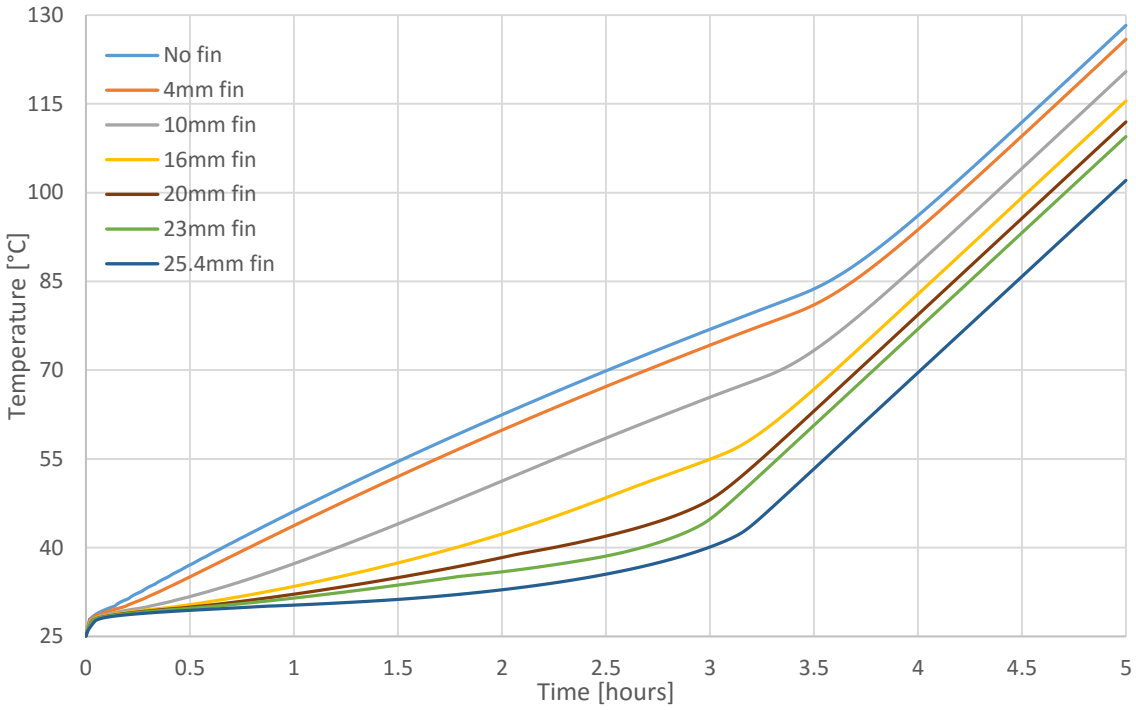

Figure 3.5: PV temperature versus time for varying fin lengths obtained from the 2D model of finned container.

In the above graph, all plots start with a high initial slope, where the PCM close to the PV heats up quickly. Once the PV (and the surrounding PCM) temperature reaches 27.6°C, the PCM layers begin to melt and the slopes decrease. Then, once all the PCM in the block is saturated, the slopes shoot up again and are equal because the effects of latent heat of the PCM are used up.

While the PCM melts, the slopes are higher for shorter fins, and reach the final knee at higher PV temperatures and longer times. Due to poor thermal conductivity of the PCM, local PCM close to the PV saturates very quickly and gets superheated while the PCM further down in the block gets only small amounts of heat. This is confirmed by trends seen in plots of location $L2$, in Figure 3.6.

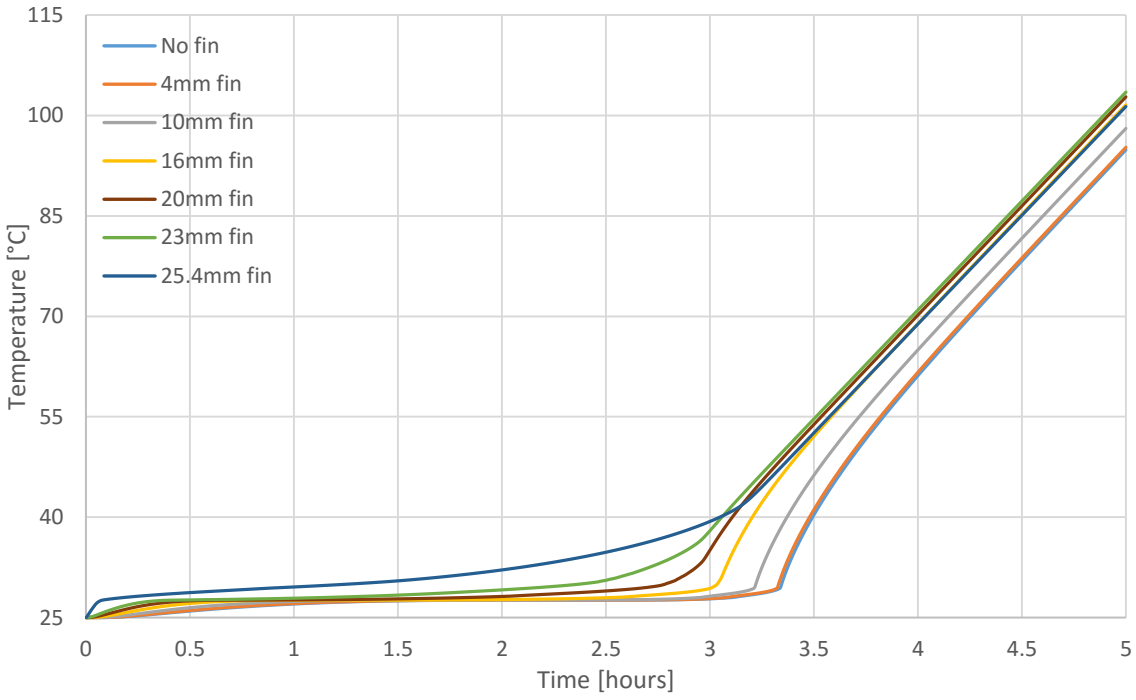

Figure 3.6: Plots of location $L2$ (inside bottom surface) versus time for varying fin lengths.

For 0 mm fin, and other short fins, the bottom surface temperature plots have an almost zero slope during PCM melt, shooting up immediately when they hit the melt temperature of 29.6°C. This trend becomes less drastic and the initial slope increases as the fin length is increased; the change in slope afterwards still exists, but

happens gradually, and at a temperature above 29.6°C. The 1” fin design exhibits this knee in the graph at around 43°C.

Figure 3.6 indicates that with increasing fin length, PCM at the bottom of the container is not the last to saturate. For the longer fins, even when the $L2$ temperature exceeds the melt range, incoming heat is still being used up to melt PCM elsewhere, and thus no sudden spike is seen in the temperature plots at 29.6°C.

Temperature contours of geometries with different fin lengths at full PCM melt are shown in Figure 3.7. As the fin length increases, the last part of PCM to saturate shifts upwards from the bottom surface. For the 1” long fin, with connects top and bottom aluminum plates, location $L6$ is where the melt process ends, making the temperature distribution almost perfectly symmetric along the depth of the container.

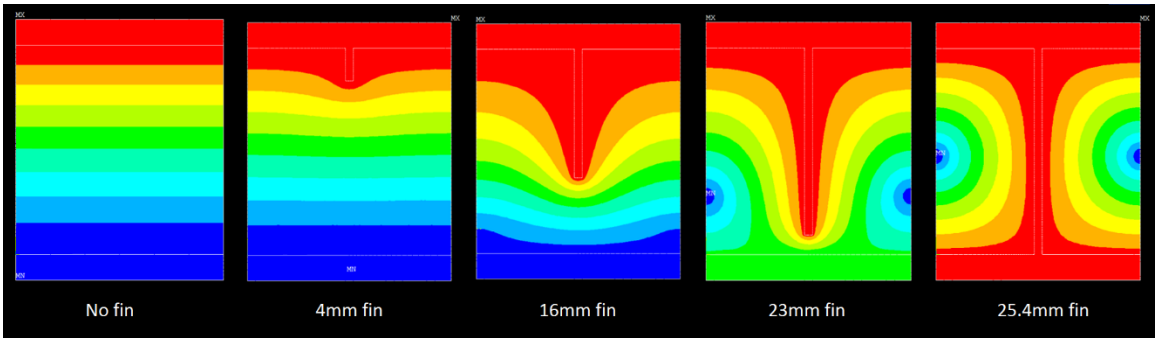

Figure 3.7: Temperature contours at PCM saturation time for different fin lengths. Red represents the hottest temperature, and blue represents the coldest temperature.

The more even distribution of heat in geometries with longer fins leads to lower PV temperature throughout the simulation. One hour into the simulation, the difference in PV temperatures (see Figure 3.5) between shortest and longest fins is 16°C. The greatest temperature difference is 36°C at around 3 hours. At the end of simulation, the 25.4 mm

fin design has a PV temperature 26°C lower than the no fin (0 mm) design. A combination of lower PV temperature and higher bottom surface temperature at all times in the simulation indicates that with longer fins heat is being more effectively moved away and used to melt PCM away from the PV surface. Shorter melt times and lower PV temperatures are thus the trend seen in Figure 3.8.

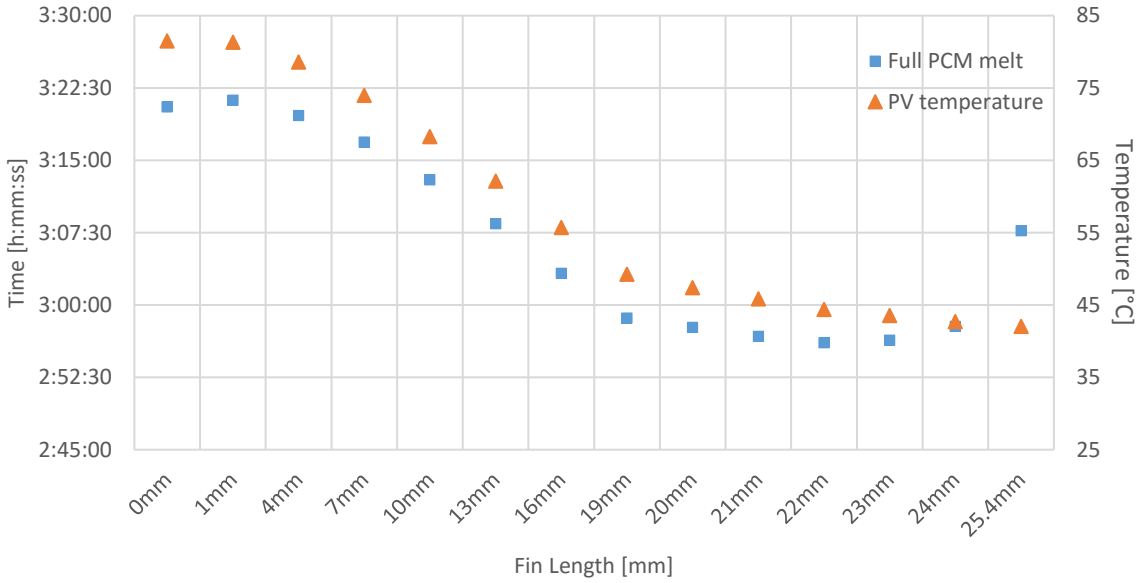

Figure 3.8: PCM saturation time and corresponding PV temperature for different fin lengths.

With increasing fin length, PCM saturation time also decreases due to a combination of two effects. First, a greater part of the incoming heat is carried down into the PCM block at all times by a longer fin. This brings the PCM closer to saturation at an earlier time. Second, the area of PCM in the 2D block decreases, which decreases the amount of thermal mass that can absorb heat without changing temperature.

An interesting result is seen for the longest fins, where the melt time goes up again, and significantly for the 1” long fin that connects top and bottom plates of the

container. This is explained by considering how the incoming heat is distributed throughout the geometry. In designs with short fins, heat flow is almost perfectly one-dimensional. The bottom part of the PCM is always the coolest region of the block. The bottom plate of the aluminum container, which is only in contact with PCM also stays at the same temperature as the PCM next to it. But, for fins of length 1", the bottom plate is thermally connected to the top plate through the fin. The fin provides a low resistance path for heat to travel down the PCM block, as noted earlier. Thus, the bottom plate reaches high temperatures much sooner while the PCM melts. This is an effective use of the heat capacity of the aluminum bottom plate that allows for longer PCM saturation time.

3.2.1.2 Case II

In this case a fin of length 13 mm is modelled with a combination of varying width and spacing values. Since there are 16 designs investigated, results are presented by grouping them into constant fin width and constant fin spacing plots.

Constant spacing graphs are presented first. Each graph contains plots for four fin widths, ranging from 1 mm to 3.175 mm. Figure 3.9 shows plots of location $L1$ for different fin widths at constant spacing of 1.5". Plot of every fin width on this graph shows a common characteristic of the temperature rising fast initially, until it reaches around 27.6°C and the PCM layer close to the PV panel starts to melt. Then the slope decreases, as the latent heat is used up in changing phase. A second knee around halfway through the simulation is seen, where the slope increases again and PV temperatures rise

faster. This can be explained by all the PCM in the block completely melting, which leads to all the incoming heat now being used for raising the temperature.

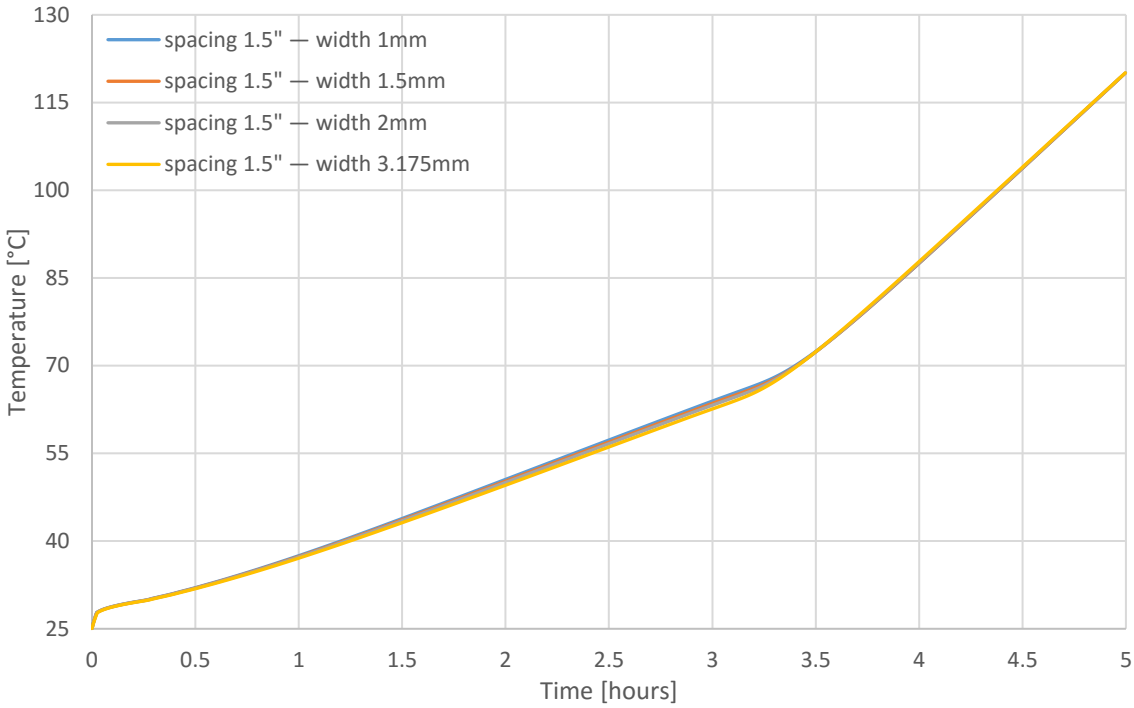

Figure 3.9: *L*1 temperature plots for finned container Case II. The fin length is held constant at 13 mm. This graph shows four fin widths arranged with the same spacing of 1.5".

PV temperature plots for Case II for other constant spacing values are shown in Appendix A. At the end of the simulation time of 5 hours, the smaller spacing plots end with lower PV panel temperatures. As spacing is increased, the PV surface ends up hotter. The final PV temperature falls between 114°C and 118°C for different fin widths with 0.5" spacing, and around 121°C for different fin widths with 2" spacing. This result shows that fins arranged close together are more effective at spreading the heat sideways; larger spacing designs are unable to do this because the low thermal conductivity of a larger amount of PCM on both sides of the fin hinders heat flow.

Figure 3.10 shows a graph with temperature plots of location $L5$ for this case with a constant fin spacing of 1.5". Graphs for other spacing values are shown in Appendix A. Fin widths are varied for different plots. All plots begin with a low slope, even though the PCM is not in the melt temperature range. This indicates that a very low amount of heat is carried over from the top part of the block to this bottom layer of PCM.

After this, once the temperature reaches around 27.6°C, the graphs become almost flat for a long time until the entire block of PCM melts. Once temperature at this location reaches 29.6°C, which marks the end of phase change, there is a sudden rise in slopes. This behavior indicates that PCM at location $L5$ is the last to saturate, and is confirmed from the temperature contours at full PCM melt.

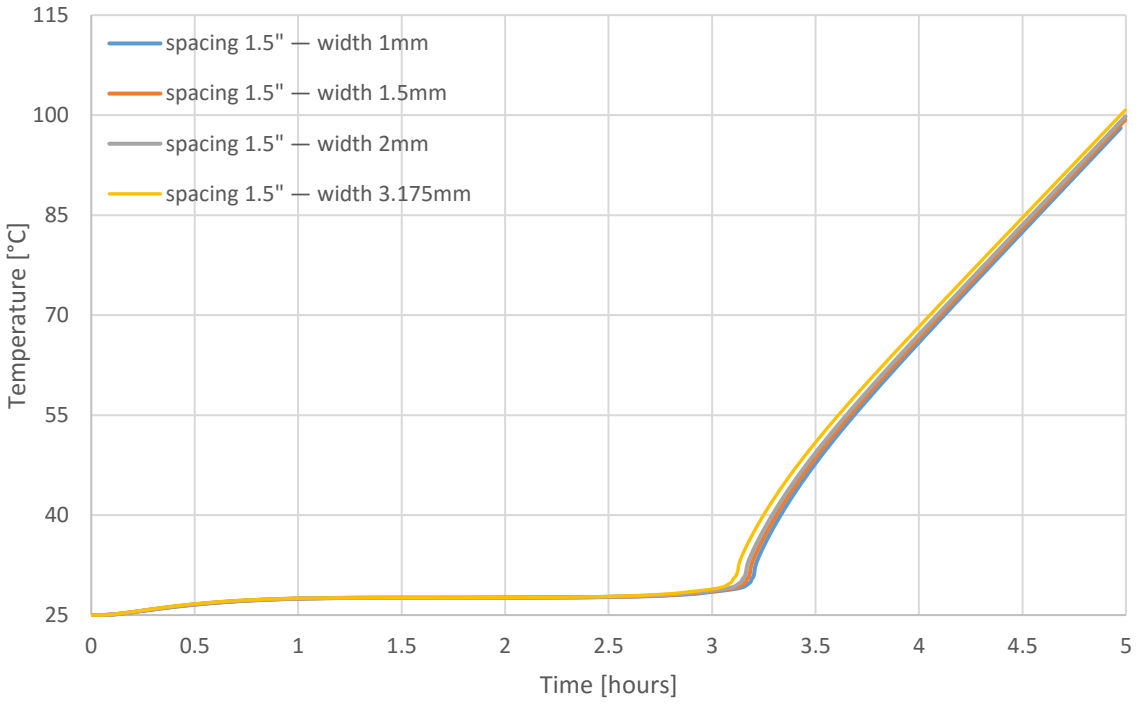

Figure 3.10: $L5$ temperature plots for finned container Case II. The fin length is held constant at 13 mm. This graph shows four fin widths arranged with the same spacing of 1.5".

Figures 3.9 and 3.10, and other plots in Appendix A, show that for the same fin length of 13 mm and constant spacing, varying fin width has only a minor impact on the temperature plots. The shapes of the plots are almost identical, and they all lie on top of each other.

Results for Case II are now presented grouped together in constant fin width graphs. Each graph contains four plots, for fin spacing ranging from 0.5” to 2”. Figure 3.11 shows PV temperature plots for a constant fin width of 1.5 mm. The plots show that as the space between fins is increased, temperature of $L1$ rises with a higher slope during PCM melt. Final temperature is also higher for larger spacing designs. Similar graphs for other constant fin widths are shown in Appendix B.

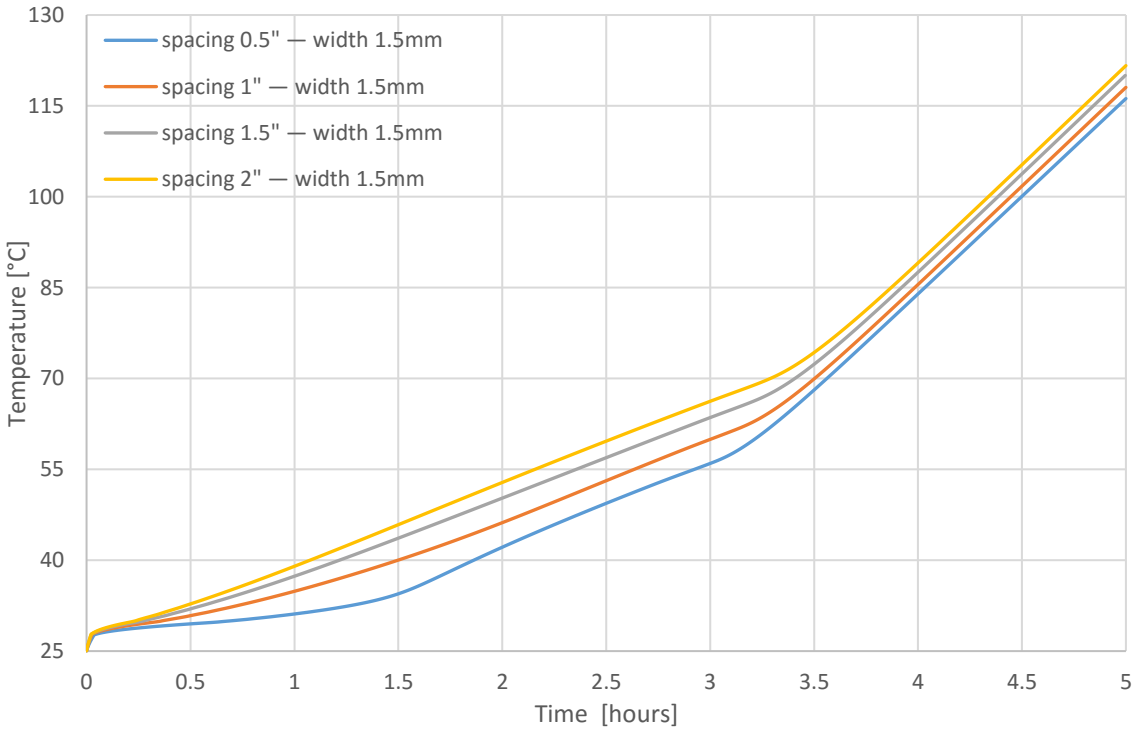

Figure 3.11: $L1$ temperature plots for finned container Case II. The fin length is held constant at 13 mm. This graph shows fins of width 1.5 mm arranged with four different values of fin spacing.

Plots of location $L5$, which is the last part of the PCM to melt, are shown in Figure 3.12. It is seen that the location of the last knee in the graph, which marks PCM saturation, varies with fin spacing – the smaller spacing designs have this knee at an earlier location than the others since more heat reaches down with fins stacked close together. Similar graphs for other constant fin widths are shown in Appendix B. These graphs show that when fin width is increased, the location of this knee moves gradually to an earlier time. This shows that wider fins are marginally better at carrying more heat to the bottom part of the PCM container.

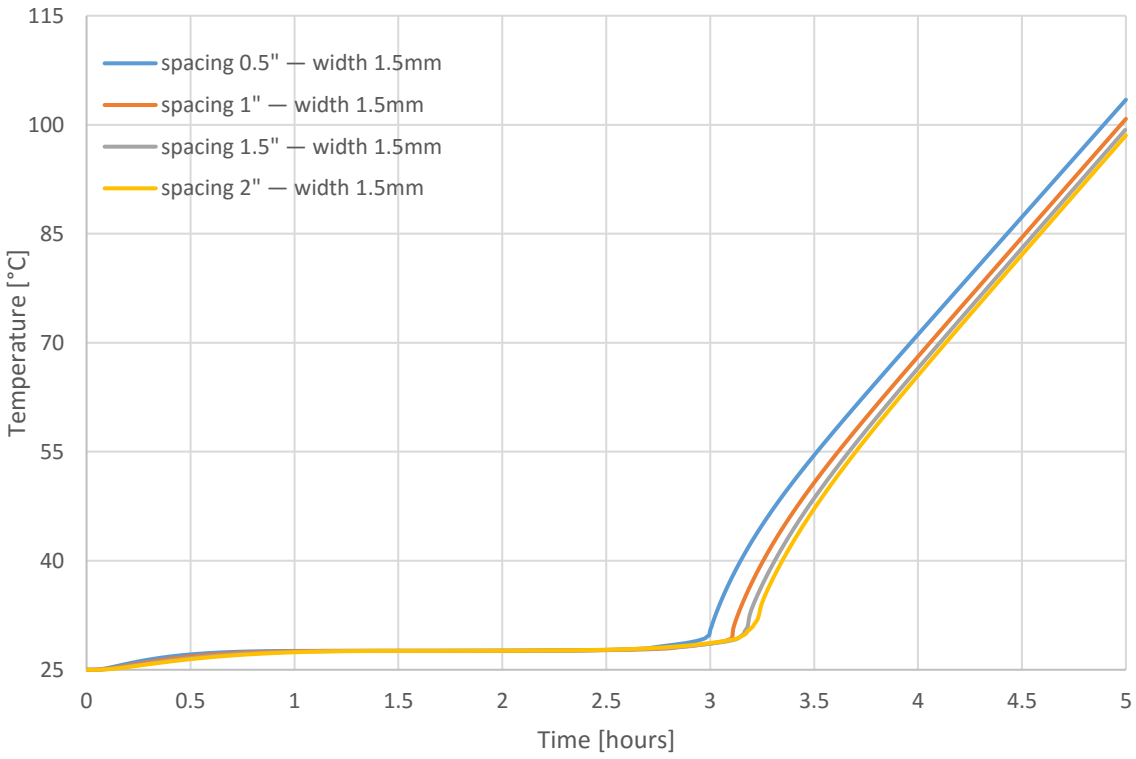

Figure 3.12: $L5$ temperature plots for finned container Case II. The fin length is held constant at 13 mm. This graph shows fins of width 1.5 mm arranged with four different values of fin spacing.

3.2.1.3 Case III

A fin of length 25.4 mm is modelled with a combination of varying width and spacing values. This fin connects the top and bottom plates of the container. Since there are 16 designs investigated, results are presented by grouping them into constant fin width and constant fin spacing plots.

Constant spacing plots are presented below. Figure 3.13 shows plots of PV temperature (location $L1$) for a constant spacing of 1.5” and varying fin width. Graphs for other constant spacing values are provided in Appendix C. In every fin spacing graph, the PV temperature with wider fins starts cooler, but around 2 hours into the simulation becomes hotter than designs with thinner fins. The slopes of the plots then increase when the PCM fully melts.

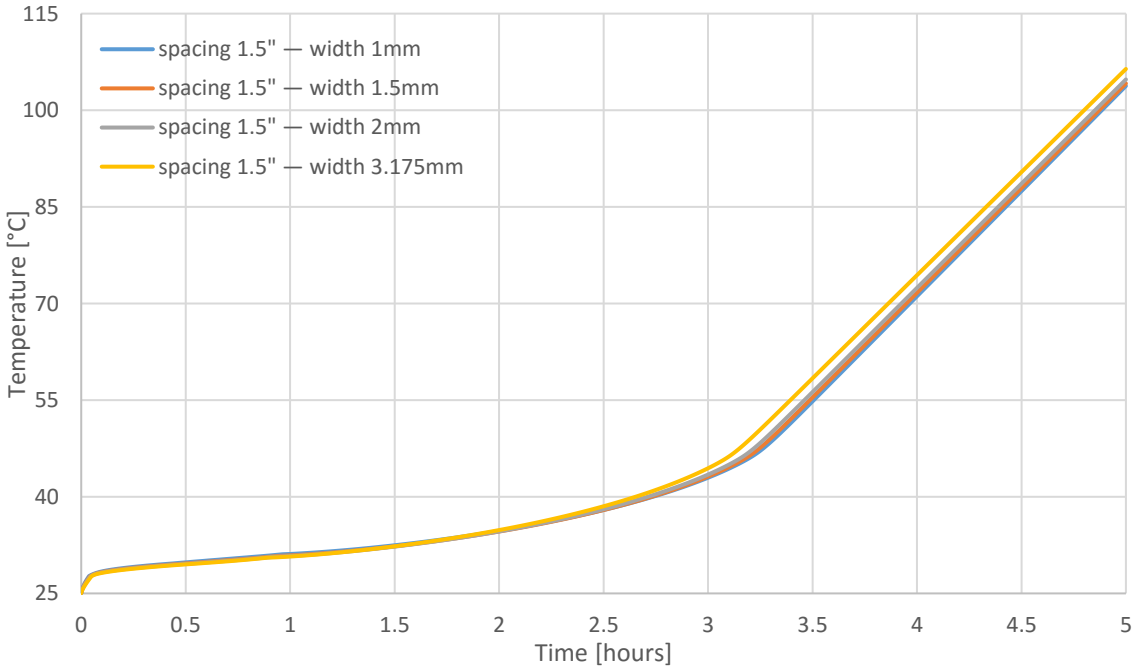

Figure 3.13: $L1$ temperature plots for finned container Case III. The fin length is held constant at 25.4 mm. This graph shows four fin widths arranged with the same spacing of 1.5”.

At the end of the simulation at 5 hours, the 3.175 mm fin always ends up with the hottest PV temperature due to reduced PCM in the block since a greater area is covered by a thicker aluminum fin. This difference in final $L1$ temperatures is more pronounced in the smallest fin spacing (0.5") graph, where the widest fin design ends 10°C higher than the thinnest fin. The difference becomes smaller and drops to 2°C as the fin spacing increases to 2". This happens because in the 2D geometry, changing fin width in larger spacing designs has a smaller effect on the ratio of PCM area to aluminum area.

When compared to the equivalent graphs for Case II (see Figure 3.9 and Appendix A), it is notable that the knee at full melt occurs at much higher PV temperatures for the 13 mm long fin plots than the 1" long fin. In Case II, the lowest knee occurs at 57°C and the highest knee occurs at 71°C. In Case III, the lowest knee is seen at a PV temperature of 33°C, while the highest knee is at 47°C. Thus, for all variations of fin spacing and fin width, the 13mm long fin does a worse job of taking the heat away from the PV panel. This results in a much higher slope of $L1$ temperature plots before the knee when compared to plots of 1" long fin.

Since the 1" fin of Case III connects top and bottom plates of the container, the last part of PCM to saturate is at location $L6$. Thus, temperature plots of this location, shown in Figure 3.14 and Appendix C, have the characteristic zero slope during phase change and a sharp knee at PCM saturation. Compared to the equivalent graphs of the last location to melt for Case II (see Figure 3.10 and Appendix A), there are differences in how the plots start. All Case II plots begin with a low slope, even though the PCM is not in the melt temperature range, indicating that very little heat reaches $L5$. In Case III, with

a longer fin, the plot slopes are high initially, and then decrease when the local PCM enters the melt phase. This indicates that comparatively more heat reaches the coolest part of the PCM block.

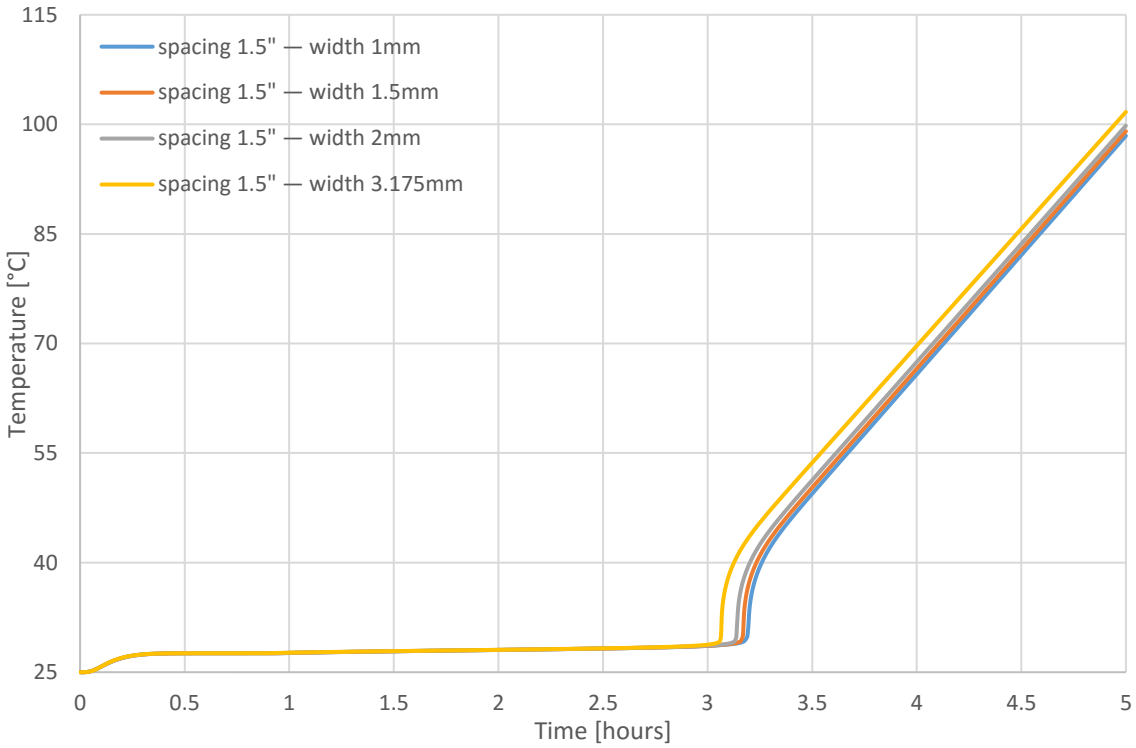

Figure 3.14: *L*6 temperature plots for finned container Case III. The fin length is held constant at 25.4 mm. This graph shows four fin widths arranged with the same spacing of 1.5”.

Temperature plots of locations *L*1 and *L*6 for Case III, grouped together in constant fin width graphs are shown in Appendix D. Trends similar to Case II are seen.

Results from all designs in Cases II and III of finned PCM container are now presented together. The differences in PCM saturation time and PV temperature at this time for all fin spacing and width combinations are shown in Figure 3.15.

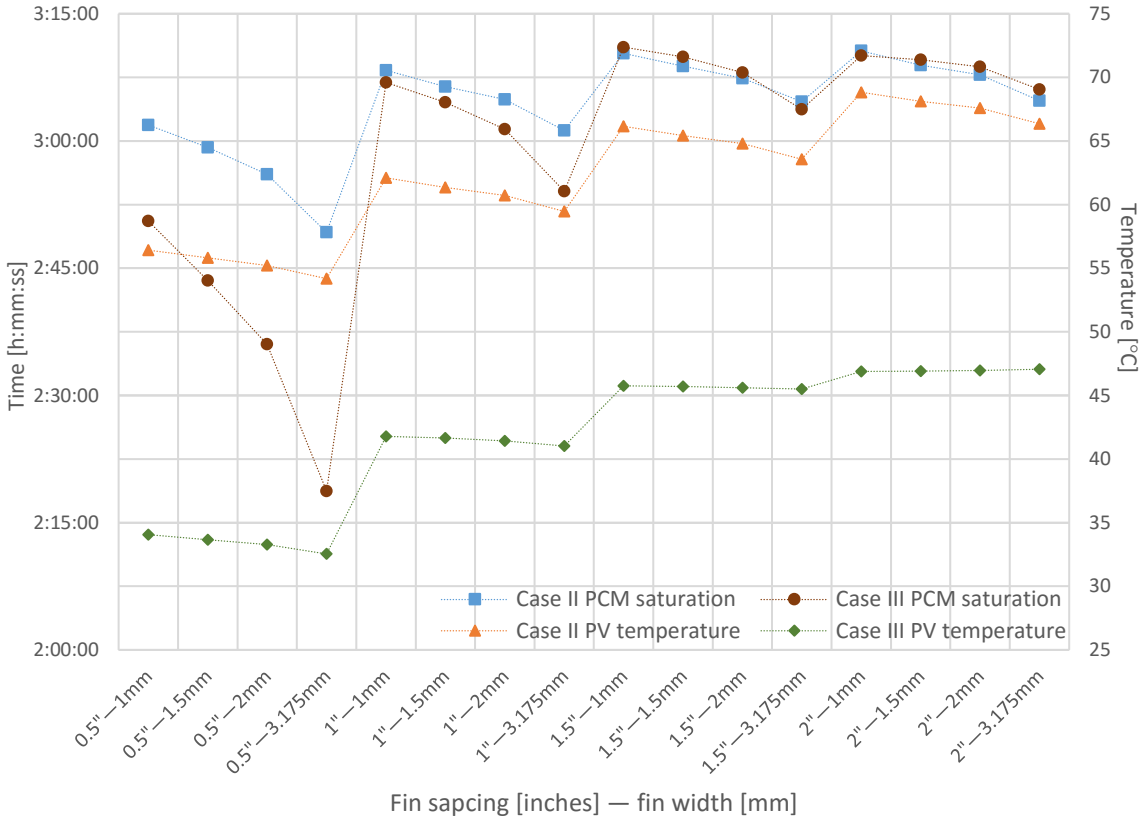

Figure 3.15: Plots of PCM saturation time and PV temperature at this time for varying fin width and spacing in Cases II and III.

For the same fin spacing, melt times drop slightly with increasing fin width due to a slightly reduced PCM area. This effect is more pronounced in smaller spacing designs because the PCM reduction has a greater effect on the area ratio of PCM to aluminum than in larger spacing designs. As fin spacing is increased, the area ratio of PCM increases, and so does the time to saturate.

Since 13mm long fins of Case II do a worse job of moving the heat away from the PV surface, it takes longer to saturate all the PCM in the block. A greater part of the incoming heat is thus used up in increasing the PV temperature. The combination of these two effects – locally accumulated heat and longer time to melt – leads to Case II designs

having a much higher PV temperature at full melt. For every combination of fin spacing and width, Case II PV temperature at saturation is around 22°C hotter than Case III.

As the fin width is increased, the PV temperature at melt is slightly lower because wider fins are marginally better at carrying heat away from the PV surface. When spacing is increased, the PV temperature at full melt goes up because the incoming heat has to travel through a wider area of low thermal conductivity PCM before saturation occurs.

Overall, for both Cases II and III, changing the fin width only has a minor effect on the regulation of PV temperature. For 13mm long fins and constant spacing, increasing fin width only decreases PV temperature at saturation by around 2.5°C. For 25.4mm long fins, this decrease is even smaller, at around 1.5°C. The accompanying reduction in PCM saturation time with increasing fin width makes thinner fins more suitable. Changing the spacing between fins has a more significant effect on the results – with increasing spacing the PV temperatures rise up.

Among all the designs modelled, Case II (fin length 25.4 mm) with a fin spacing of 0.5” has the lowest PV temperatures at full melt. With this spacing, PV temperature at saturation decreases by 1.5°C when fin width is increased from 1 mm to 3.175 mm. But, this also decreases PCM saturation time by 32 minutes. Hence, fins of length 25.4 mm, width 1mm and spaced 0.5” apart are deemed most effective for use in the temperature regulation system.

3.2.2 Three-Dimensional Model

Two geometries of the finned container configuration are modelled in three dimensions and the results compared to their respective equivalent 2D models. In both cases, the fins have a length of 1", and so the PCM is divided into separate blocks.

3.2.2.1 Case I

In this case, the fin width is 1 mm and fin spacing is 0.5". The temperature results from locations $L1$ through $L6$, collected at each of the 6 sites, $S1$ through $S6$ (see Figure 2.10), are plotted and compared graphically to results from the analogous 2D simulation. All throughout the 5 hours of simulation time the plots match closely. For every location, temperature plots from the 2D geometry are always slightly higher than plots from the 3D geometry. Figure 3.16 shows this trend in plots of location $L1$, where the 2D model ends with a slightly higher PV temperature by 5°C. This happens because the 3D model has some extra thermal mass of the container sidewalls that were not modeled in the 2D geometry. The temperature of these walls is also raised long with the PCM in the container, making them heat storage components.

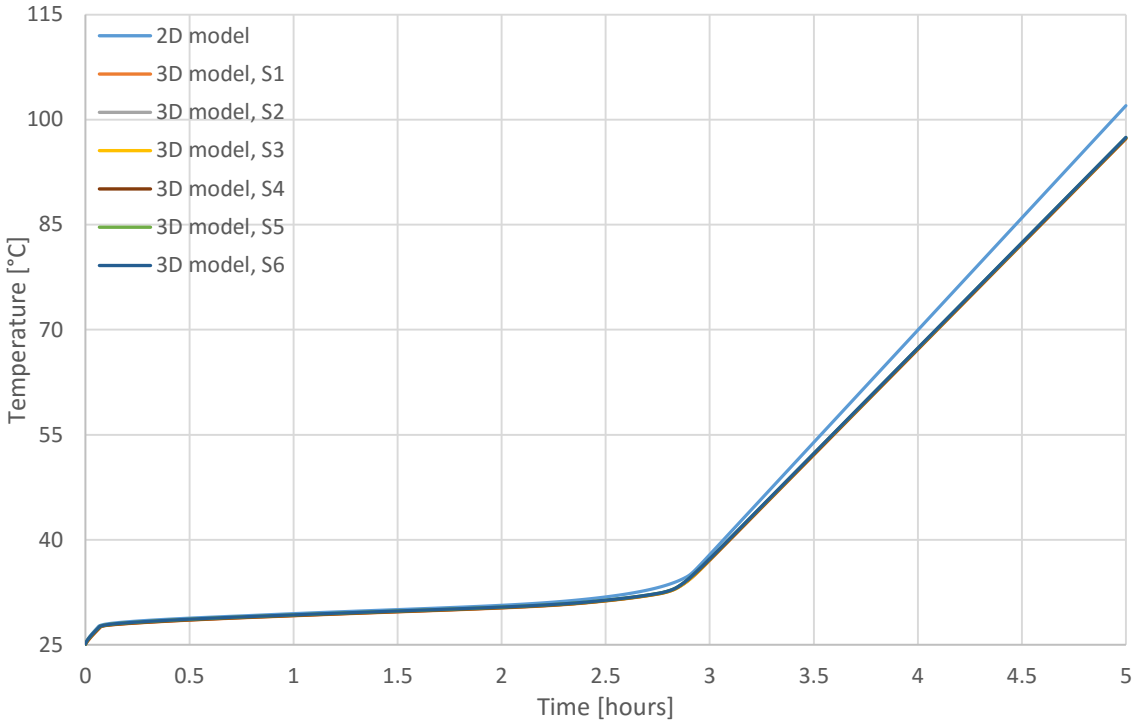

Figure 3.16: Temperature plots of location $L1$ obtained from the 2D model, and six sites of the 3D model.

Plots of all six sites from the 3D model are almost identical, indicating that heat is distributed evenly throughout the PCM container, and hence there is not much difference in where the data is collected inside the container. Thus, the use of symmetry to reduce the model to a 2D geometry is justified.

There is a slight variation seen in PCM saturation times between the six sites of the 3D model. In the PCM block adjacent to the container sidewall, PCM saturates first at site $S1$, then $S2$, and last at $S3$. Because site $S1$ is close to two container walls, the thicker sidewalls act as thick fins and bring slightly more heat from the top plate into the PCM. This causes PCM at this site to melt sooner. The effect of the second sidewall diminishes as the sites get closer to the middle of the PCM container. A similar trend is

seen in the PCM block in the center of the container, where PCM at site $S4$ melts first, then $S5$, and $S6$ last.

When melt times are compared between the two PCM blocks of interest, it is seen that PCM in the block adjacent to the sidewall saturates at a slightly later time. This occurs this due to the sidewalls of PCM surrounding it on three sides, which store a part of the incoming heat which would have otherwise gone into melting the PCM.

Table 3.2 compares the 2D and 3D models for PCM saturation time and PV temperature at this time. Very small differences are seen, as quantified by the percentage difference in PV temperatures at full melt.

Table 3.2: Results from Case I of 3D models for finned PCM configuration compared to equivalent 2D model.

	2D model	**3D model, S3**	**3D model, S6**
PCM saturation time $[hh:mm]$	02h:51m	02h:56m	02h:52m
PV temperature @ PCM saturation $[°C]$	34.0	35.5	33.7
Percent Difference		4.1%	-1.1%

3.2.2.2 Case II

In this case, fins of width 3.175 mm are arranged with a spacing of 1". Graphical comparison of temperature data from six locations at sites S1 through S6 with the 2D model results shows minimal differences. Between the six sites of the 3D model, trends similar to Case I are seen.

Table 3.3 presents results of PCM saturation time and PV temperature at this time. The results of the 3D model are compared to that of the equivalent 2D model, and a good agreement between the two modelling approaches is seen.

Table 3.3: Results from Case II of 3D models for finned PCM configuration compared to equivalent 2D model.

	2D model	**3D model, S3**	**3D model, S6**
PCM saturation time $[hh{:}\,mm]$	02h:54m	03h:01m	02h:56m
PV temperature @ PCM saturation $[°C]$	41.0	42.2	40.6
Percent Difference		2.9%	-1.0%

Overall, results from the finned PCM container show a marked improvement over the bulk PCM configuration. Fin length has the most significant impact on the regulation of PV temperature, with the longest fin providing lowest PV temperatures. With this fin length, PCM saturation time also increases, which is a break from the trend of shorter melt times with increasing length. Fin spacing is next in importance, since changing it affects the farthest any point in PCM is from a high thermal conductivity heat flow path. Fin width has only a minimal impact on PV temperature. In fact, increasing fin width shortens saturation time, which is a negative effect on the temperature regulation system. Results suggest that long, thin fins with small spacing are most suitable for mitigating the effects of low thermal conductivity of PCM. A honeycomb structure, which matches these criteria, is investigated and results presented in the next section.

3.3 Container with Honeycomb Core Fin

An aluminum honeycomb core is modelled in the PCM container. The depth of the honeycomb is 1”, so it connects the top and bottom plates of the container. The PCM is also divided into cells, and temperature is monitored at four of the cells (see Figure 2.16). Results are compared to Case I and Case II of the 3D model of finned container configuration. Case I has fins of length 1”, width 1mm and spacing 0.5”. Case I has fins of length 1”, width 3.175mm, and spacing 1”.

3.3.1 Case I

In Case I, the cell size of the honeycomb is 1”. Temperature contours of all four PCM cells were plotted at full PCM melt, and were found to be similar. Figure 3.17 shows the temperature contours for cell TL. It can be seen that the honeycomb effectively carries heat away from the PV surface and distributes it evenly to the enclosed PCM cells because of the near symmetry in temperatures seen between the top and bottom halves of the model.

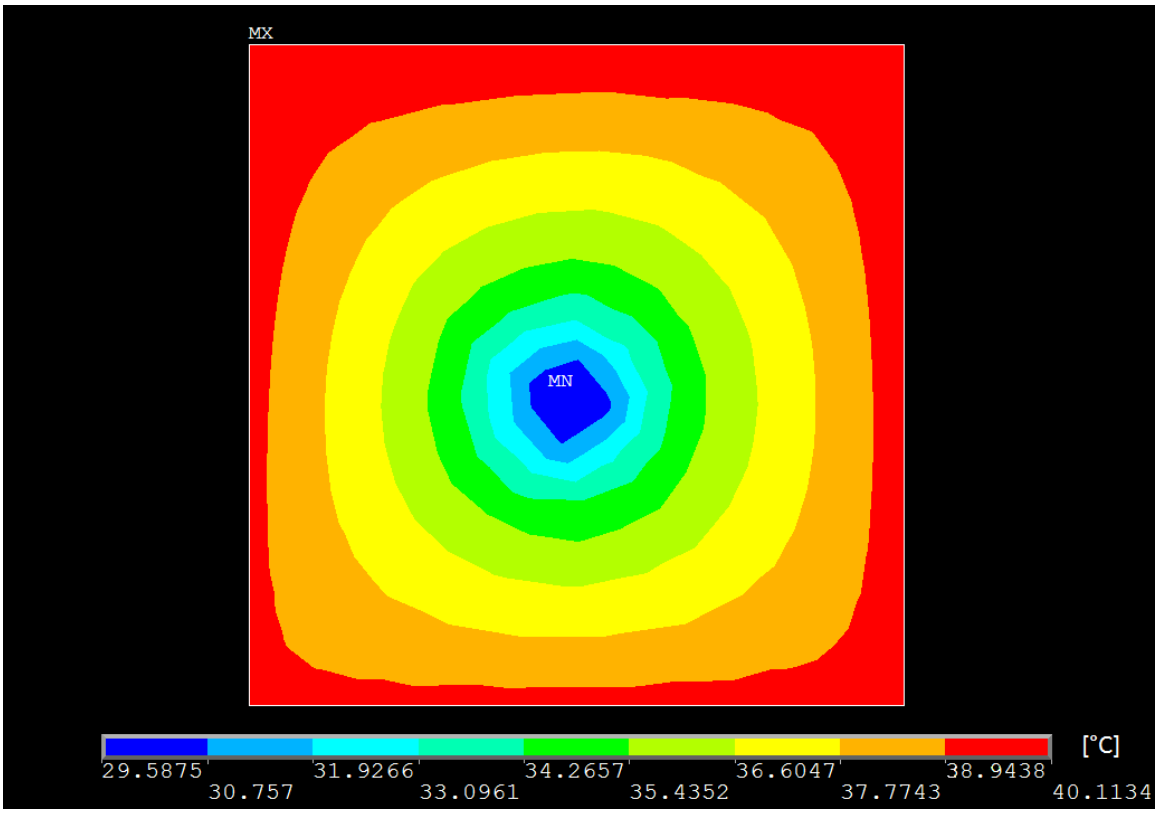

Figure 3.17: Temperature contours at full melt for honeycomb configuration Case I. Only the PCM cell is shown.

For each PCM cell, the last part of the PCM to melt is verified to be at or very close to the centroid, whose temperature is monitored as it is analogous to location *L*6 in Figure 2.11. This is also seen in the temperature plots of this location for all PCM cells, where the slope remains flat in the melt temperature range of the PCM, and once saturated, immediately increases. Figure 3.18 shows these plots of location *L*6 for the four PCM cells of the honeycomb configuration, and two 3D finned container models.

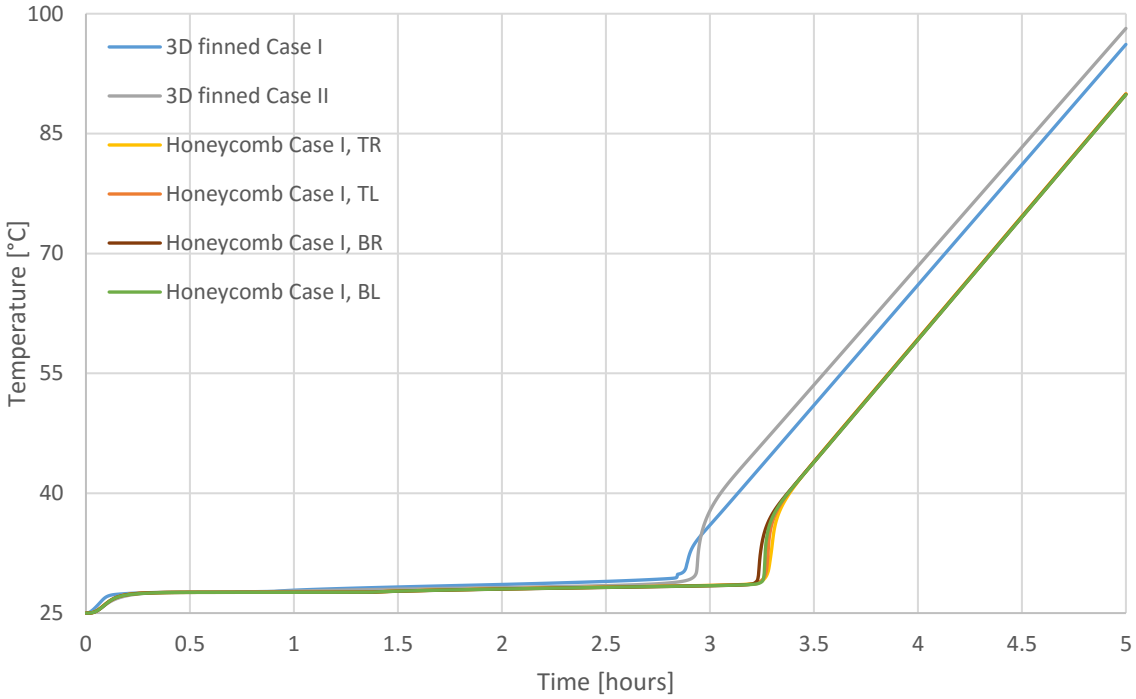

Figure 3.18: Temperature plots of location *L*6 obtained from the 3D cases of finned configuration, and four cells of the honeycomb configuration Case I.

The figure above shows that the two finned designs melt very close to each other. All PCM cells in the honeycomb configuration reach saturation last, and also have the lowest final PCM temperature. The difference in final temperatures of the PCM at *L*6 is around 10°C.

*L*1 temperature from the same configurations is plotted in Figure 3.19. Throughout the simulation time, the PV panel is almost always maintained at lower temperatures by using the honeycomb core rather than straight fins in the PCM container. At the end of simulation, the honeycomb configuration PV temperature is 92°C. This value is 5°C lower than the finned container Case I, and 9°C lower than the finned container Case II.

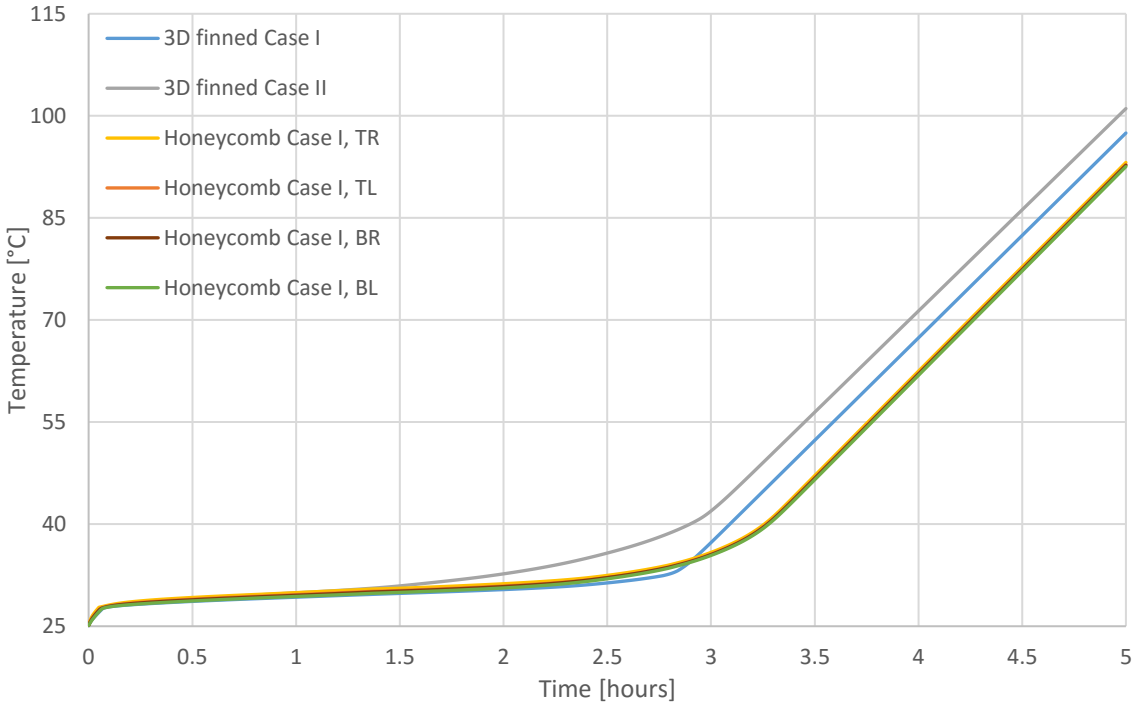

Figure 3.19: Temperature plots of location $L1$ obtained from the 3D cases of finned configuration, and four cells of the honeycomb configuration Case I.

A comparison of PCM saturation time and the PV temperature at this time for the two finned 3D designs and the honeycomb Case I is shown in Table 3.4. It is seen that finned container Case I melts soonest, and the PV temperature at this time is the lowest. Finned container Case II saturates next. Even though this design melts slightly later, the gains in melt time come with a higher PV temperature at full PCM melt. The honeycomb PCM cells have the longest saturation time of 3h:17m. This due to the extra volume of PCM in the container made possible by the very small thickness of the honeycomb of 0.2 mm. This melt time is an improvement of 21 minutes and 16 minutes over finned container Cases I and II, respectively. At full melt, the PV temperature is 40.9°C, which is higher than that of finned container Case I. But, it is seen from Figure 3.19 that at the same time, that design has reached a PV temperature of 46.1°C.

Table 3.4: Results from two 3D cases of finned PCM configuration compared to honeycomb configuration Case I.

	3D finned Case I	**3D finned Case II**	**Honeycomb Case I**
PCM saturation time $[hh:mm]$	02h:56m	03h:01m	03h:17m
PV temperature @ PCM saturation $[°C]$	35.5	42.2	40.9

3.3.2 Case II

In Case II, the cell size of the honeycomb is 0.5". This case is modelled to see if a smaller honeycomb cell size (effectively reducing fin spacing) has the same significant effect on PV temperature as it did with straight fins. Temperature contours of the monitored PCM cells are again very similar, with an even heat distribution seen. The last part of every PCM cell to saturate is again at location $L6$.

Figure 3.20 shows $L1$ temperature plots from two 3D finned container designs and honeycomb Case II. All plots from the honeycomb configuration fall on top of each other, suggesting that the location of the PCM cell in the container does not matter. Throughout the simulation, the honeycomb configuration has the lowest PV temperatures. At the end of the simulation, the PV temperature for Case II of honeycomb configuration is 93°C. This is 4°C lower than the first finned container Case I, and 8°C lower than the finned container Case II.

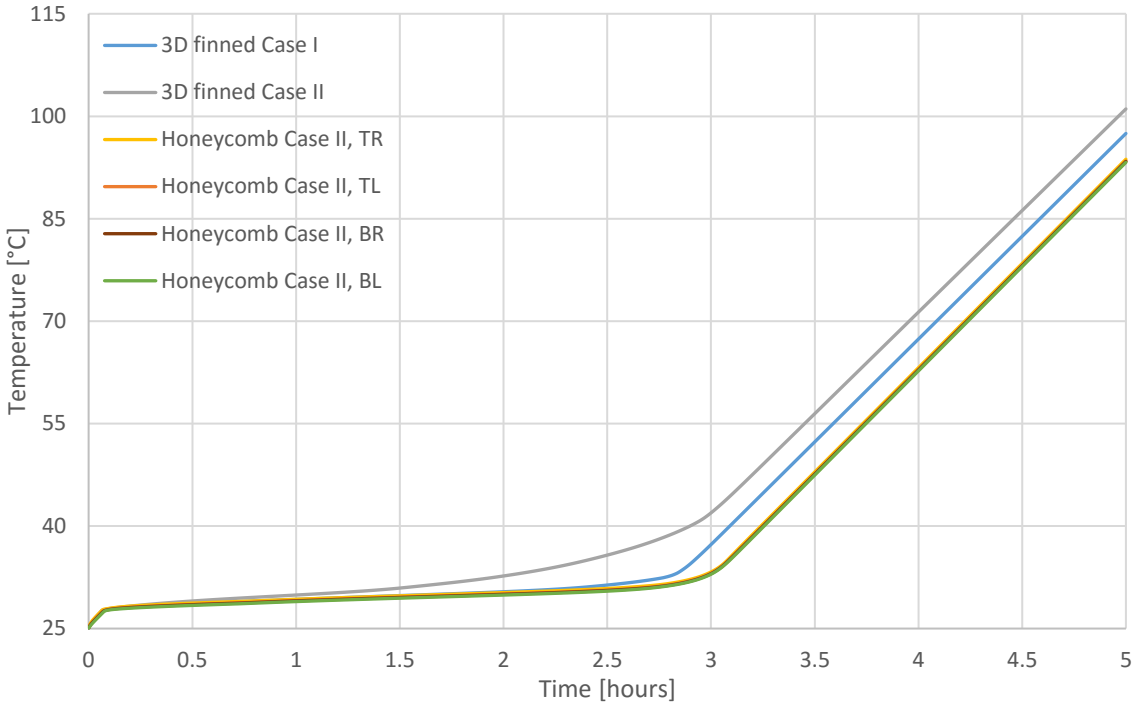

Figure 3.20: Temperature plots of location $L1$ obtained from the 3D cases of finned configuration, and four cells of the honeycomb configuration Case II.

Table 3.5 shows PCM saturation time and PV temperature at this time for honeycomb configuration Case II. When compared to the two finned designs, this design gives a melt time improvement of 6 minutes over Case I, and 2 minutes over Case II. These gains are smaller than were seen in honeycomb configuration Case I. A larger improvement is seen in PV temperature at PCM saturation. The PV temperature at melt is lowered by 1.5°C and 8°C when compared to finned container Cases I and II, respectively.

Table 3.5: Results from two 3D cases of finned PCM configuration compared to honeycomb configuration Case II.

	3D finned Case I	**3D finned Case II**	**Honeycomb Case II**
PCM saturation time $[hh:mm]$	02h:56m	03h:01m	03h:03m
PV temperature @ PCM saturation $[°C]$	35.5	42.2	34.1

Comparing the two honeycomb configuration cases, all PCM in Case II saturates 15 minutes sooner than in Case I. This is because smaller sized honeycomb cells reduce the amount of PCM in the container. Shorter melt time of Case II is also accompanied by a 6.8°C lower PV temperature at full melt.

3.4 Encapsulated PCM

In this configuration, spherical HDPE pellets containing PCM are placed inside the container. The remaining volume of the container is filled with water. Temperature contours of the quarter model at PCM saturation, shown in Figure 3.21, show that the center of the container has highest temperatures and longest melt time. Thus, temperature data was only collected at this site.

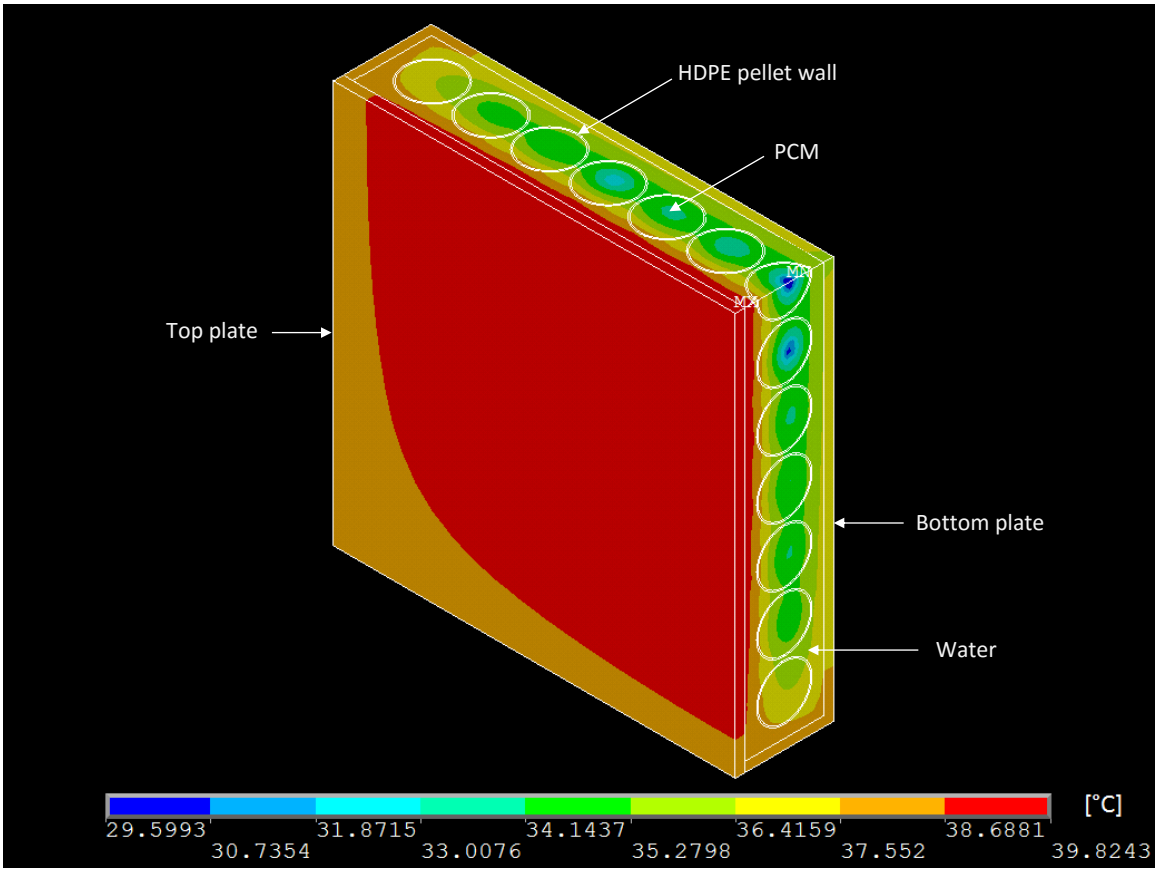

Figure 3.21: Temperature contours at PCM saturation time for quarter model of encapsulated PCM configuration.

A plot of PV temperature versus time from this configuration is shown in Figure 3.22, along with two 3D finned cases. The plot starts with a high slope, similar to other configurations. During PCM melt, the slope for encapsulated PCM configuration is higher than the rest. This happens because in this configuration the volume of PCM in the container is substantially reduced. Once all PCM inside the pellets has saturated, the plot slope increases again by a small amount. This final slope is much lower than other configurations after PCM melt because a large part of the container volume is occupied by water, which has a very high specific heat capacity.

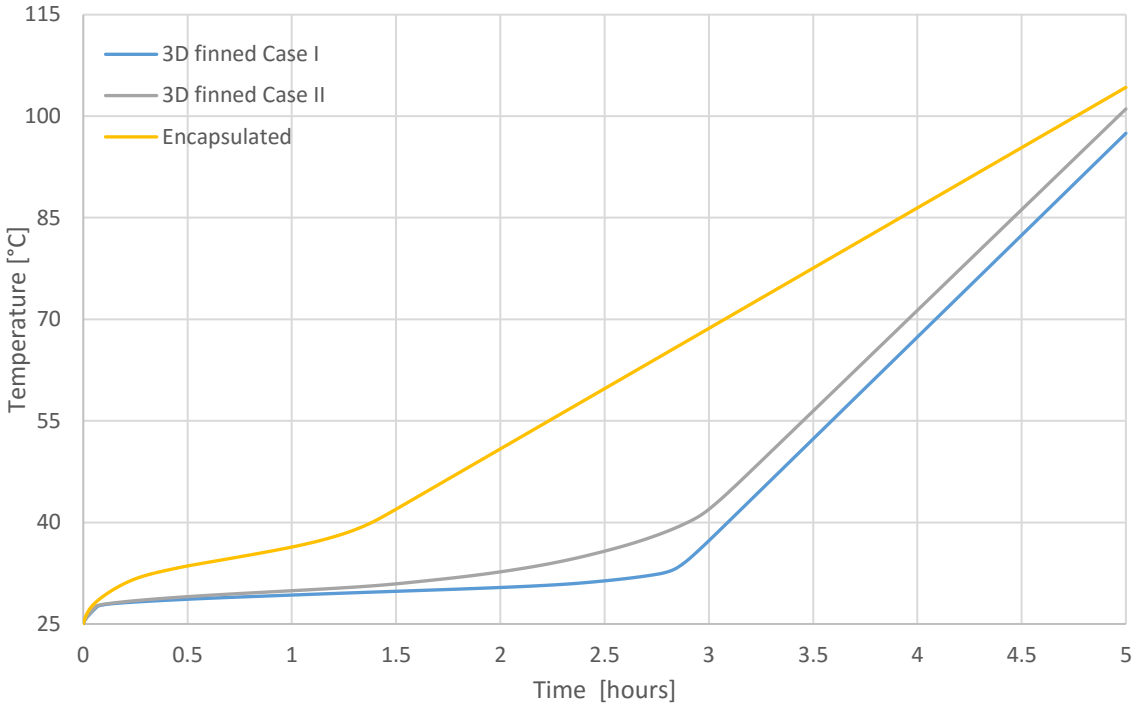

Figure 3.22: Plot of PV temperature versus time for encapsulated PCM configuration.

PCM in the encapsulated configuration saturates after 1 hour and 22 minutes. The PV temperature at this time is 39.8°C. Almost every other container configuration modelled has a lower PV temperature at this time.

3.5 Cost Comparison

Plots of PV temperature versus time for a few selected configurations are compiled in Figure 3.23.

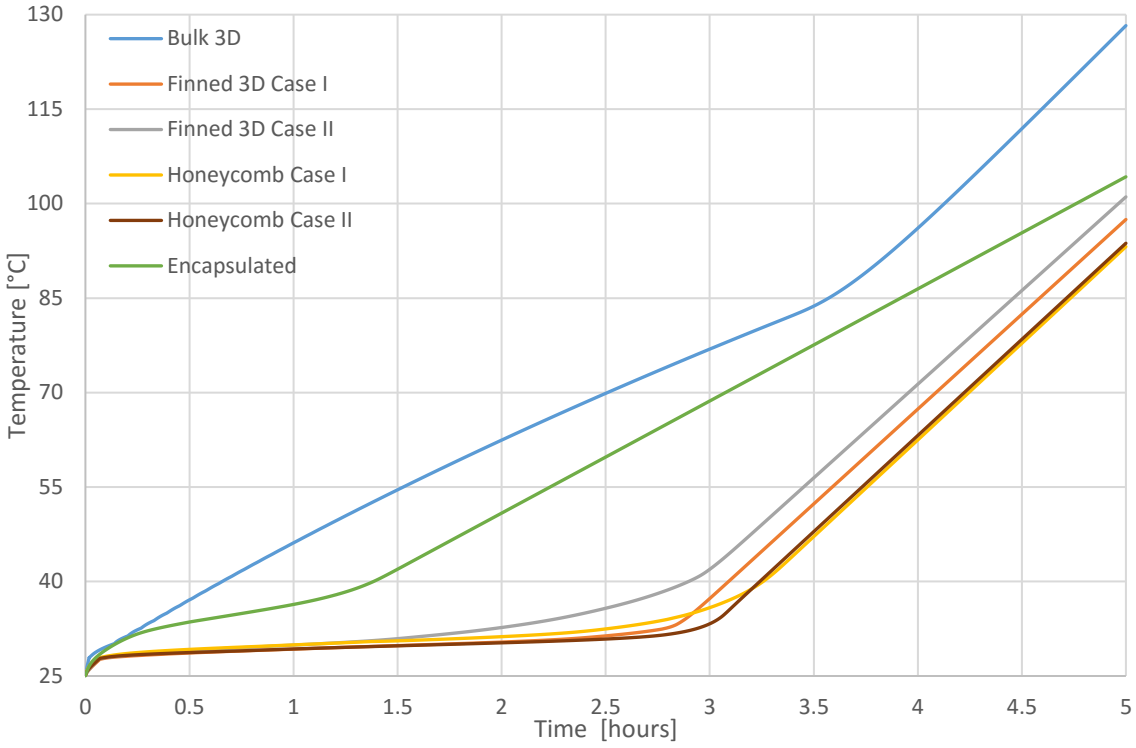

Figure 3.23: PV temperature plots for different PCM container configurations.

A wide variation in saturation times and PV temperatures is seen. To compare the performance of the configurations directly against each other, the cost of each configuration is computed using Equation 2.3. The results are shown in Table 3.6.

Table 3.6: Costs for various container configurations.

PCM Container Configuration	**Cost, J $[°C \cdot s]$**
Bulk 3D	839,003
Finned 3D Case I	359,950
Finned 3D Case II	409,631
Honeycomb Case I	334,469
Honeycomb Case II	326,978
Encapsulated	659,470

Table 3.6 shows that when compared for a five-hour time period, a PCM container with a honeycomb fin with 0.5” cell size is most effective at maintaining low PV panel temperature over a long duration. Very close performance is also seen from honeycomb of 1” cell size, and a straight fins of length 1”, width 1 mm, and spacing 0.5”.

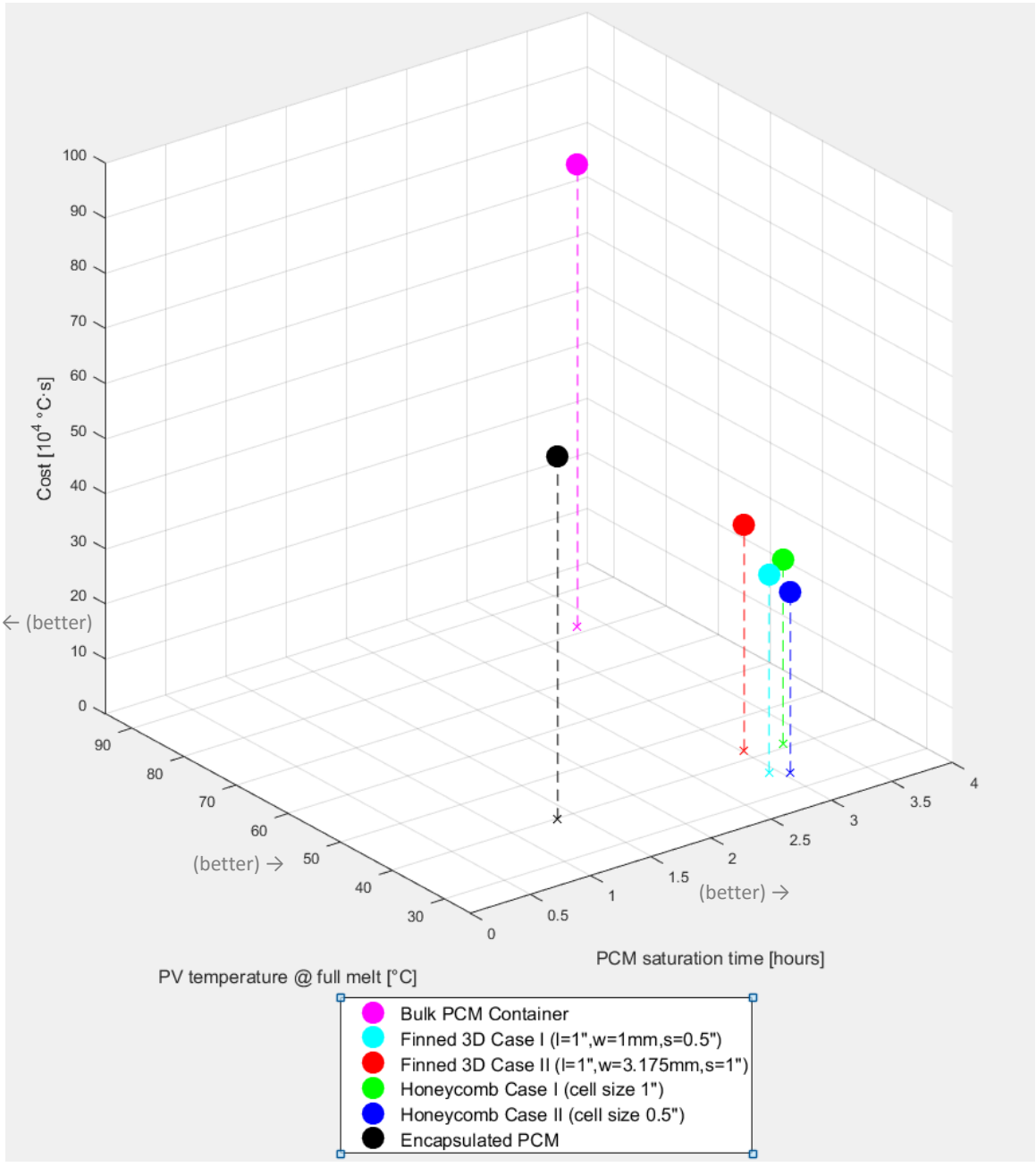

Figure 3.24: Graphical comparison of performance metrics.

Figure 3.24 shows all three performance metrics – PCM saturation time, PV temperature at saturation, and cost – compared graphically. Configurations with longer saturation times, lower PV temperatures at saturation and lower cost over the 5-hour simulation time are considered better suited for temperature regulation.

Chapter IV

Conclusions and Future Work

PV panels are a commonly used to convert solar energy to clean electricity. But, their energy conversion efficiency drops with an increase in panel temperature with exposure to insolation. This thesis explores a PCM-based passive temperature regulation system for PV panels. The PCM is placed into a container attached to the back surface of the panel, and absorbs incoming heat at a constant temperature while changing phase. Four configurations of PCM inside the aluminum container are explored.

In the first configuration, bulk PCM fills up the entire interior volume of the container. With three different depths of the container modelled (0.33", 0.5" and 1'), it is seen that a deeper container regulates the PV temperature for a longer time. However, the rise in PV temperature during the melt phase of PCM occurs at the same rate for each depth of container. This suggests that the extra thermal mass of PCM in deeper containers is not being effectively utilized to regulate temperature. And, in the absence of any heat transfer mechanism to remove heat from the PCM in the container, PV temperature still reaches high values.

A three-dimensional model of the bulk PCM container is also created, and results compared to the 2D model. Results show that the sidewalls of the container are able to remove a part of the incoming heat to the bottom layers of PCM, thus decreasing PV temperature and PCM saturation time. Since this container design has no aluminum fin

connecting the top and bottom plates, the 2D model under predicts the performance of the temperature regulation system.

With the knowledge that addition of aluminum to the PCM container improves performance, straight aluminum fins are added to a container of 1” internal depth in order to promote heat transfer into the PCM away from the PV panel. The effects of varying fin length, width and spacing are investigated. Results show that with an increase in fin length, a larger part of the incoming heat is used as latent heat to melt PCM away from the PV panel, and hence, PV temperature is lowered. This is accompanied by a slight drop in saturation time. Fin width and spacing are then varied for two selected fin lengths – 13 mm and 25.4 mm. Results from both fin lengths show that wider fins are only marginally better at removing heat from the PV panel. Reduction in fin spacing as a more significant impact on PV temperature. Any increase in fin length or width, or a decrease in spacing, causes PCM saturation time to drop because of the reduced volume of PCM in the container. A container design with fins of length 1”, width 1 mm, and spacing 0.5” offers a good combination of relatively high saturation time of 2 hours and 51 minutes, and one of the lowest PV temperatures at full melt of 34°C.

Three-dimensional models two finned PCM container configurations are created. In both these designs, there are 1” long fins that connect the top and bottom aluminum plates. The results from 2D models of finned container still match very well with the 3D models. Only a small difference in melt times is seen because the added thermal mass of the container sidewalls is not present in the 2D models.

Since long, thin fins stacked close together are found best at maintaining low PV temperatures, an aluminum honeycomb core is used as a fin in the next configuration. The honeycomb has a depth of 1” to connect the top and bottom container plates, and two cell sizes are modelled: 0.5” and 1”. Both cases show a slight improvement in melt times over the most effective finned container design. PV temperatures at full melt are also among the lowest, at 40.9°C for 1” cells, and 34.1°C for 0.5” cells.

The encapsulated PCM configuration tries to overcome the problems of packaging and low thermal conductivity of the PCM. The PCM is in spherical pellets which provide a larger surface area for heat exchange. Water is used as a medium to draw heat from the container walls and bring it to the pellets. Results show a very short saturation time due to the substantially reduced PCM volume. The PV temperature is also higher than finned or honeycomb configurations throughout the simulation. These drawbacks of the encapsulated PCM configuration could be mitigated by altering the size of the pellets so that a larger volume of PCM can be carried inside the container.

Values of the developed cost function are computed for a few selected configurations and compared to gauge their performance. The minimum cost among these configurations is attained when using an aluminum honeycomb core of cell size 0.5” as a fin in the PCM container. Other configurations with similarly low costs are honeycomb core fin of 1” cell size, and straight fins of length 1”, width 1 mm and spacing 0.5”.

In this purely numerical analysis, perfect thermal contact is assumed between the container plates and the straight or honeycomb core fins. However, the honeycomb core

has a very small foil thickness, and with realistic manufacturing considerations, it would be very difficult to attach this to the to the container walls. Thus, good thermal contact might not be achieved. It would be easier to manufacture a PCM container with straight aluminum fins attached to the walls inside it. Also, when this temperature regulation system is attached to a PV panel, it would be expected to work throughout the day. Thus, an active heat exchanger cooling tube would pass through the container to re-solidify the PCM upon saturation. Routing this tube would be much easier with straight fins than with a honeycomb container. Thus, in a realistic manufacturing solution, a PCM container with long, narrow, closely spaced straight fins would be the best option.

The results obtained from numerical simulations of various configurations show that a PCM based system is an effective way of regulating PV panel temperature. More work can be done to verify this claim. The numerical setup needs to be validated with data from controlled laboratory experiments which mimic the geometry, heating load and boundary conditions of the simulated model.

A different modelling approach for the PCM, called the enthalpy-porosity method, can be used. This method tracks the position of the melt front of the PCM, and captures convection effects in the melted regions.

Similarly, a CFD solver can be used to model the convection in the water inside the container of the encapsulated configuration. This would promote the removal of heat from the PV surface into the PCM pellets, and could result in lower PV temperature at PCM saturation time.

The simulations set up for this work assumed a constant heat flux coming into the adiabatic PCM container. This would not be the case in reality. To assess the performance for varying outdoor conditions, the numerical experiments need to be set up with varying values of the heating load and convective boundary conditions. Thermal properties of the PV panel can also be factored in to affect how much solar insolation turns to heat and reaches the PCM container.

After the above listed more detailed analyses are performed on the PCM container configurations, the results can be used to select the most effective passive temperature regulation system for PV panels that would limit the drop in electrical efficiency.

Appendix A

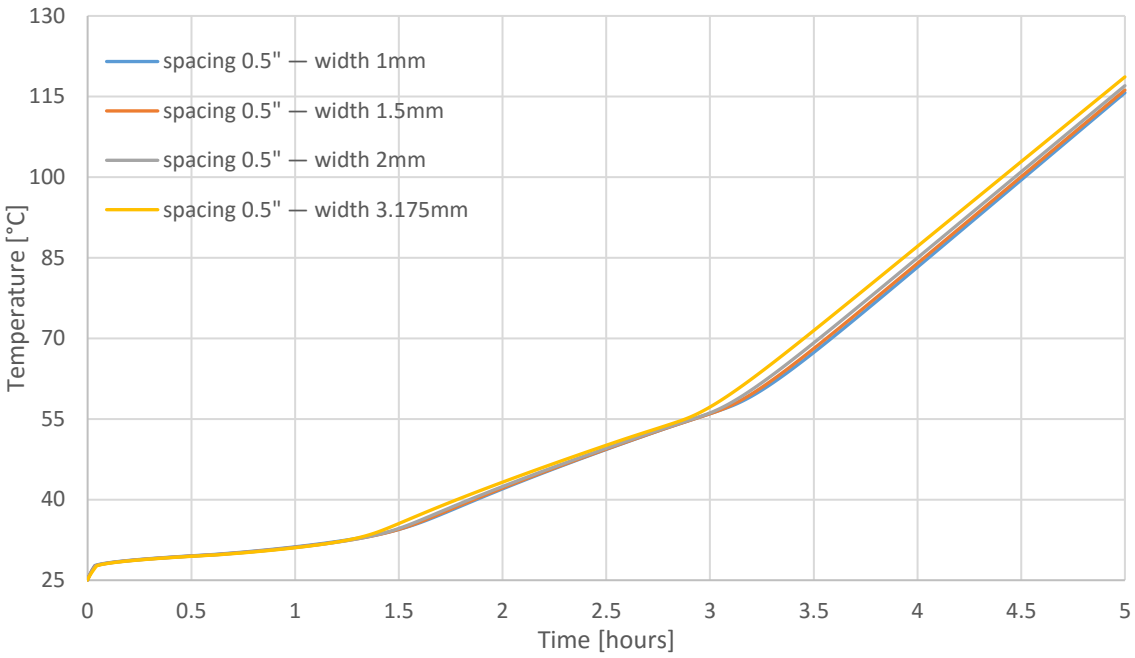

Figure A.1: *L*1 temperature plots for finned container Case II. Four fin widths arranged with a spacing of 0.5" are shown.

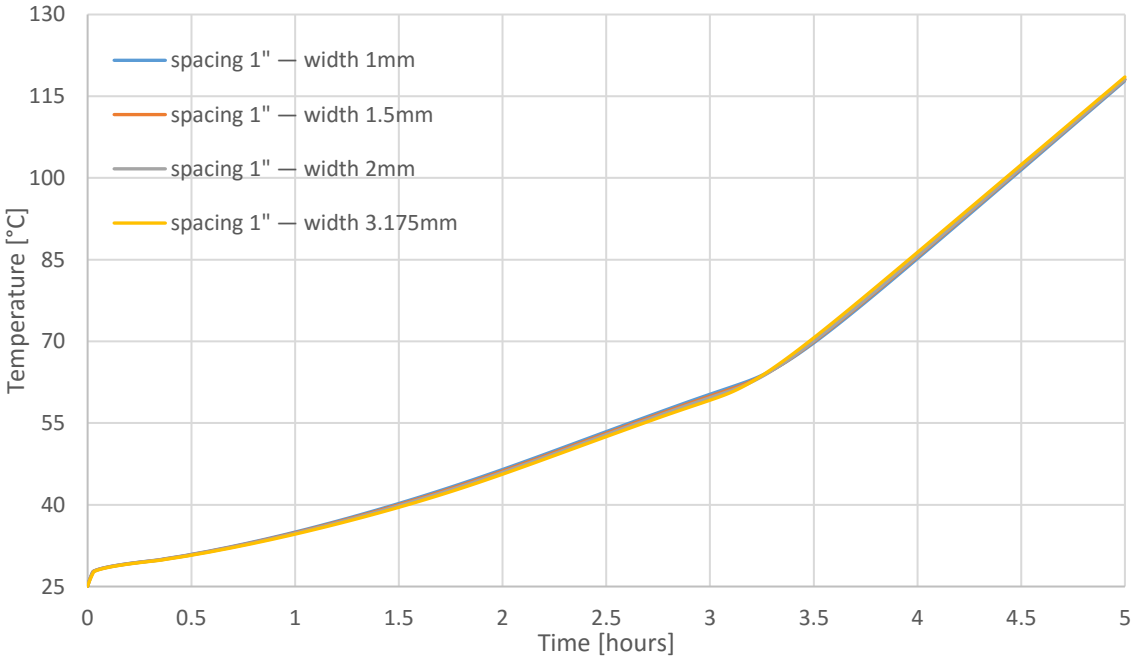

Figure A.2: *L*1 temperature plots for finned container Case II. Four fin widths arranged with a spacing of 1" are shown.

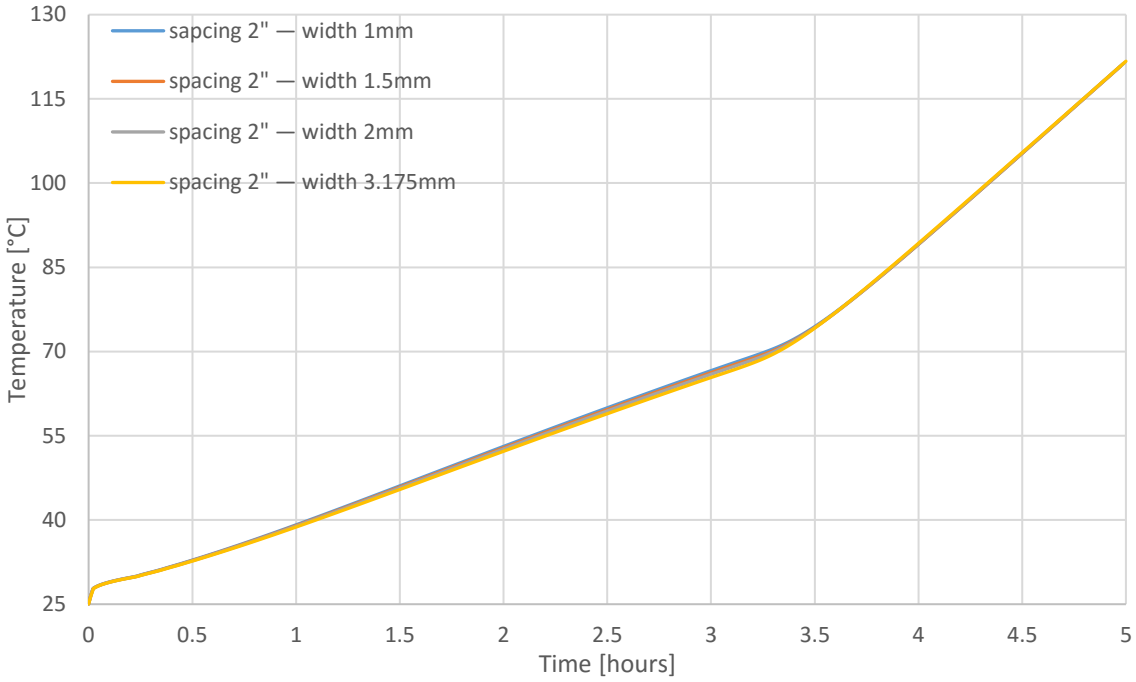

Figure A.3: *L*1 temperature plots for finned container Case II. Four fin widths arranged with a spacing of 2" are shown.

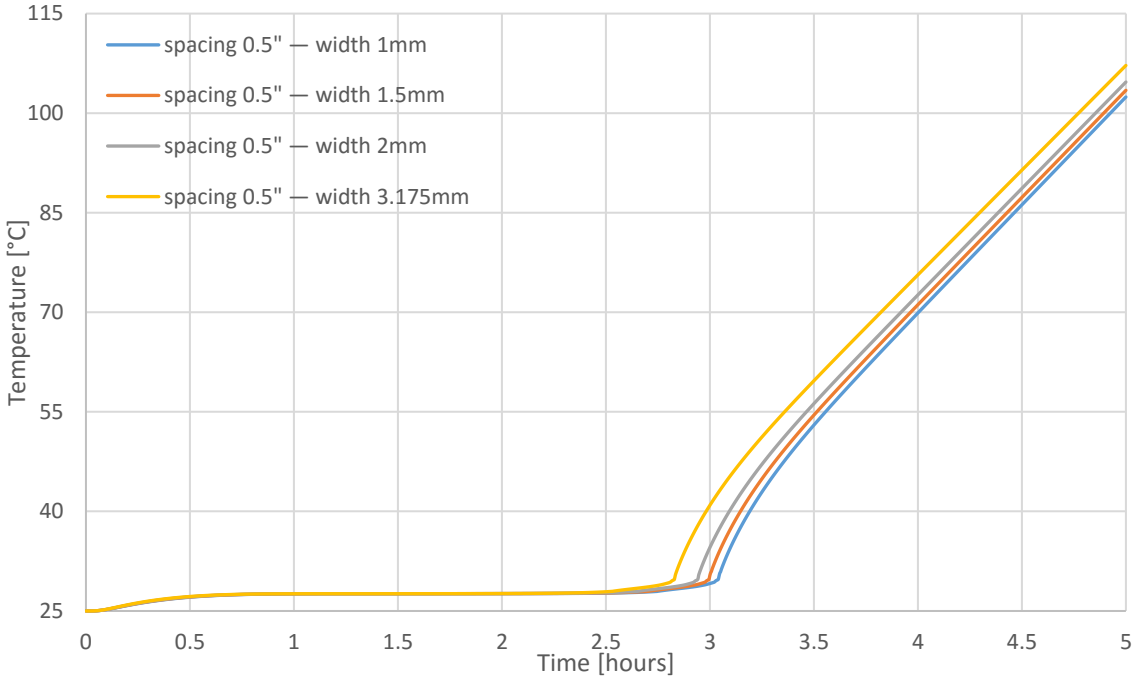

Figure A.4: *L*5 temperature plots for finned container Case II. Four fin widths arranged with a spacing of 0.5" are shown.

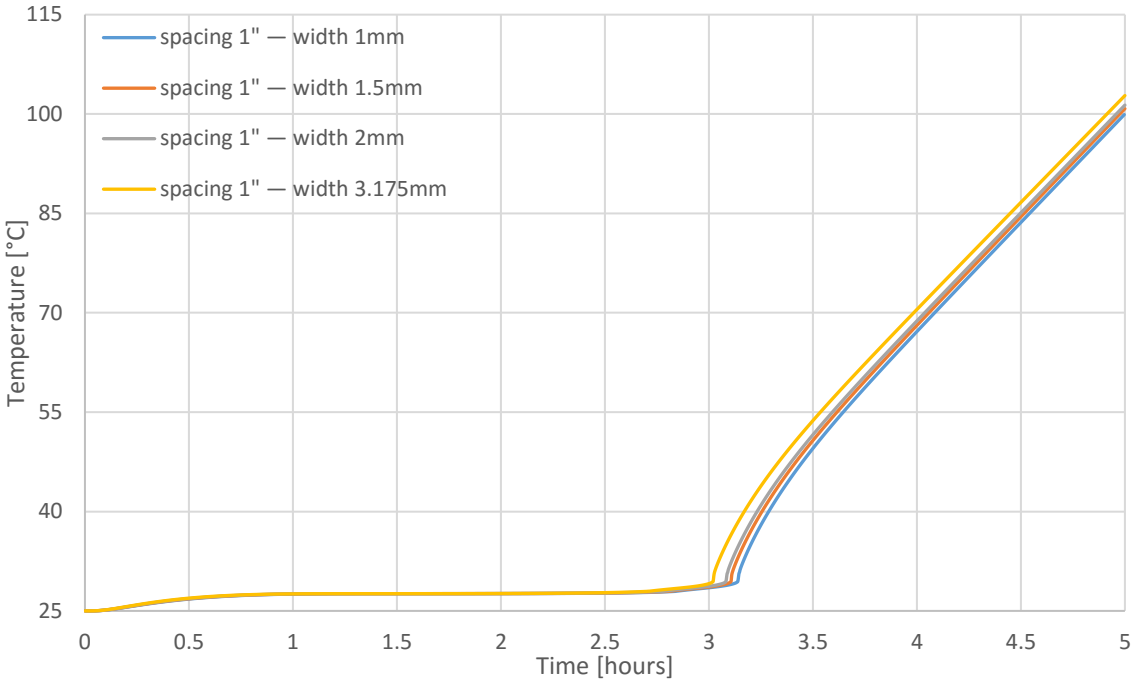

Figure A.5: *L*5 temperature plots for finned container Case II. Four fin widths arranged with a spacing of 1" are shown.

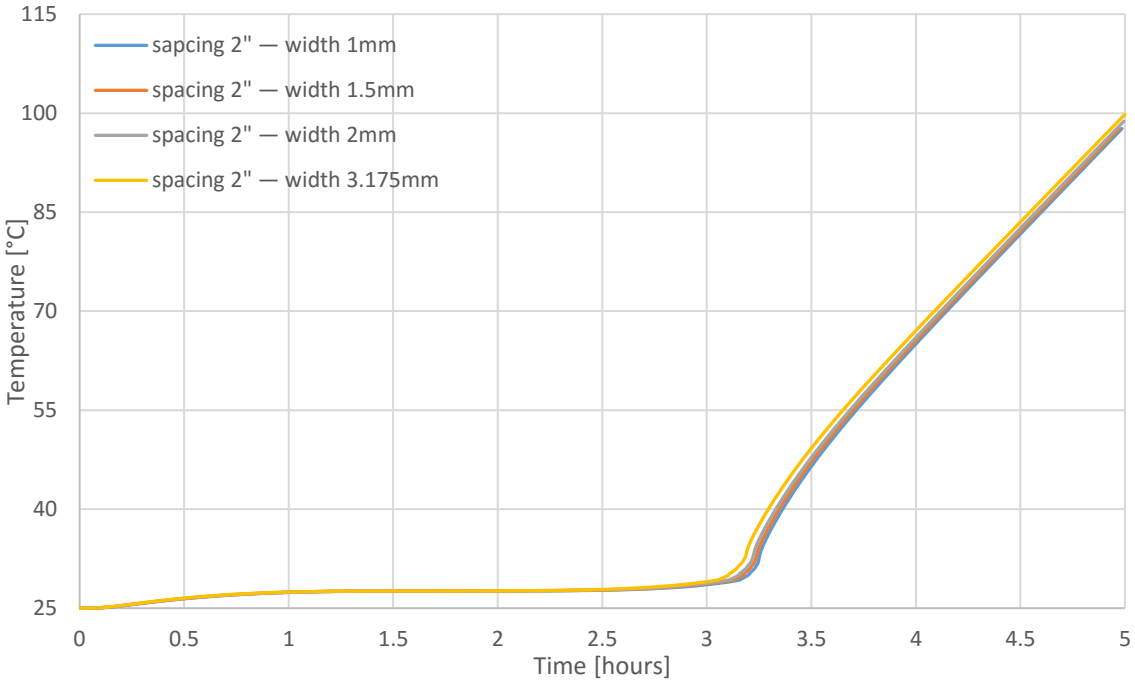

Figure A.6: *L*5 temperature plots for finned container Case II. Four fin widths arranged with a spacing of 2" are shown.

Appendix B

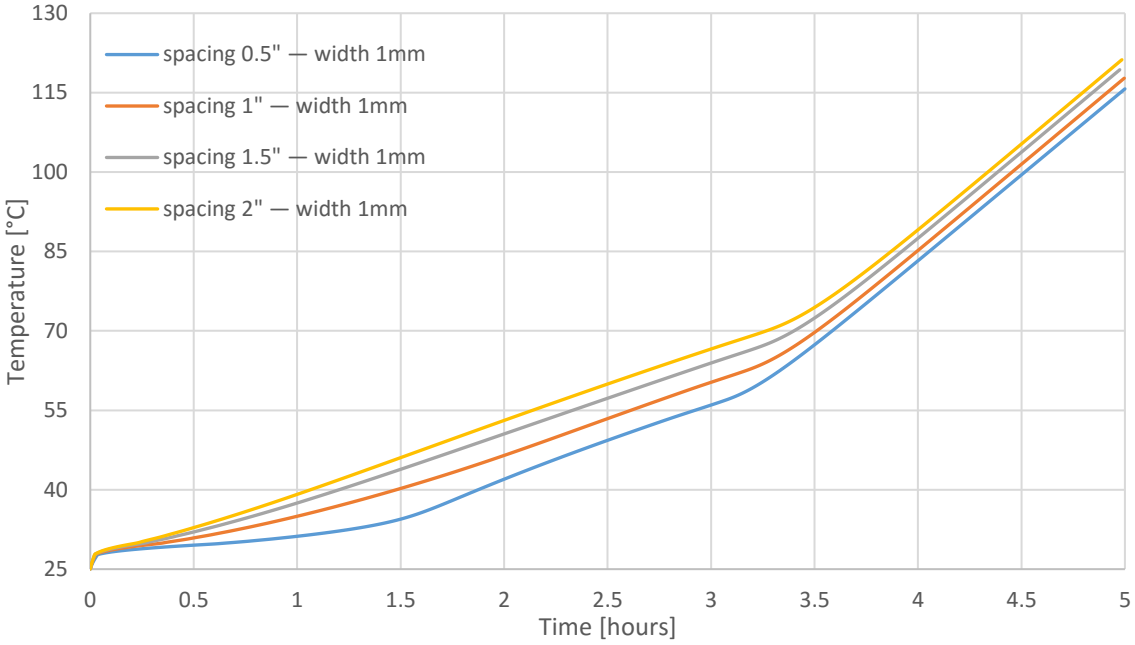

Figure B.1: *L*1 temperature plots for finned container Case II. This graph shows fins of width 1 mm arranged with four different values of fin spacing.

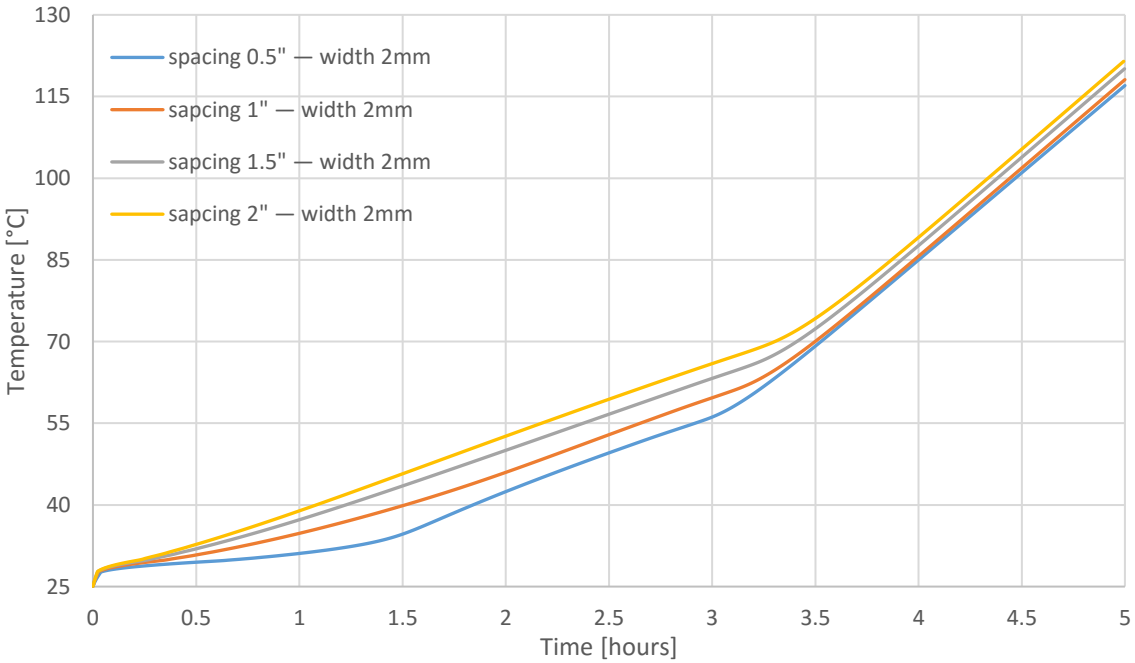

Figure B.2: *L*1 temperature plots for finned container Case II. This graph shows fins of width 2 mm arranged with four different values of fin spacing.

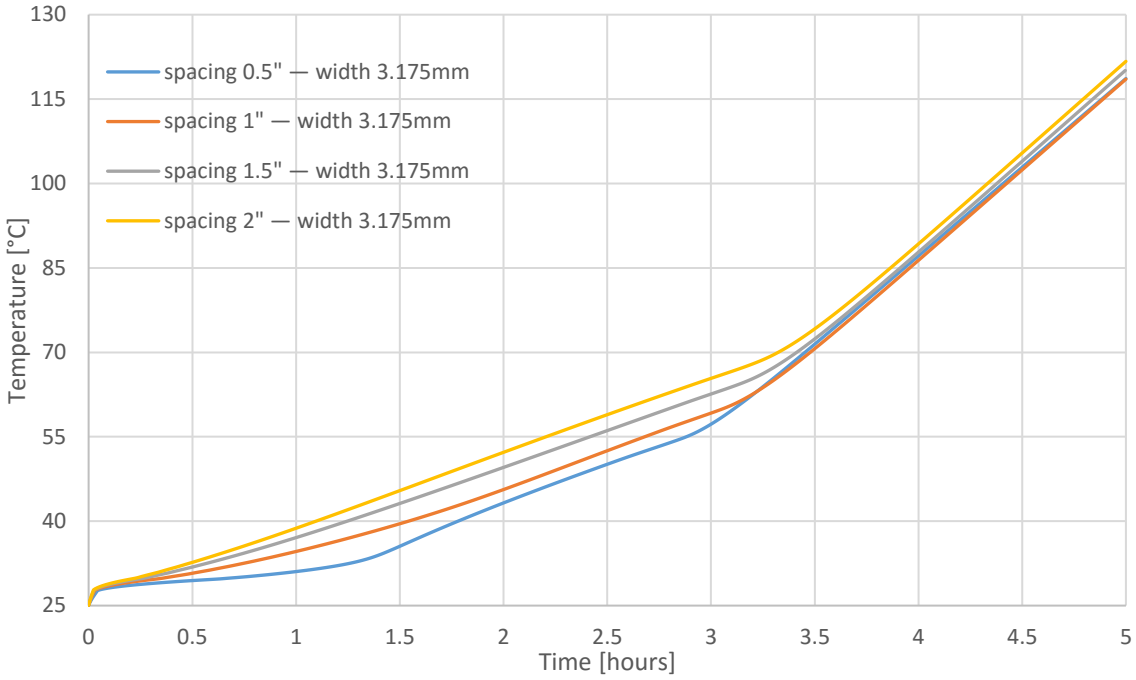

Figure B.3: $L1$ temperature plots for finned container Case II. This graph shows fins of width 3.175 mm arranged with four different values of fin spacing.

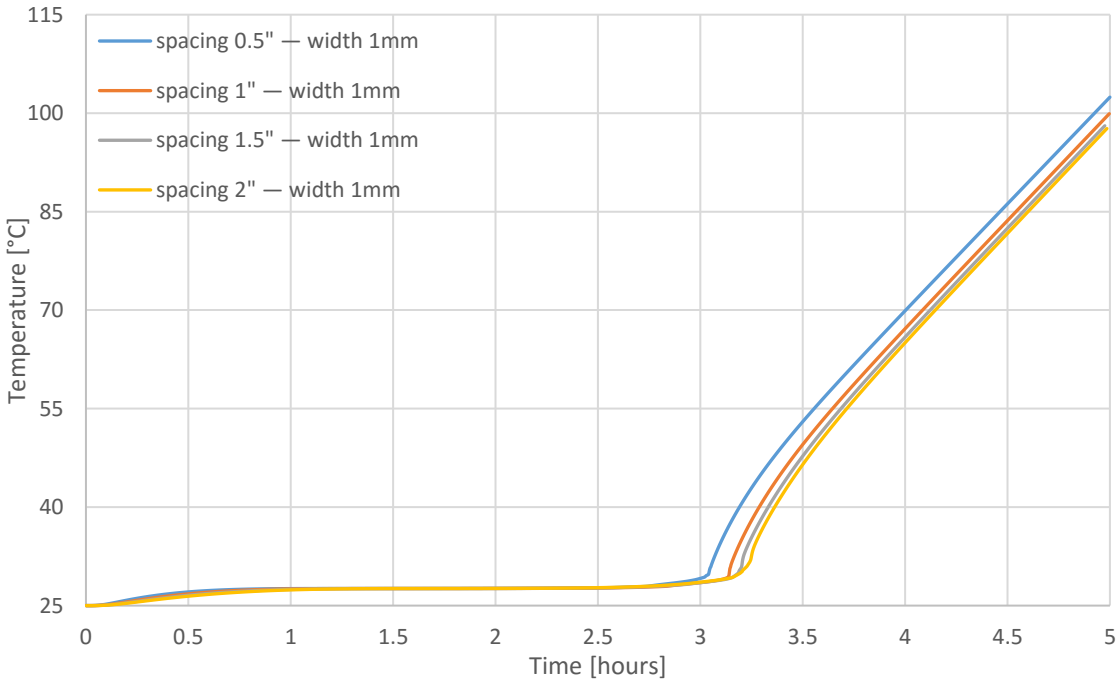

Figure B.4: $L5$ temperature plots for finned container Case II. This graph shows fins of width 1 mm arranged with four different values of fin spacing.

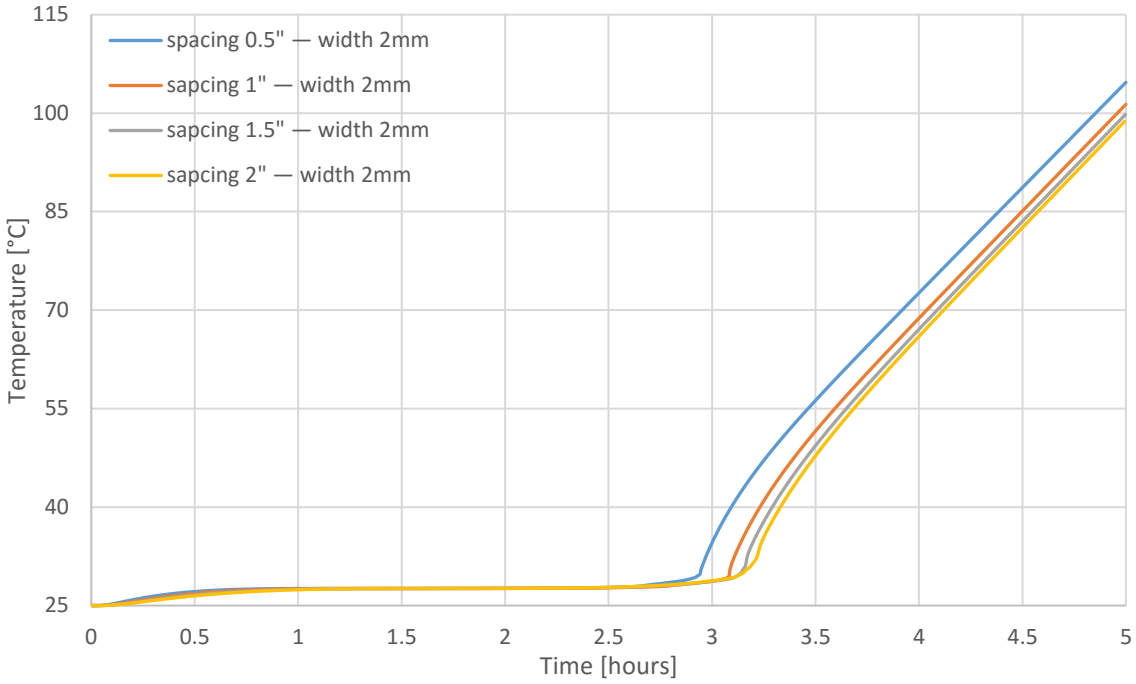

Figure B.5: *L*5 temperature plots for finned container Case II. This graph shows fins of width 2 mm arranged with four different values of fin spacing.

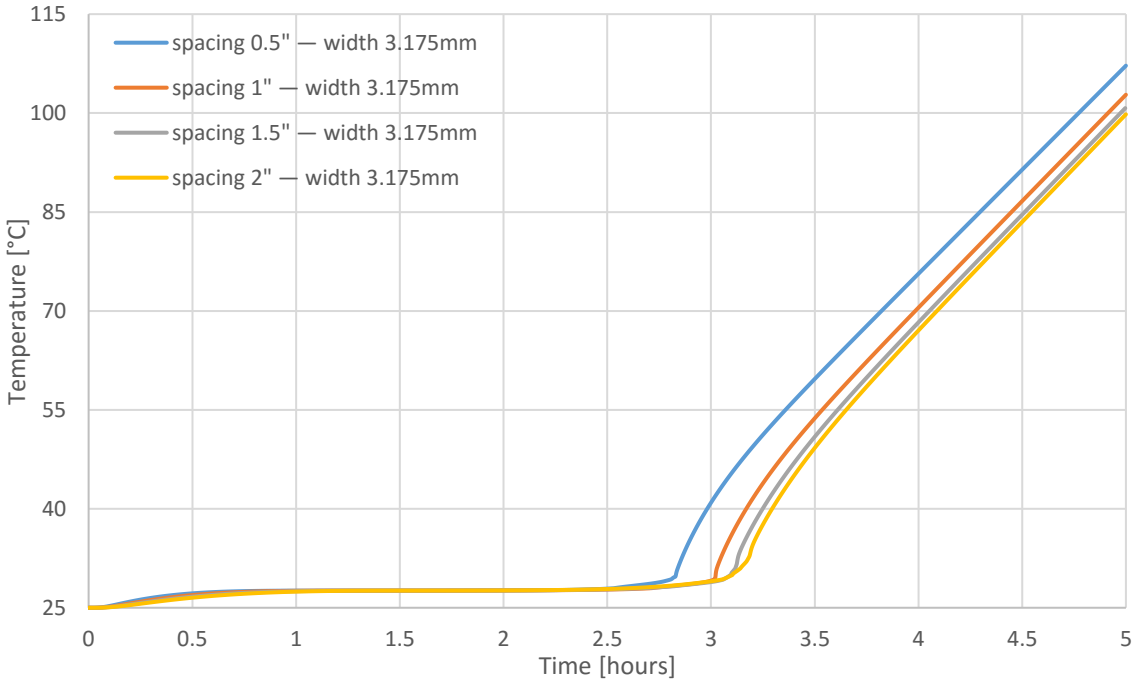

Figure B.6: *L*5 temperature plots for finned container Case II. This graph shows fins of width 3.175 mm arranged with four different values of fin spacing.

Appendix C

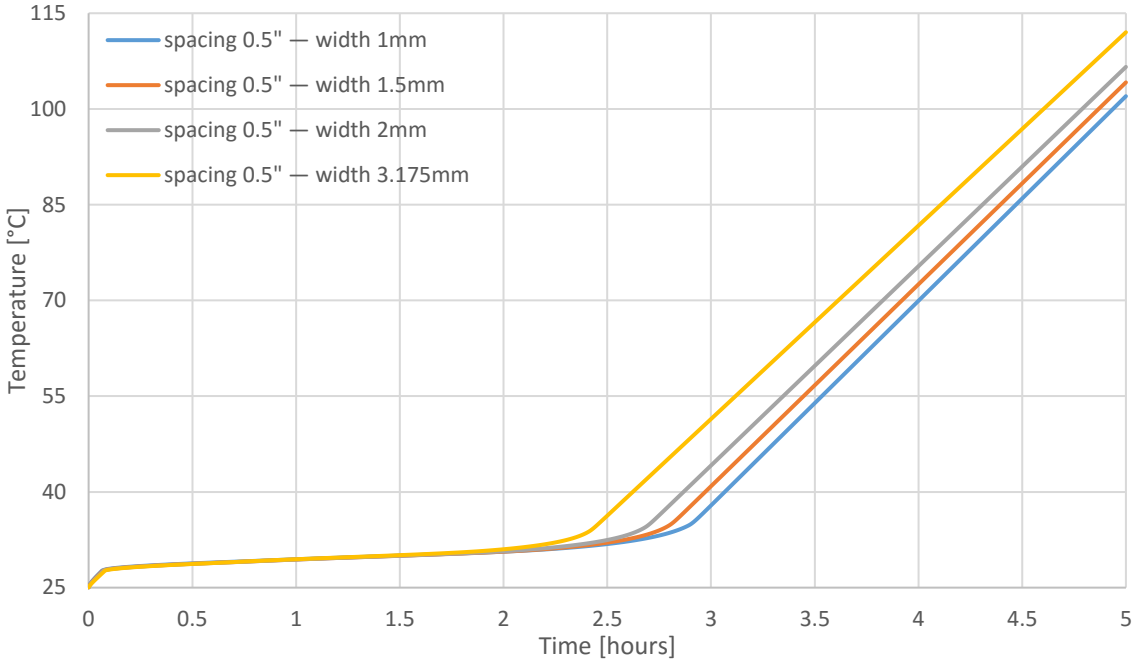

Figure C.1: *L*1 temperature plots for finned container Case III. Four fin widths arranged with a spacing of 0.5" are shown.

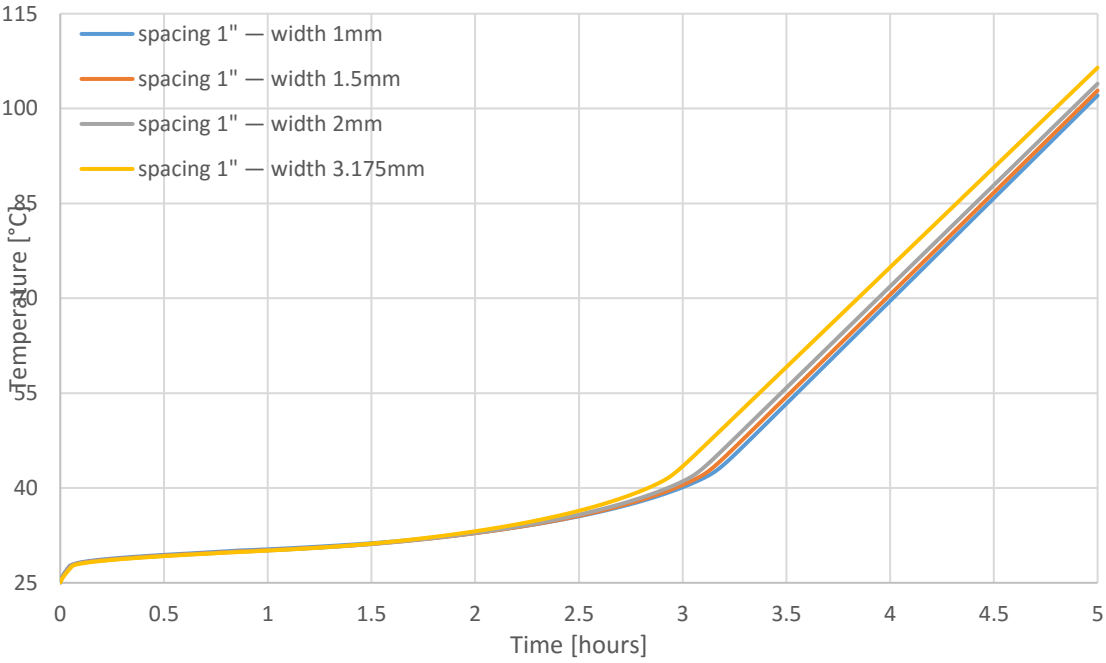

Figure C.2: *L*1 temperature plots for finned container Case III. Four fin widths arranged with a spacing of 1" are shown.

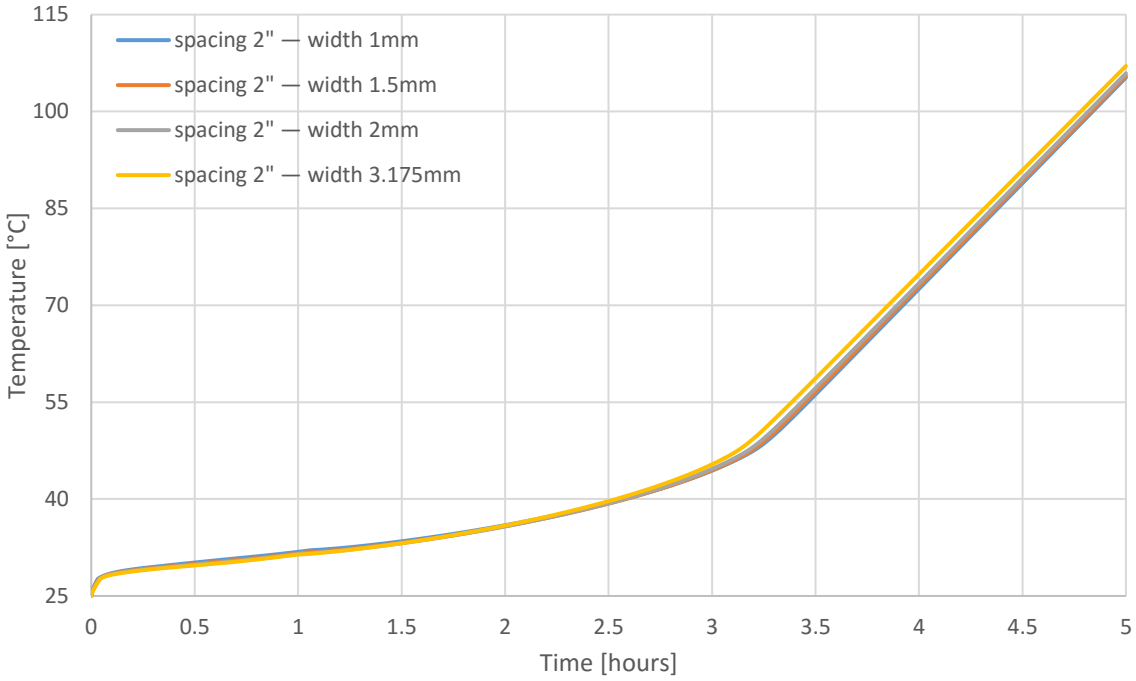

Figure C.3: *L*1 temperature plots for finned container Case III. Four fin widths arranged with a spacing of 2" are shown.

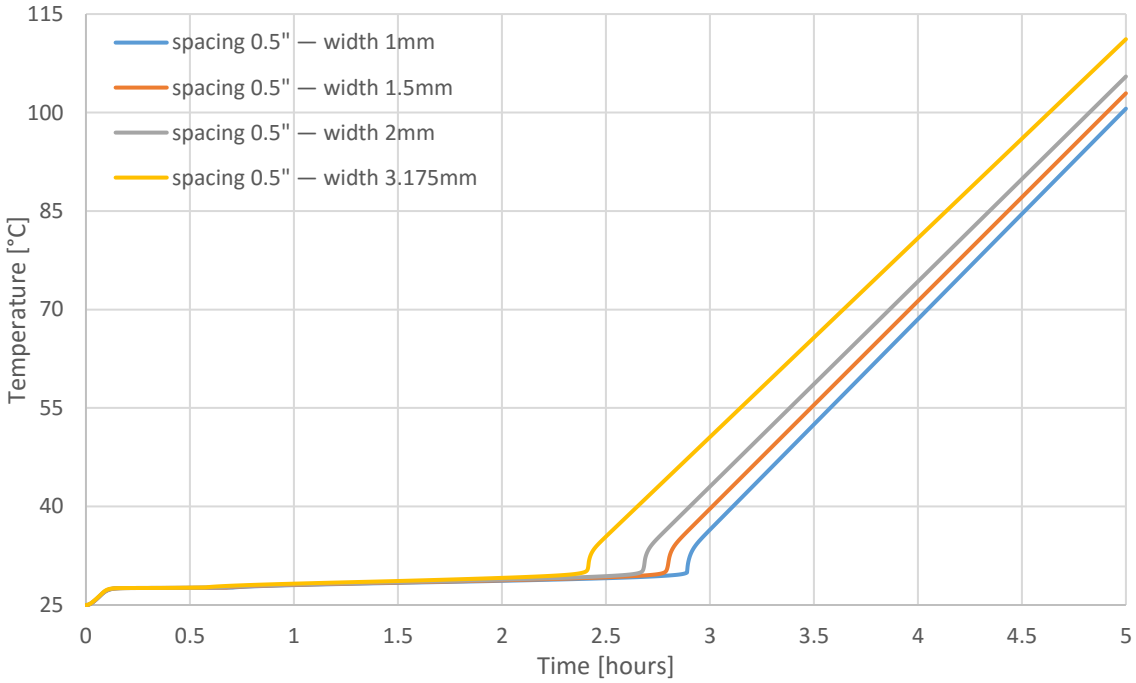

Figure C.4: *L*6 temperature plots for finned container Case III. Four fin widths arranged with a spacing of 0.5" are shown.

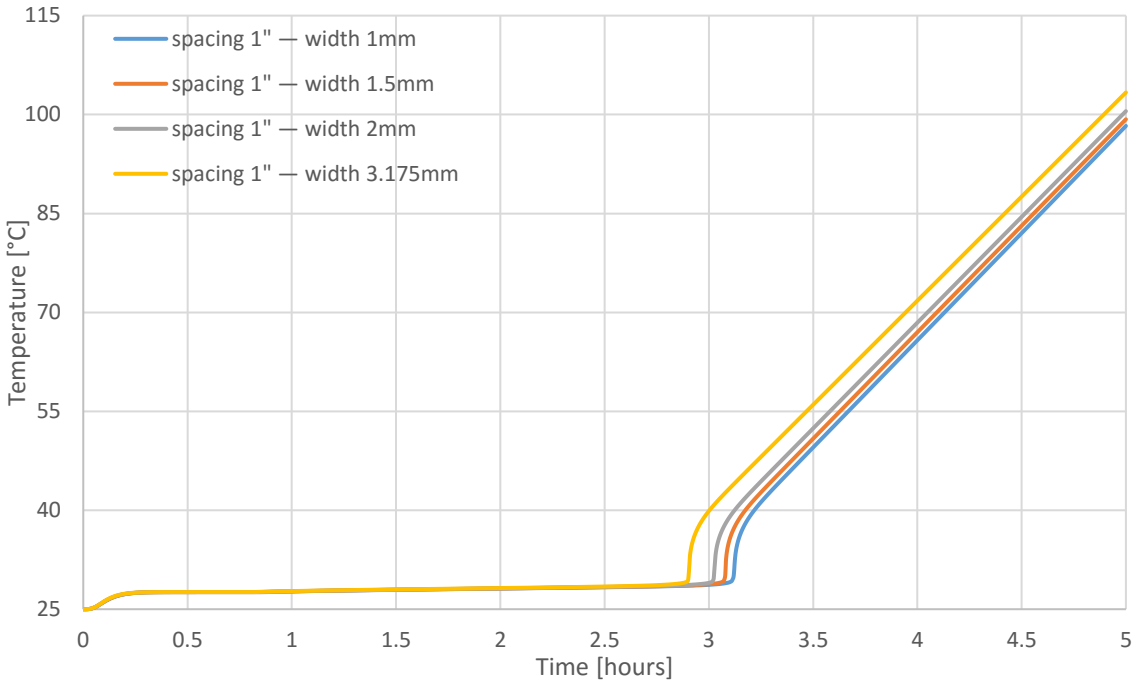

Figure C.5: *L*6 temperature plots for finned container Case III. Four fin widths arranged with a spacing of 1" are shown.

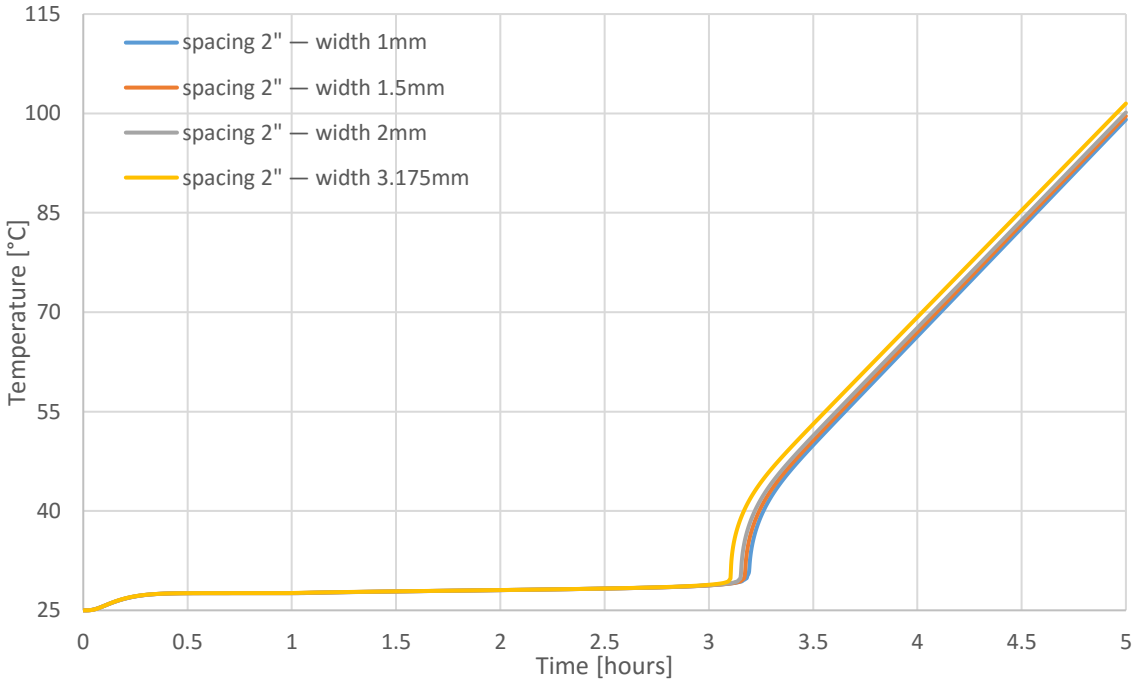

Figure C.6: *L*6 temperature plots for finned container Case III. Four fin widths arranged with a spacing of 2" are shown.

Appendix D

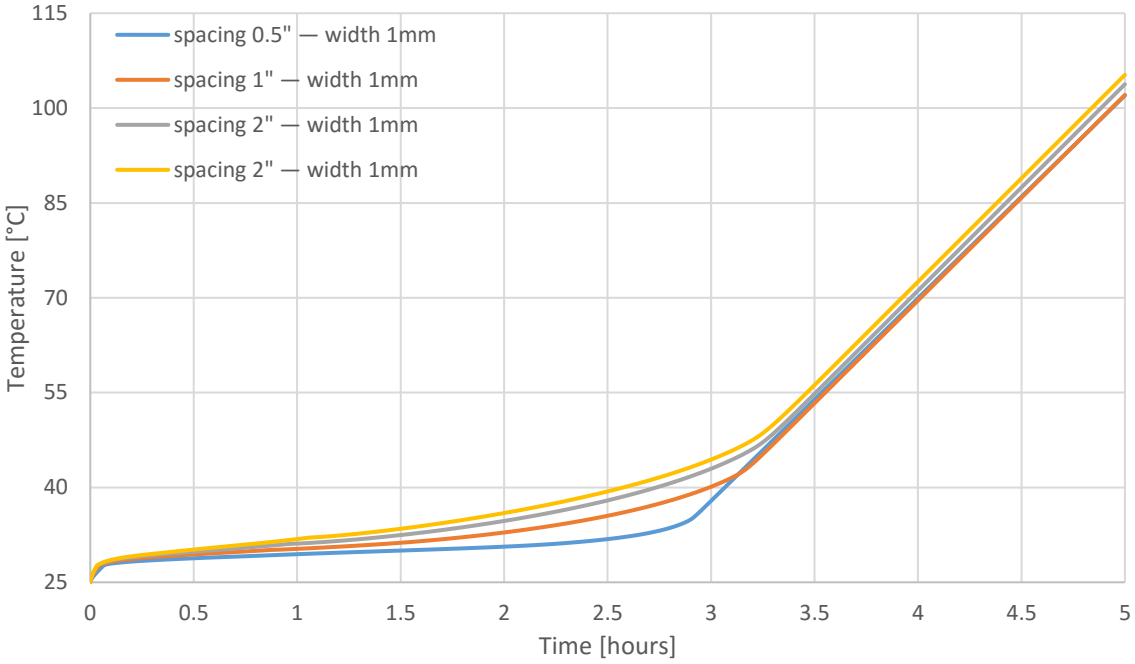

Figure D.1: *L*1 temperature plots for finned container Case III. This graph shows fins of width 1 mm arranged with four different values of fin spacing.

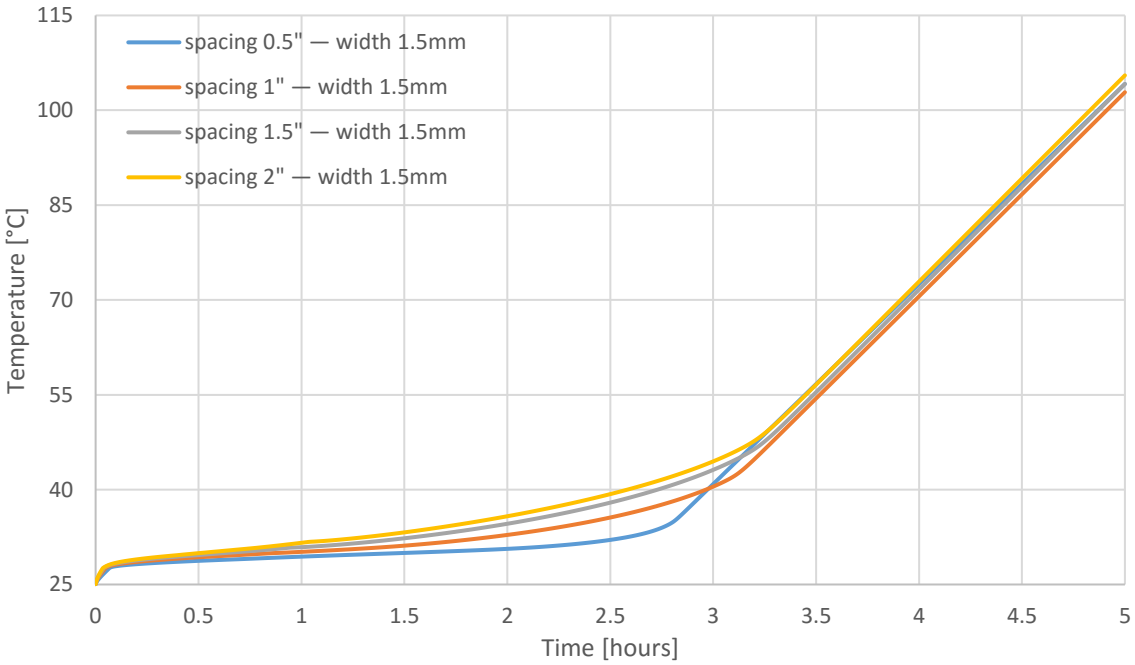

Figure D.2: *L*1 temperature plots for finned container Case III. This graph shows fins of width 1.5 mm arranged with four different values of fin spacing.

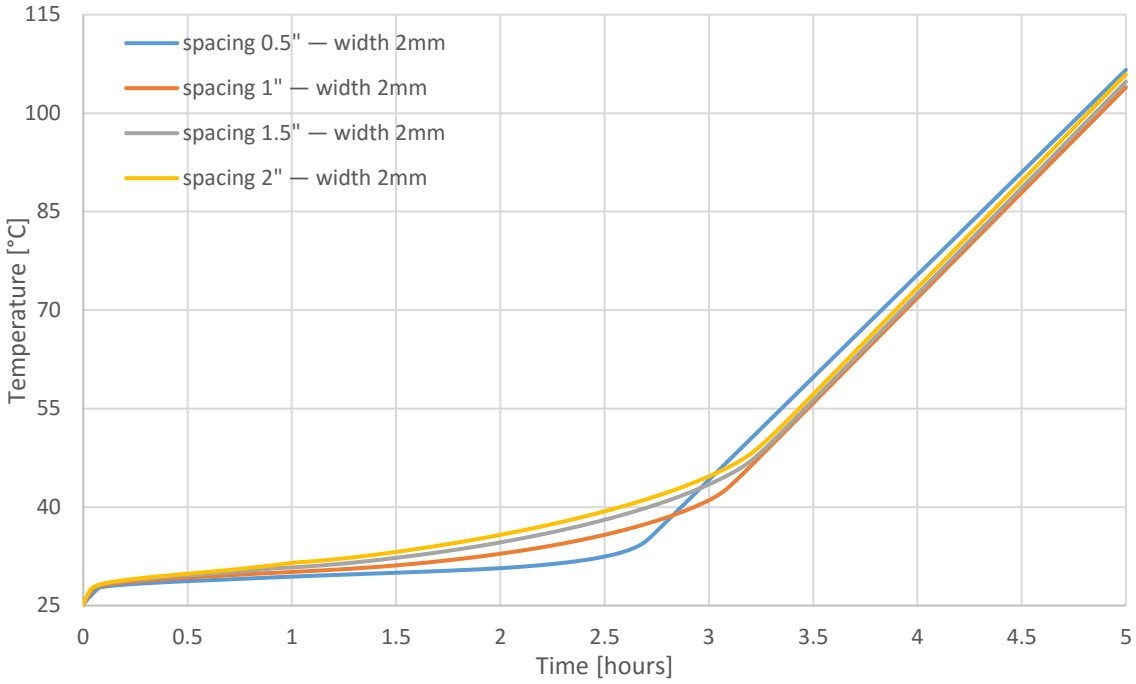

Figure D.3: *L*1 temperature plots for finned container Case III. This graph shows fins of width 2 mm arranged with four different values of fin spacing.

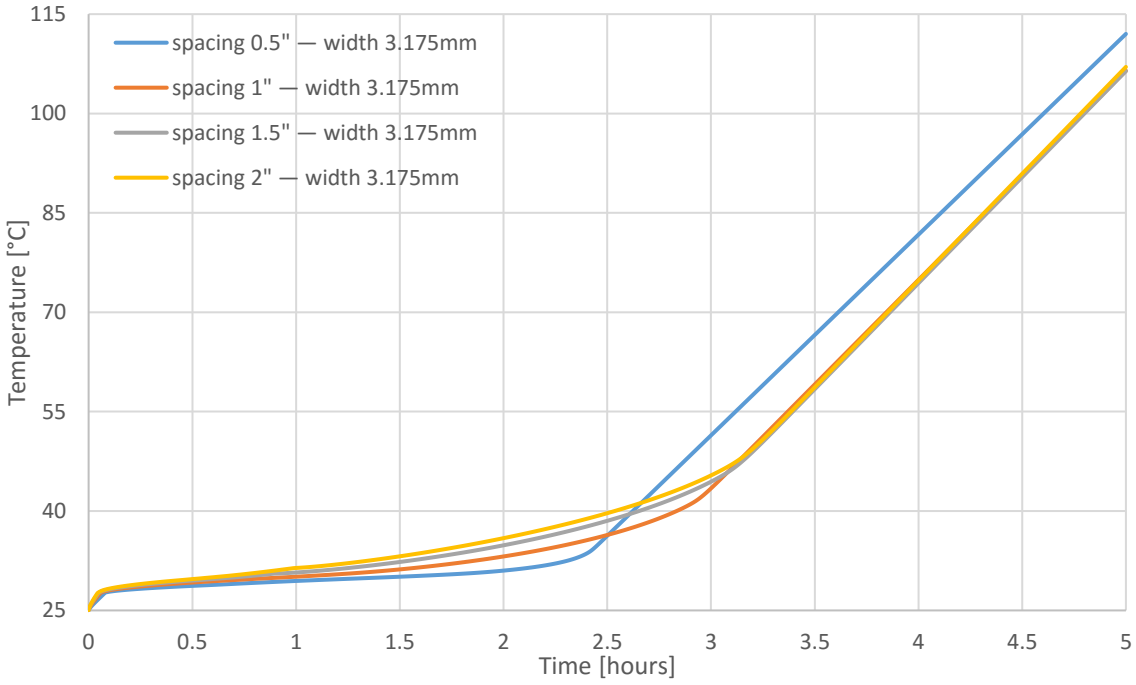

Figure D.4: *L*1 temperature plots for finned container Case III. This graph shows fins of width 3.175 mm arranged with four different values of fin spacing.

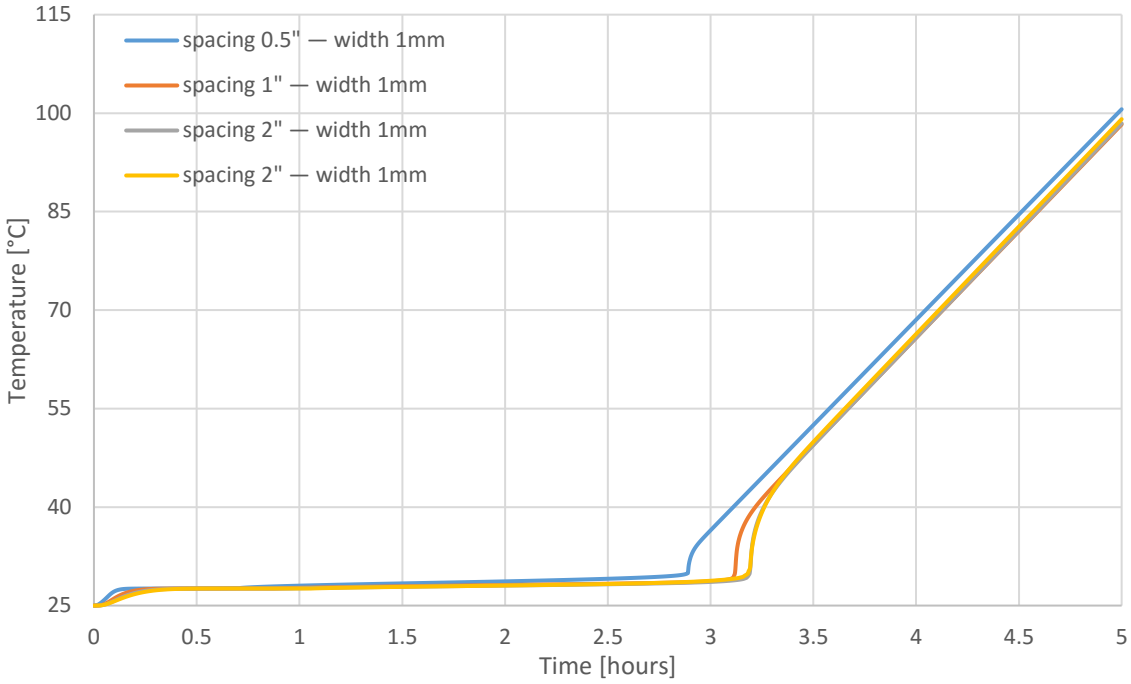

Figure D.5: *L*6 temperature plots for finned container Case III. This graph shows fins of width 1 mm arranged with four different values of fin spacing.

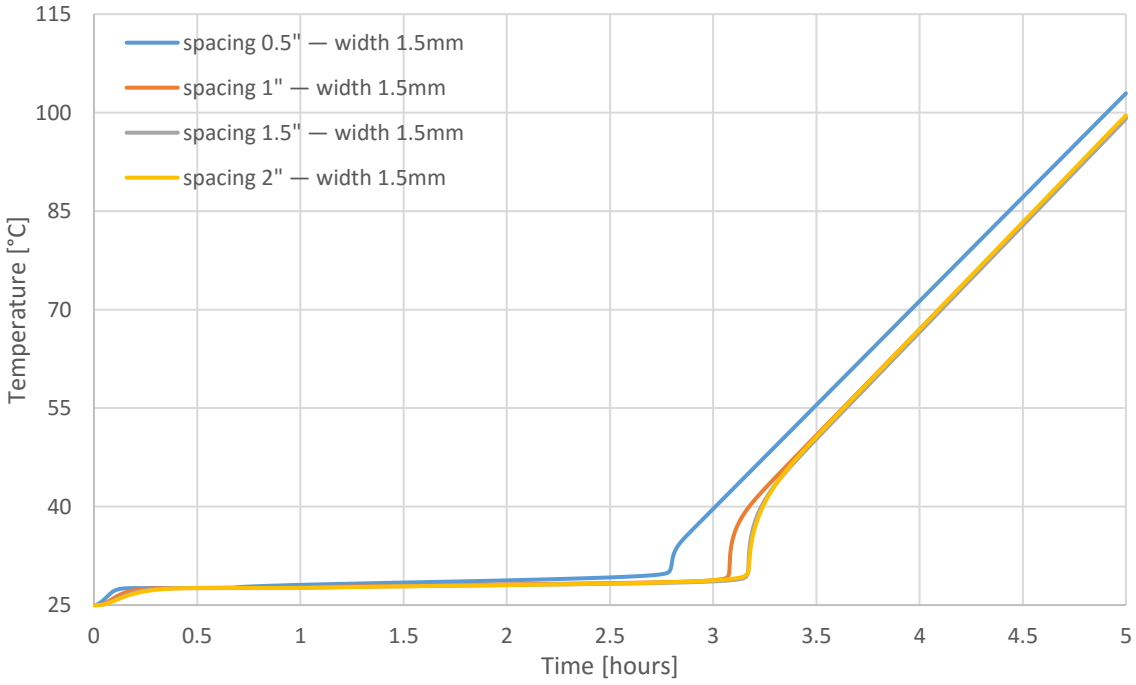

Figure D.6: *L*6 temperature plots for finned container Case III. This graph shows fins of width 1.5 mm arranged with four different values of fin spacing.

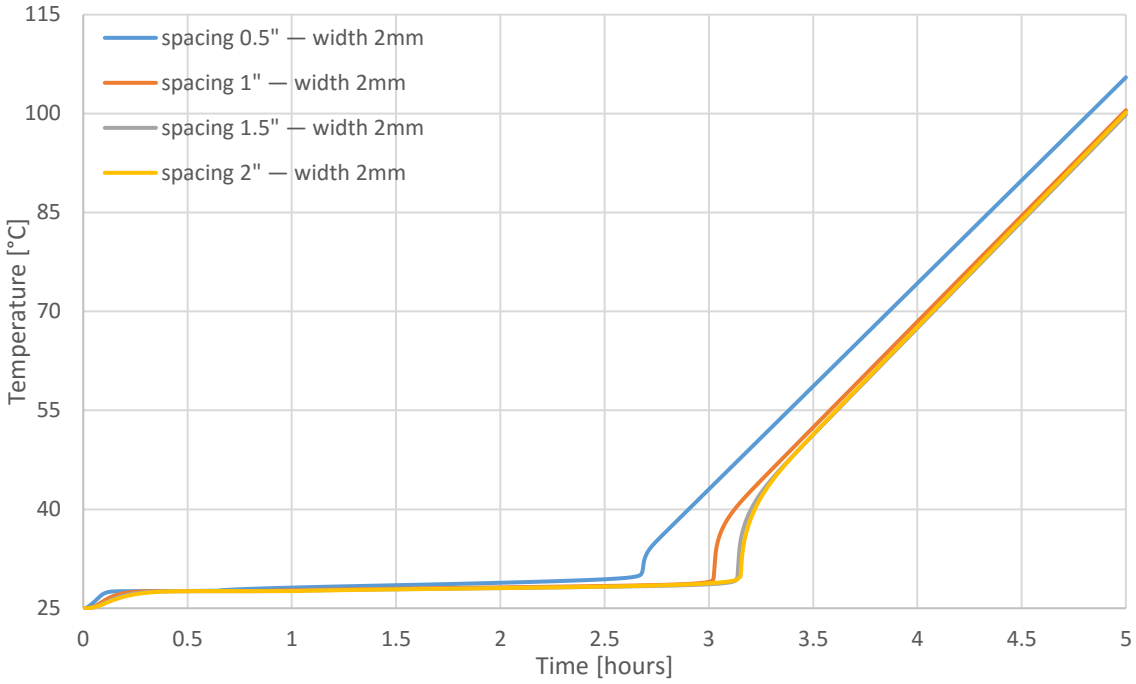

Figure D.7: *L*6 temperature plots for finned container Case III. This graph shows fins of width 2 mm arranged with four different values of fin spacing.

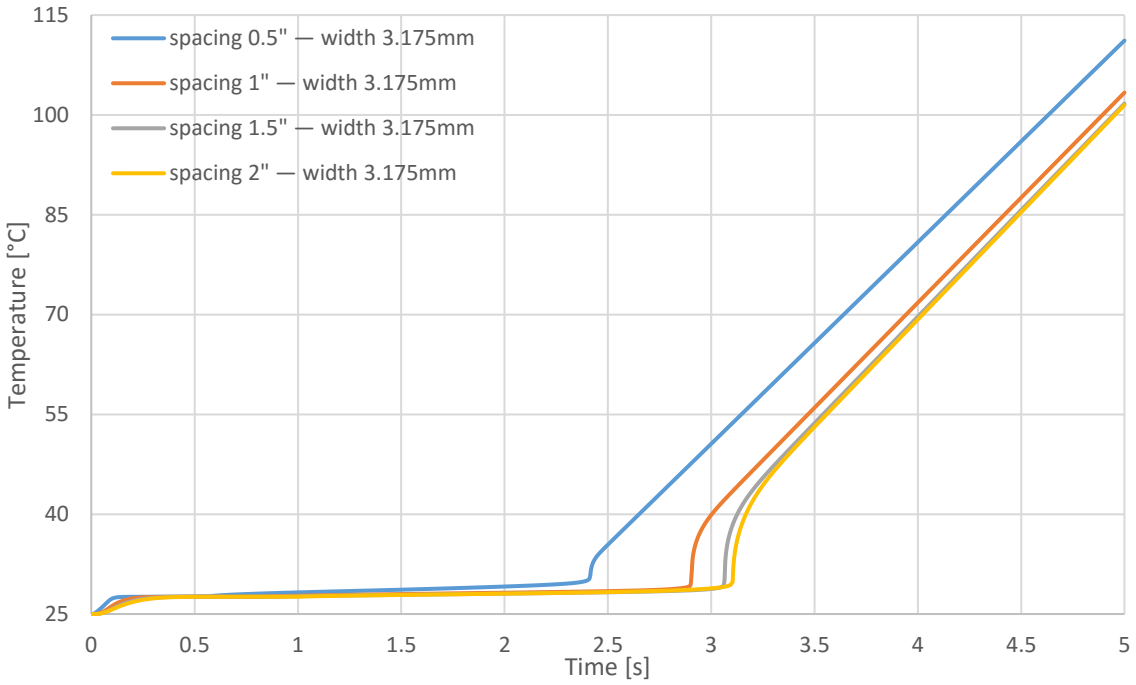

Figure D.8: *L*6 temperature plots for finned container Case III. This graph shows fins of width 3.175 mm arranged with four different values of fin spacing.

References

[1] U.S. Energy Information Administration, *Net Generation by Energy Source: Total (All Sectors), 2007-January 2017*, in Electric Power Monthly. Retrieved March 21, 2017, from https://www.eia.gov/electricity/monthly/epm_table_grapher.cfm?t=epmt_1_01 (2017).

[2] U.S. Energy Information Administration, *U.S. electric generating capacity increase in 2016 was largest net change since 2011*. Retrieved March 21, 2017, from https://www.eia.gov/todayinenergy/detail.php?id=30112# (2017).

[3] Weakliem, H., Redfield, D., "Temperature dependence of the optical properties of silicon," *Journal of Applied Physics*, 50, pp. 1491–1493 (1979).

[4] Krauter, S., "Actual optical and thermal performance of PV-modules," in "Proceedings of the 1st World Conference on Photovoltaic Energy Conversion," (1994).

[5] Radziemska, E., "The effect of temperature on the power drop in crystalline silicon solar cells," *Renewable Energy*, 28, pp. 1 – 12 (2003).

[6] Krauter, S., Araujo, R.G., Schroer, S., Hanitsch, R., Salih, M.J., Triebel, C., and Lemoine, R., "Combined photovoltaic and solar thermal systems for facade integration and building insulation," *Solar Energy*, 67, pp. 239 – 248 (1999).

[7] Chow, T., "A review on photovoltaic/thermal hybrid solar technology," *Applied Energy*, 87, pp. 365 – 379 (2010).

[8] Tyagi, V., Kaushik, S., and Tyagi, S., "Advancement in solar photovoltaic/thermal (PV/T) hybrid collector technology," *Renewable and Sustainable Energy Reviews*, 16, pp. 1383 – 1398 (2012).

[9] Ma, T., Yang, H., Zhang, Y., Lu, L., and Wang, X., "Using phase change materials in photovoltaic systems for thermal regulation and electrical efficiency improvement: A review and outlook," *Renewable and Sustainable Energy Reviews*, 43, pp. 1273 – 1284 (2015).

[10] Häusler, T., and Rogaß, H., "Photovoltaic module with latent heat storage - collector," in "Proceedings of the 2nd World Conference and Exhibition on Photovoltaic Solar Energy Conversion Vienna, Austria," (1998).

[11] Häusler, T., and Rogaß, H., "Latent heat storage on photovoltaics," in "16th European Photovoltaic Solar Energy Conference Glasgow, UK," (2000).

[12] Huang, M.J., Eames, P.C., and Norton, P., "Thermal regulation of building-integrated photovoltaics using phase change materials*," International Journal of Heat and Mass Transfer*, 47, pp. 2715 – 2733 (2004).

[13] Huang, M., Eames, P., and Norton, B., "Phase change materials for limiting temperature rise in building integrated photovoltaics," *Solar Energ*y, 80, pp. 1121 – 1130 (2006).

[14] Huang, M., Eames, P., and Norton, B., "Comparison of a small-scale 3D PCM thermal control model with a validated 2D PCM thermal control model," *Solar Energy Materials and Solar Cells*, 90, pp. 1961 – 1972 (2006).

[15] Kosny, J., Biswas, K., Miller, W., Childs, P., and Kriner, S., "Sustainable retrofit of residential roofs using metal roofing panels, thin-film photovoltaic laminates and PCM heat sink technology," *Journal of Building Enclosure Design* (2011).

[16] Kosny, J., Biswas, K., Miller, W., and Kriner, S., "Field thermal performance of naturally ventilated solar roof with PCM heat sink," *Solar Energy*, 86, pp. 2504 – 2514 (2012).

[17] Hasan, A., McCormack, S., Huang, M., and Norton, B., "Evaluation of phase change materials for thermal regulation enhancement of building integrated photovoltaics," *Solar Energy*, 84, pp. 1601 – 1612 (2010).

[18] Huang, M., Eames, P., Norton, B., and Hewitt, N., "Natural convection in an internally finned phase change material heat sink for the thermal management of photovoltaics," *Solar Energy Materials and Solar Cells*, 95, pp. 1598 – 1603 (2011).

[19] Biwole, P. H., Eclache, P., and Kuznik, F., "Phase-change materials to improve solar panel's performance," *Energy and Buildings*, 62, pp. 59 – 67 (2013).

[20] Brano, V. L., Ciulla, G., Piacentino, A., and Cardona, F., "Finite difference thermal model of a latent heat storage system coupled with a photovoltaic device: Description and experimental validation," *Renewable Energy*, 68, pp. 181 – 193 (2014).

[21] Park, J., Kim, T., and Leigh, S.-B., "Application of a phase-change material to improve the electrical performance of vertical-building-added photovoltaics considering the annual weather conditions," *Solar Energy*, 105, pp. 561 – 574 (2014).

[22] Aelenei, L., Pereira, R., Gonçalves, H., and Athienitis, A., "Thermal performance of a hybrid BIPV-PCM: Modeling, design and experimental investigation," *Energy Procedia*, 48, pp. 474 – 483 (2014).

[23] Aelenei, L., Pereira, R., Ferreira, A., Gonçalves, H., and Joyce, A., "Building integrated photovoltaic system with integral thermal storage: A case study," *Energy Procedia*, 58, pp. 172 – 178 (2014).

[24] Maiti, S., Banerjee, S., Vyas, K., Patel, P., and Ghosh, P. K., "Self regulation of photovoltaic module temperature in v-trough using a metal-wax composite phase change matrix," *Solar Energy*, 85, pp. 1805 – 1816 (2011).

[25] Hasan, A., McCormack, S., Huang, M., Sarwar, J., and Norton, B., "Increased photovoltaic performance through temperature regulation by phase change materials: Materials comparison in different climates," *Solar Energy*, 115, pp. 264 – 276 (2015).

[26] Sharma, S., Tahir, A., Reddy, K., and Mallick, T. K., "Performance enhancement of a building-integrated concentrating photovoltaic system using phase change material," *Solar Energy Materials and Solar Cells*, 149, pp. 29 – 39 (2016).

[27] Ho, C., Tanuwijava, A., and Lai, C.-M., "Thermal and electrical performance of a BIPV integrated with a microencapsulated phase change material layer," *Energy and Buildings*, 50, pp. 331 – 338 (2012).

[28] Ho, C., Jou, B.-T., Lai, C.-M., and Huang, C.-Y., "Performance assessment of a BIPV integrated with a layer of water-saturated MEPCM," *Energy and Buildings*, 67, pp. 322 – 333 (2013).

[29] Ho, C., Chou, W.-L., and Lai, C.-M., "Thermal and electrical performances of a water-surface floating PV integrated with double water-saturated MEPCM layers," *Applied Thermal Engineering*, 94, pp. 122 – 132 (2016).

[30] Ho, C., Chen, C.-C., and Yan, W.-M., "Experimental and numerical study on transient thermal energy storage of microencapsulated phase change material particles in an enclosure," *International Journal of Heat and Mass Transfer*, 94, pp. 191 – 198 (2016).

[31] Tanuwijava, A. O., Ho, C. J., Lai, C.-M., and Huang, C.-Y., "Numerical investigation of the thermal management performance of MEPCM modules for PV applications," *Energies*, 6, pp. 3922 – 3936 (2013).

[32] Barsotti, D. L., Hyatt, W. T., Compere, M. D., and Boetcher, S. K. S., "Battery thermal management for hybrid electric vehicles using a phase-change material cold plate," in "Proceedings of the ASME 2013 Heat Transfer Summer Conference Minneapolis, USA," (2013).

[33] Beckwith, J. A., Freeman, T. B., Cwiok, K. R., and Boetcher, S. K. S., "Utilizing phase-change material to thermally regulate and capture heat from building-integrated photovoltaic panels," in "Proceedings of the 2nd Thermal and Fluid Engineering Conference Las Vegas, USA," (2017).

[34] Shamsundar, N. N., and Sparrow, E. M., "Analysis of multidimensional conduction phase change via the enthalpy method," *ASME Journal of Heat Transfer*, 97, pp. 333-340 (1975).

[35] Çengel, Y. A., and Ghajar, A. J., *Heat and Mass Transfer*, New York: McGraw-Hill Education, pp. 910–920 (2015).

[36] National Renewable Energy Laboratory, *30-Year Average of Monthly Solar Radiation, 1961-1990: Daytona Beach*. Retrieved September 29, 2015, from http://rredc.nrel.gov/solar/old_data/nsrdb/1961-1990/redbook/sum2/12834.txt (1990).